"The Estimation of the Cylindrical Wave Reflection Coefficient"

Andrew Loris Kurkjian

TECHNICAL REPORT 495

July 1982

Massachusetts Institute of Technology
Research Laboratory of Electronics
Cambridge, Massachusetts 02139

This work has been supported in part by the Advanced Research Projects Agency monitored by ONR under Contract N00014-81-K-0742 NR-049-506 and in part by the National Science Foundation under Grant ECS80-07102

UNCLASSIFIED

SECURITY CLASSIFICATION OF THIS PAGE *(When Data Entered)*

REPORT DOCUMENTATION PAGE		READ INSTRUCTIONS BEFORE COMPLETING FORM
1. REPORT NUMBER	2. GOVT ACCESSION NO.	3. RECIPIENT'S CATALOG NUMBER
4. TITLE *(and Subtitle)* THE ESTIMATION OF THE CYLINDRICAL WAVE REFLECTION COEFFICIENT		5. TYPE OF REPORT & PERIOD COVERED Technical Report 6. PERFORMING ORG. REPORT NUMBER
7. AUTHOR(s) Andrew Loris Kurkjian		8. CONTRACT OR GRANT NUMBER(s) N00014-81-K-0742
9. PERFORMING ORGANIZATION NAME AND ADDRESS Research Laboratory of Electronics Massachusetts Institute of Technology Cambridge, MA 02139		10. PROGRAM ELEMENT, PROJECT, TASK AREA & WORK UNIT NUMBERS NR-049-506
11. CONTROLLING OFFICE NAME AND ADDRESS Advanced Research Projects Agency 1400 Wilson Boulevard Arlington, Virginia 22217		12. REPORT DATE July 1982 13. NUMBER OF PAGES 189
14. MONITORING AGENCY NAME & ADDRESS *(if different from Controlling Office)* Office of Naval Research Mathematical and Information Sciences Division, 800 North Quincy Street Arlington, Virginia 22217		15. SECURITY CLASS. *(of this report)* Unclassified 15a. DECLASSIFICATION/DOWNGRADING SCHEDULE

16. DISTRIBUTION STATEMENT *(of this Report)*

Approved for public release; distribution unlimited

17. DISTRIBUTION STATEMENT *(of the abstract entered in Block 20, if different from Report)*

18. SUPPLEMENTARY NOTES

19. KEY WORDS *(Continue on reverse side if necessary and identify by block number)*

wave
reflection
coefficient
well logging
maximum likelihood
array
borehole

20. ABSTRACT *(Continue on reverse side if necessary and identify by block number)*

see other side

DD FORM 1 JAN 73 1473 EDITION OF 1 NOV 65 IS OBSOLETE

UNCLASSIFIED

SECURITY CLASSIFICATION OF THIS PAGE *(When Data Entered)*

20. ABSTRACT

In the acoustic well logging problem an acoustic source and an array of receivers are placed in a borehole for the purpose of resolving the acoustic properties of the surrounding formation. In the existing approach to this problem, a received array is placed at a large offset from the source and energy refracted by the formation is analyzed. Here, a short-offset array is used to analyze energy reflected by the formation.

The formation is modeled as cylindrically stratified and the concepts and properties of the monochromatic cylindrical wave and the cylindrical wave reflection coefficient are developed. The reflection coefficient carries information pertaining to the radial structure of the formation and is of fundamental interest. A separate problem is the interpretation, or inversion, of the reflection coefficient in terms of the radial structure.

The reflection coefficient as a function of frequency, but at a single axial wavenumber, is estimated from the reflected component of the total field on the axis of the borehole. The signal processing problem is one of dereverberation and a maximum likelihood (ML) estimation criterion is used. The ML estimation problem is nonlinear and an iterative method is applied. The method is guaranteed to increase the log likelihood function with each iterative pass and, within a given iteration, only linear processing is required.

A rapid method for generating arrays of synthetic acoustic logging data is developed and the data is used to test and evaluate the iterative ML dereverberation scheme. The reflection coefficient estimates are found to be accurate within the passband of the source pulse except at those frequencies which excite modes. The estimation performance is sensitive to the array design and to the signal-to-noise ratio.

THE ESTIMATION OF THE CYLINDRICAL WAVE REFLECTION COEFFICIENT

by

Andrew Loris Kurkjian

Submitted to the Department of Electrical Engineering and Computer Science on July 2, 1982
in partial fulfillment of the requirements for the degree of Doctor of Philosophy.

ABSTRACT

In the acoustic well logging problem an acoustic source and an array of receivers are placed in a borehole for the purpose of resolving the acoustic properties of the surrounding formation. In the existing approach to this problem, a receiver array is placed at a large offset from the source and energy *refracted* by the formation is analyzed. Here, a short-offset array is used to analyze energy *reflected* by the formation.

The formation is modeled as cylindrically stratified and the concepts and properties of the monochromatic cylindrical wave and the cylindrical wave reflection coefficient are developed. The reflection coefficient carries information pertaining to the radial structure of the formation and is of fundamental interest. A separate problem is the interpretation, or inversion, of the reflection coefficient in terms of the radial structure.

The reflection coefficient as a function of frequency, but at a single axial wavenumber, is estimated from the reflected component of the total field on the axis of the borehole. The signal processing problem is one of dereverberation and a maximum likelihood (ML) estimation criterion is used. The ML estimation problem is nonlinear and an iterative method is applied. The method is guaranteed to increase the log likelihood function with each iterative pass and, within a given iteration, only linear processing is required.

A rapid method for generating arrays of synthetic acoustic logging data is developed and the data is used to test and evaluate the iterative ML dereverberation scheme. The reflection coefficient estimates are found to be accurate within the passband of the source pulse except at those frequencies which excite modes. The estimation performance is sensitive to the array design and to the signal-to-noise ratio.

Thesis Supervisor: Alan V. Oppenheim

Title: Professor of Electrical Engineering

to my wife

Terri

and my parents

Joy and Jeff

ACKNOWLEDGEMENT

I am most deeply indebted to Professor Alan Oppenheim for his encouragement and support throughout this period of study. He originally directed me toward the acoustic well logging problem, arranged my summer employment at Schlumberger-Doll Research, and helped to initiate the Schlumberger fellowship which I received to support my study. In addition, he pointed me toward Bruce Musicus' masters thesis which led directly to the processing method developed in this thesis.

I am also grateful to Professor Arthur Baggeroer, Professor Alan Willsky and Dr. Robert Porter who each served as readers on the thesis committee. In particular, I wish to thank Dr. Porter who, as Director of the Mechanics-Electrical department at SDR, allowed me a free rein in my summers of employment and in many ways made my experience at SDR enjoyable.

I also want to thank the soon to be Dr. Douglas Mook. Doug's thesis work on the estimation of the plane wave reflection coefficient complemented my work associated with the cylindrical wave reflection coefficient. Our discussions had a distinct influence on this thesis. Dr. Steve Chang of Schlumberger-Doll Research also deserves thanks. His interest in the technical details of this research helped to make this thesis as strong as it is.

Funding for this research was provided by a fellowship from Schlumberger-Doll Research in Ridgefield CT. In addition, Schlumberger supported me through four summers of employment (1978-81) and gave me access to their computer and office facilities year round. The last six months of this study was spent in Ridgefield preparing the manuscript.

Finally, I would like to thank my friend Mark Dalton who, for a few bottles of Molsons Golden Ale, meticulously prepared the 75 figures contained in this thesis.

CONTENTS

LIST OF FIGURES

I. INTRODUCTION

II. ACOUSTIC WELL LOGGING

III. BOREHOLE ACOUSTICS

IV. THE NUMERICAL EVALUATION OF SYNTHETIC DATA

V. ITERATIVE MAXIMUM LIKELIHOOD DEREVERBERATION

VI. THE SINGLE WAVENUMBER SYSTEM

LIST OF TABLES

I. INTRODUCTION

1.1 Cylindrically Stratified Media

This thesis is concerned with wave propagation in cylindrically stratified (cylindrically layered) media. By "cylindrically stratified" we mean that there is no variation in the medium in either the angular or axial dimensions of a cylindrical coordinate system, but there is variation radially.

Our interest in cylindrically layered media arises out of the acoustic well logging application. Here, an acoustic source and an array of receivers are lowered into a borehole for the purpose of resolving, or imaging, the acoustic properties of the surrounding formation. From a perspective on the axis of the borehole, at acoustic frequencies, the earth's structure can often be accurately modeled as varying only in the radial dimension. The radial variation which is present in the formation is entirely a by-product of the drilling operation. Besides the cylindrical hole itself, the drilling contaminates the virgin formation in the vicinity of the hole. The mechanical, chemical, electrical and nuclear properties are all altered as a result of drilling. Thus, we imagine the borehole/formation wall as a strong reflecting interface behind which is a relatively weakly varying structure which tapers off to its virgin state a short distance from the hole.

Relative to wave propagation in planar layered media (i.e. media which varies axially, but not angularly or radially), wave propagation in cylindrically layered media has received little attention in the literature. However, planar and cylindrically layered geometries are coordinate system analogs of one another so that we might expect many of the concepts and methods which have been useful in the planar case to transfer to the cylindrical case, and vice versa. The recognition and exploitation of the analogies between the planar and cylindrical layered media problems is a central theme in this thesis.

Surface exploration seismology is the primary application which has motivated the extensive research which has been done on wave propagation in planar layered media. In this application, sources and receivers are placed on the surface of the earth for the purpose of imaging the subsurface structure. From a perspective on the surface, at seismic frequencies, the earth can often be modeled accurately as varying only with depth. The variation with depth is often conveniently thought of as piecewise homogeneous so that the earth structure consists of a stacked system of strong reflecting interfaces.

Although acoustic frequencies differ from seismic frequencies by several orders of magnitude, and although well logging instrumentation is deployed vertically while seismic instrumentation is positioned horizontally, the acoustic well logging problem and the exploration seismology problem are actually closely tied. The analogy between these two geometries is suggested in Figure 1-1. Here we see that in each case the instrumentation is deployed perpendicular to the direction of variation in the earth model. The fundamental difference between the two cases is the interchange of the z and r axes.

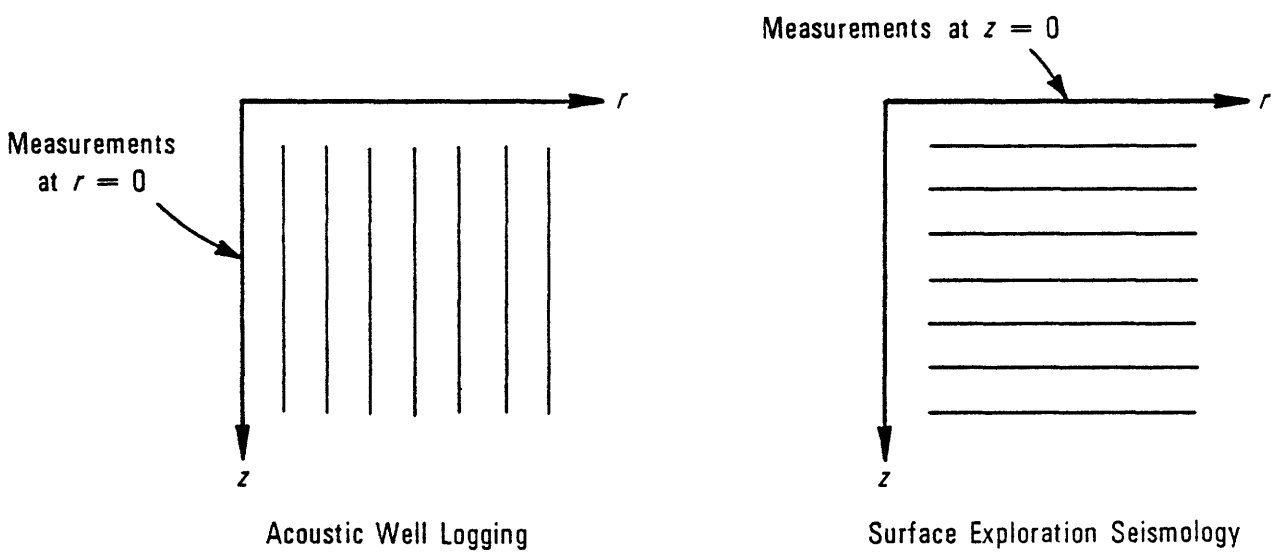

Figure 1-1. The analogy between planar and cylindrical geometries

Unlike the axial dimension, z, the radial dimension, r, is a non-negative quantity. Any

energy propagating toward $r = 0$ in the cylindrical geometry will pass through the axis and propagate back toward the formation. This is not generally true in planar problems since energy propagating upwards can propagate through $z = 0$ and off to $z = -\infty$. However, in exploration seismology, the $z = 0$ plane can often be modeled as a perfect reflector, in which case upgoing energy will reflect off the earth's surface from below and re-enter the formation in a manner analogous to the cylindrical case.

In conclusion, wave propagation in cylindrically stratified media is a central concern of this thesis and arises in the acoustic well logging application. Cylindrically layered media problems are closely tied to planar layered media problems and, in fact, the acoustic well logging problem considered in this thesis is similar in many ways to the surface exploration seismology problem. In treating the acoustic logging problem we will frequently refer to and borrow concepts from the better known seismology problem.

1.2 The Cylindrical Wave Reflection Coefficient

The monochromatic cylindrical wave plays a fundamental role in the study of wave propagation in cylindrically stratified media. This role is analogous to that of the monochromatic plane wave in planar layered media. Specifically, the cylindrical wave is the fundamental solution to the homogeneous monochromatic scalar wave equation in cylindrical axi-symmetric coordinates, just as the plane wave is in Cartesian coordinates. A cylindrical wave can be constructed as an integral of plane waves and general solutions to the homogeneous wave equation can be cast as weighted integrals of either plane or cylindrical waves.

In the same way that a plane wave incident on a planar layered medium results in a reflected plane wave, a cylindrical wave incident on a cylindrically layered medium results in a reflected cylindrical wave. The frequency of the reflected wave is the same as that of the incident wave and the angle of incidence equals the angle of reflection. The only influence which the medium has on the reflection process is to determine the amplitude of the reflected wave, relative to the incident wave amplitude. In fact, the cylindrical wave reflection coefficient is

defined as the ratio of the reflected to incident cylindrical wave amplitudes. This is illustrated in Figure 1-2.

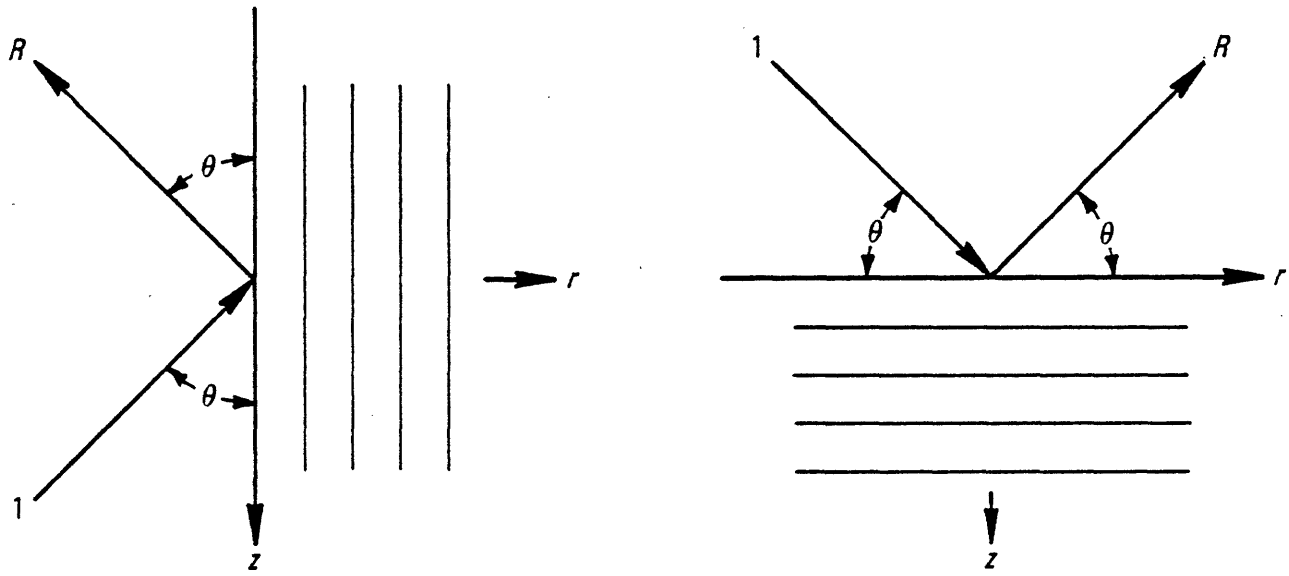

Figure 1-2. The reflection process in planar and cylindrical geometries

Conceptually, the reflection coefficient is the means through which we learn about the formation. Summarized in the reflection coefficient is the "information" regarding the structure of the medium being sensed and a separate problem is the interpretation, or inversion, of the reflection coefficient to recover this structure. For this reason, the reflection coefficient of a layered medium is of fundamental interest.

In Figure 1-3 we show both perspective and contour plots of the magnitude of the theoretical cylindrical wave reflection coefficient as a function of frequency, ω, and the axial component of wavenumber, k_z, for the case of a homogeneous elastic formation model (Chapter IV). Note from this figure that the behavior of the reflection coefficient can be roughly divided into 4 wedge-shaped regions delineated by the three sound speeds in the geometry. These are denoted by v_c, v_s and v_f and correspond to the compressional speed of the formation, the shear speed of the formation and the fluid speed of the mud in the borehole. In typical logging situations, $v_c > v_s > v_f$, as is the case in this figure. Also of interest is the situation where

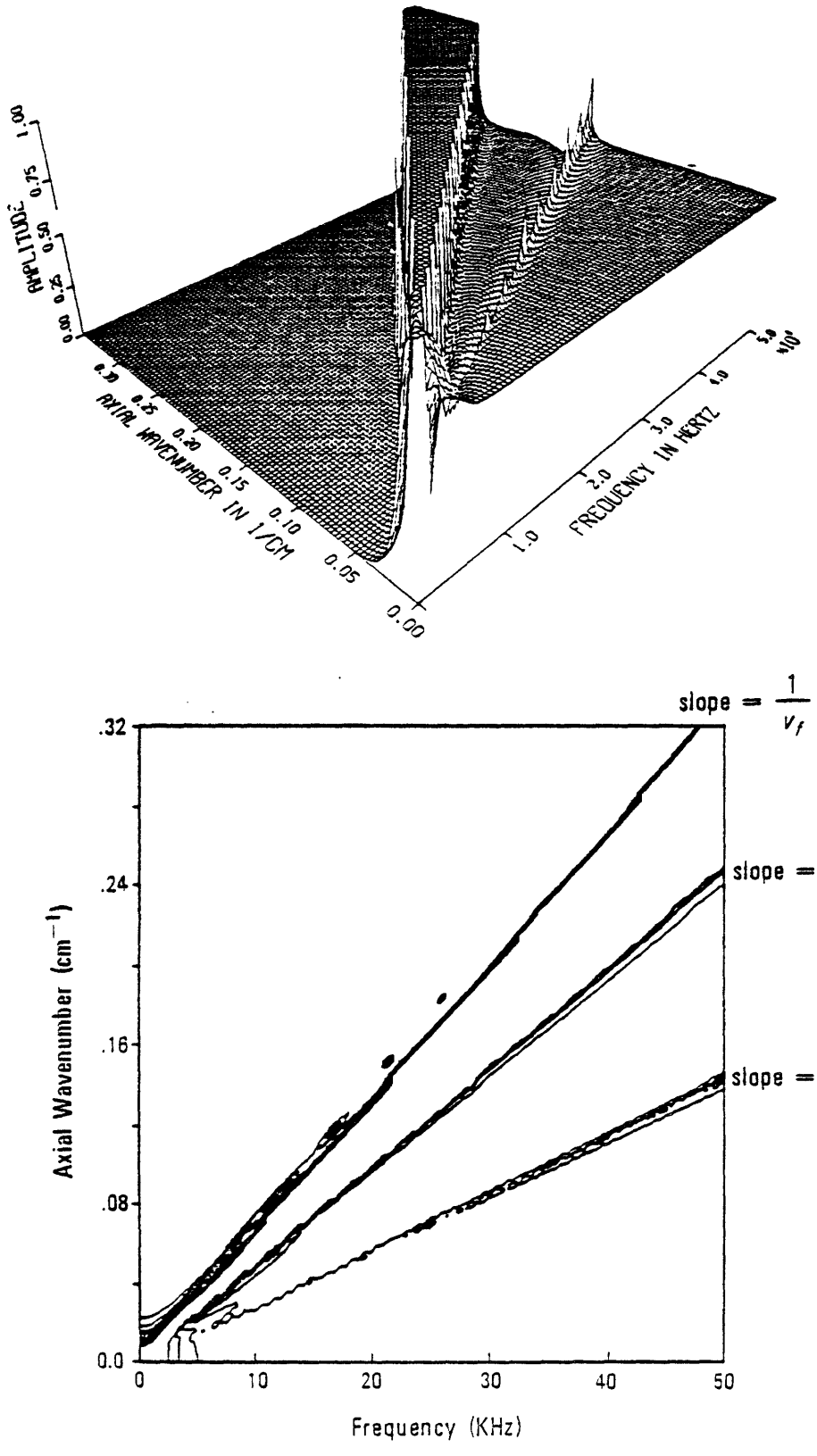

Figure 1-3. The magnitude of the cylindrical wave reflection coefficient

$v_c > v_f > v_s$, sometimes referred to as a "slow formation". However, we do not explicitly treat this case here.

A detailed interpretation of the features of the reflection coefficient shown in Figure 1-3 is given in Chapter II. Briefly, the flat table-like region in the reflection coefficient corresponds to a condition of total internal reflection. That is, an incident cylindrical wave defined by a frequency and wavenumber in this wedge-shaped flat-table region will not transmit a propagating cylindrical wave into the formation but will be entirely reflected into the borehole. The reflection coefficient is complex-valued with unity magnitude in this region and the (k_z, ω) pairs where the phase of the reflection coefficient is a multiple of 2π define the condition for a propagating mode in the borehole. In the region defined by $k_z > \omega/v_f$, on the other hand, the reflection coefficient is essentially zero. This is because the axial component of wavenumber is larger than the total wavenumber, implying that the radial component of wavenumber is imaginary. Thus, this region corresponds to the case of an inhomogeneous incident cylindrical wave which decays exponentially in the radial direction and therefore attenuates significantly in propagating out to the wall and back.

In conclusion, cylindrical waves and the cylindrical wave reflection coefficient play a fundamental role in the study of wave propagation in cylindrically stratified media. The cylindrical wave reflection coefficient carries the information pertaining to the radial structure of the formation and a separate problem is the inversion of the coefficient to obtain this structure. In the case of a homogeneous formation model, the reflection coefficient is directly interpretable in terms of the parameters of the formation.

1.3 Relating the Reflection Coefficient to the Field

The relationship between the cylindrical wave reflection coefficient, $R(k_z, \omega)$, and the acoustic pressure field on the axis of the borehole due to a point source at the origin, $p(z,t)$, is derived in Chapter III and is given by

$$p(z,t) = p_d(z,t) + p_r(z,t) \tag{1.1}$$

where $p_d(z,t)$ denotes the direct component of the total field and $p_r(z,t)$ denotes the reflected component. Physically, the direct field corresponds to energy which has traveled a path directly from the source and is therefore independent of the formation. The reflected component of the field summarizes the effect of the formation on the field. The direct field is a delayed and scaled version of the source pulse, $s(t)$, and is given by

$$p_d(z,t) = \frac{1}{|z|}\, s(t - |z|/v_f) \tag{1.2}$$

while the reflected component of the field can be written in the form of a two dimensional (2D) Fourier transform as

$$p_r(z,t) = \frac{1}{(2\pi)^2} \int_{-\infty}^{\infty}\int_{-\infty}^{\infty} \left\{ S_h(\omega) \sum_{m=1}^{\infty} R^m(k_z,\omega) \right\} e^{-i\omega t} e^{ik_z z}\, dk_z\, d\omega \tag{1.3}$$

where $S_h(\omega)$ is the Fourier transform of the Hilbert transform of the source pulse. Specifically, $S_h(\omega) = 2\pi i\ \mathrm{sgn}(\omega)\ S(\omega)$, where $S(\omega)$ is the Fourier transform of the source pulse.

As we will show, the reflection coefficient is theoretically guaranteed to be less than or equal to unity in magnitude, while if there is the slightest amount of attenuation in the medium, then it will be strictly less than unity in magnitude. Assuming that there is some attenuation present, the integration and summation operations in equation (1.3) can be interchanged so that the field can be interpreted as a sum of individually reflected arrivals. This also allows the reflection coefficient series can be summed in closed form as

$$\sum_{m=1}^{\infty} R^m(k_z,\omega) = \frac{R(k_z,\omega)}{1 - R(k_z,\omega)} = \frac{1}{2} A(k_z,\omega) \tag{1.4}$$

For the case when $S_h(\omega) = 2$, $A(k_z,\omega)$ represents the 2D Fourier transform of the reflected

component of the space-time pressure field along the borehole axis. In Figure 1-4 we show perspective and contour plots of the magnitude of this coefficient.

The mountain-like features which dominate Figure 1-4 correspond to modal phenomena. In the wedge-shaped region defined by the fluid and shear speeds, reflections off the formation are totally internally reflected, interference between the multiples occurs, and modes are formed. Outside this region, interference also occurs between the multiples, but because the reflection coefficient is less than unity in magnitude in this region, the modes are not completely trapped in the borehole and are termed "leaky". Here, the ridges are not nearly as high or sharp. The magnitude in the perspective plot in Figure 1-4 is on a dB scale ($10 \log_{10}$) and the plot was intentionally clipped at -100 dB.

The relationship between the field on the borehole axis and the reflection coefficient can be interpreted in terms of 2D linear space-time-invariant convolutions. Specifically, in Figure 1-5 we show this relation in terms of the 2D Fourier transform of the reflection coefficient, which we will refer to as the reflection coefficient signal and denote as $r(z,t)$. Here we see that the reflection coefficient signal is repeatedly convolved with itself and summed to form the reflected component of the field.

In Figure 1-6 we show a plot of 100 synthetically generated waveforms (Chapter IV) corresponding to $s_h(t) * r(z,t)$, where the asterisk denotes temporal convolution and $s_h(t)$ denotes the Hilbert transform of the source pulse. This figure is in a variable density log (VDL) format where the grey-scale indicates amplitude. In Figure 1-7, we show the corresponding the reflected component of the field, $p_r(z,t)$, also in a VDL format. The reflection coefficient signals in Figure 1-6 correspond to the primary reflection of the source pulse off the formation wall while the reflected component of the field in Figure 1-7 contains the sum of an infinite number of reflections. Comparing these two figures, we see that the reflection coefficient signal is less cluttered than the reflected component of the field. Furthermore, the interference of the multiples in Figure 1-7 produces modal phenomenon which are difficult to interpret in terms of the nature of the formation. The reflection coefficient signals do not contain these complicated

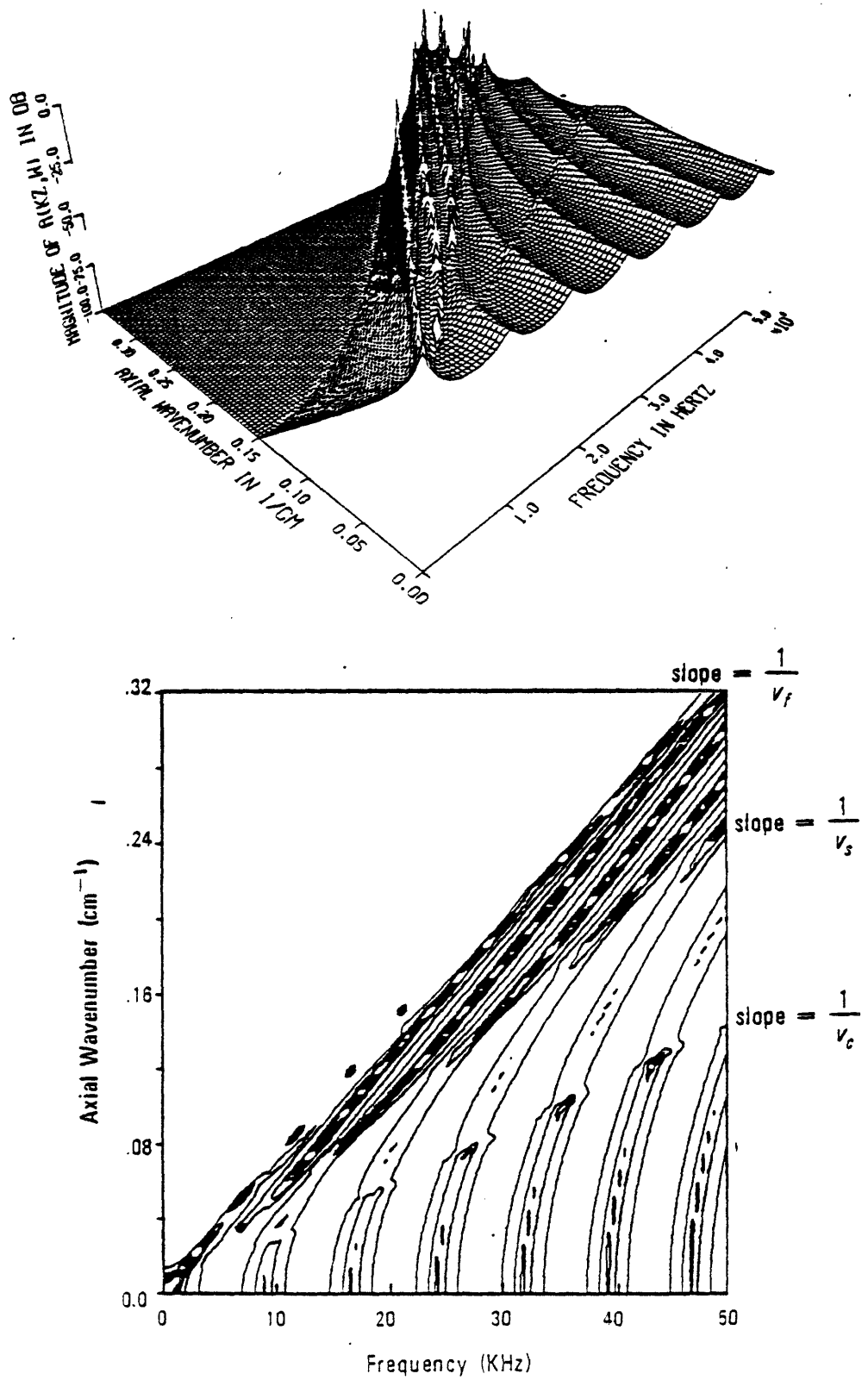

Figure 1-4. The magnitude of the cylindrical wave modal coefficient

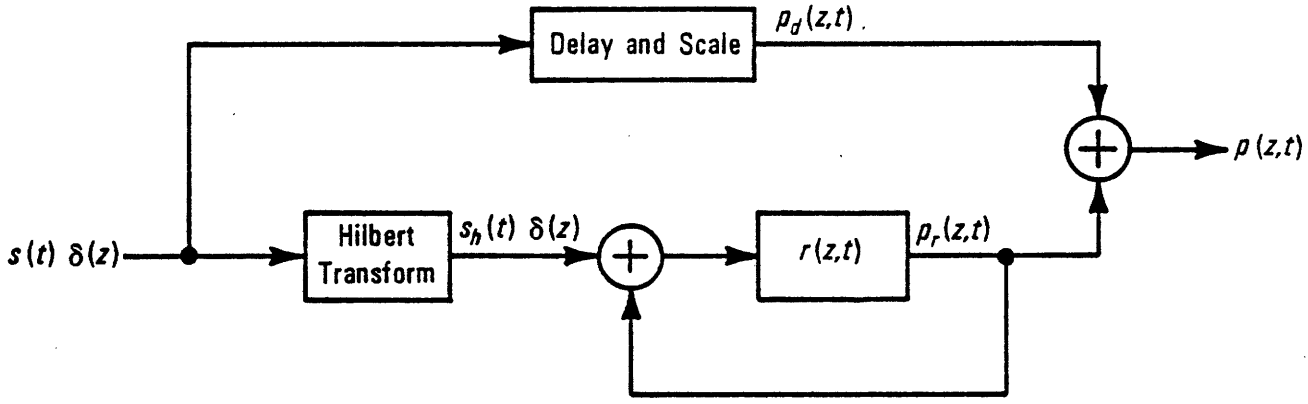

Figure 1-5. Relating the reflection coefficient to the reflected field on the axis

waveguide effects.

In conclusion, the reflected component of the field on the axis of the borehole consists of an infinite sum of reflected arrivals. At acoustic frequencies, these arrivals overlap one another in space and time to produce a complicated wavefield which is difficult to interpret. The reflection coefficient signal, on the other hand, represents the primary reflection off the formation wall and is easier to interpret in terms of the formation parameters. The reflected component of the total field is related to the reflection coefficient signal via a series of 2D space-time invariant convolutions and summations.

1.4 Thesis Problem

In this thesis, we explore the estimation of the cylindrical wave reflection coefficient within the context of acoustic well logging. Specifically, from measurements of the acoustic field on the axis of the hole due to a point source, also on the axis, the problem is to estimate the cylindrical wave reflection coefficient associated with the formation.

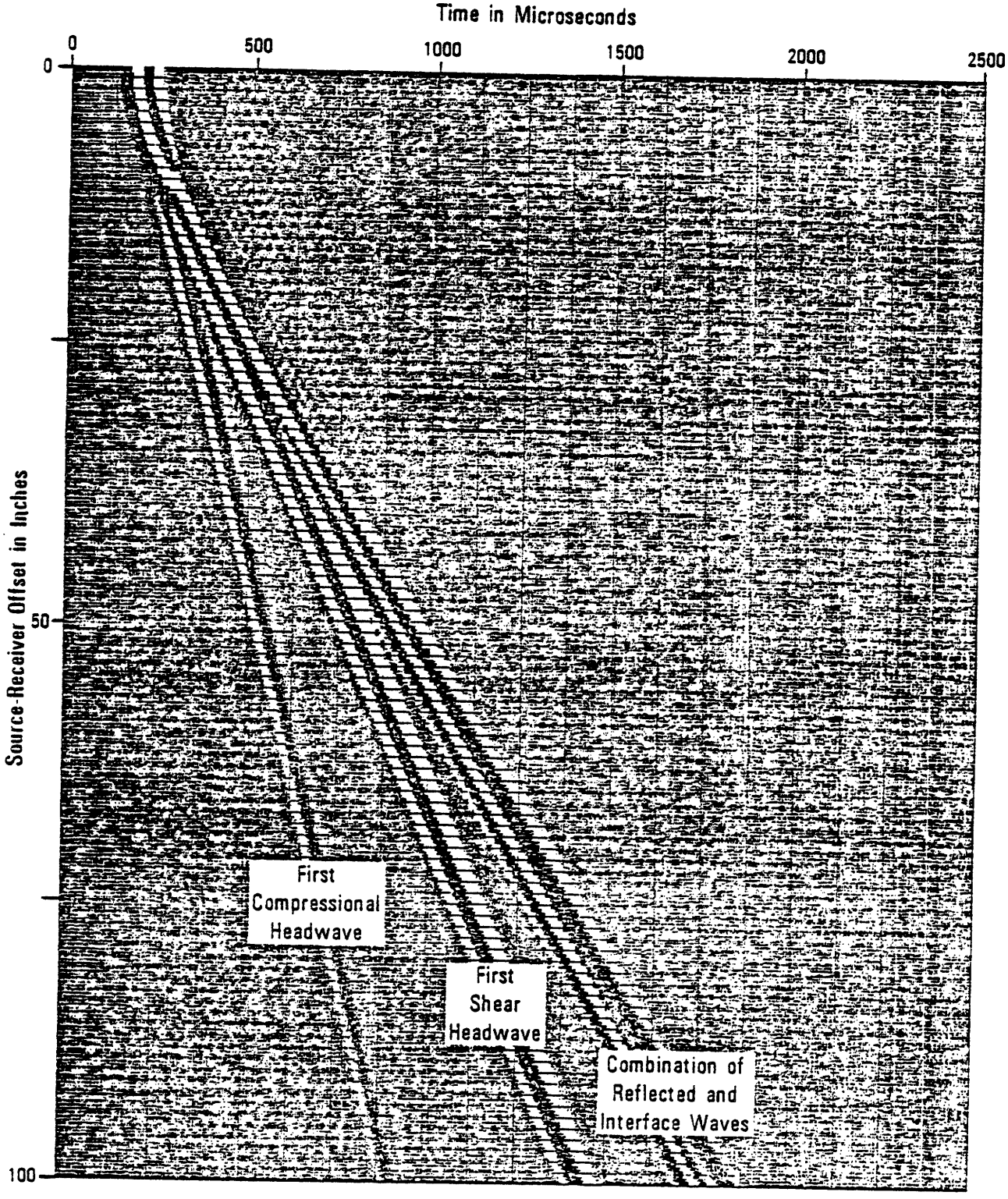

Figure 1-6. $s_h(t) * r(z,t)$, reflection coefficient signals

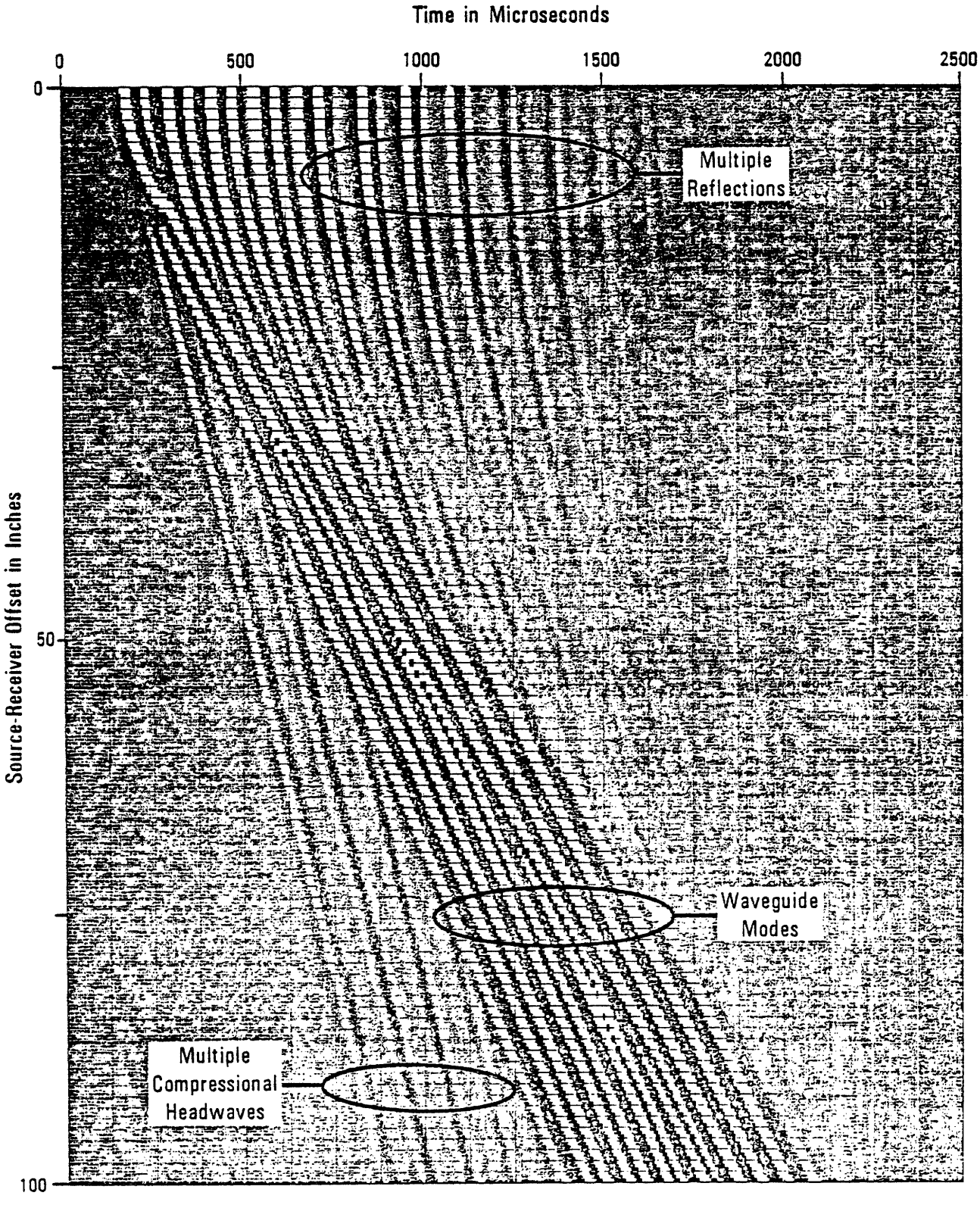

Figure 1-7. $p_r(z,t)$, the reflected component of the total pressure field

The estimation of the cylindrical wave reflection coefficient is complicated by the presence of multiple reflections in the data as well as by the presence of energy which has traveled a direct path from the source. In this thesis, we treat the problem of estimating the reflection coefficient from measurements of the infinite series of reflections in the borehole, but without the presence of the direct arrival. The estimation of the reflection coefficient from the multiple reflections plus the direct arrival is the actual problem of interest but is not treated here. Also not treated here is the problem of inverting the reflection coefficient to recover the radial variation of the formation model.

The reflection coefficient of the formation is a function of both frequency and axial wavenumber and the problem is to estimate this 2D function from space-time data. In this thesis we do not treat this 2D estimation problem, but instead treat a somewhat simpler one dimensional (1D) version of the problem. In this 1D formulation, we estimate the reflection coefficient as a function of frequency but at a single value of axial wavenumber. This corresponds to estimating a slice of the reflection coefficient shown in Figure 1-3 made at a constant axial wavenumber. The procedure we develop for a single wavenumber can, in theory, be repeated for various choices of wavenumber to build up an estimate of the 2D reflection coefficient of interest.

We refer to the reflection coefficient at a single axial component of wavenumber as $R(\omega \mid k_z)$, and its Fourier transform as $r(t \mid k_z)$, and we will estimate this slice of the reflection coefficient from the reflected pressure field at a single axial component of wavenumber, denoted $p_r(t \mid k_z)$. The single wavenumber reflected pressure field can, in theory, be obtained by first removing the direct field from the data and then transforming the remaining reflected field over space and evaluating the result at the desired wavenumber. Alternatively, a phased array of point sources can be used to attain the same result (Chapter V). From equation (1.3) it follows that the relationship between the single wavenumber reflected field and the single wavenumber reflection coefficient signal is given by

$$p_r(t \mid k_z) = s_h(t) * \left\{ r(t \mid k_z) + r(t \mid k_z) * r(t \mid k_z) + \cdots \right\} \tag{1.5}$$

As in the 2D case, we see that the reflection coefficient signal is repeatedly convolved with itself and summed in the model for the reflected field.

Based on equation (1.5) we derive the 1D reverberatory signal processing model shown in Figure 1-8. Here, we have switched to a discrete domain representation of the signals and have introduced observation noise at the system output as well as source noise at the input. The reflection coefficient sequence in this system is modeled as causal and finite in length. The problem is to estimate the elements of the reflection coefficient sequence given the observations and the statistics of the noise processes. The estimate of the slice of the reflection coefficient will be taken as the discrete Fourier transform (DFT) of the estimate of the reflection coefficient sequence.

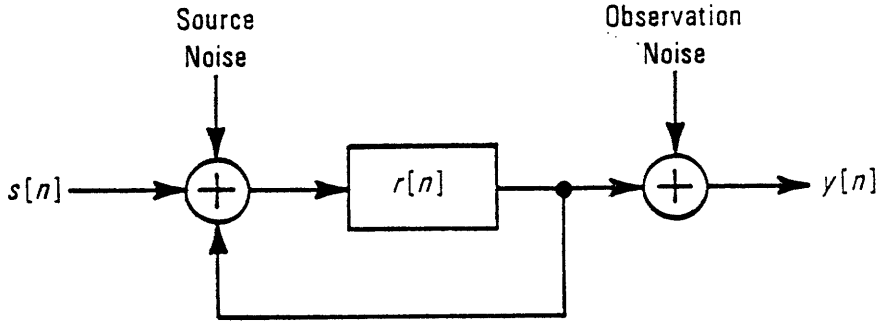

Figure 1-8. The discrete domain dereverberation signal processing model

1.5 Relationship to Other Problems

The problem of estimating the cylindrical wave reflection coefficient is related to a variety of other problems. In this section, we discuss the relationships with several other problems.

1.5.1 Plane Wave Reflection Coefficient Estimation

Estimating the cylindrical wave reflection coefficient in a cylindrical geometry is analogous to estimating the plane wave reflection coefficient in a planar geometry which has a perfect reflector at $z = 0$. In each case, the data will contain a direct arrival from the source as well as an infinite series of multiple reflections. The details of the equations relating the plane wave reflection coefficient to data recorded on the surface will be different than those of the equations relating the cylindrical wave reflection coefficient to data recorded on the axis, however. That is, equations (1.1)-(1.5) will be replaced by their planar geometry analogs. These can be found, for example, in [6].

It should be noted that if the instrumentation is placed in an infinite half-space above a layered medium, as opposed to in a medium topped by a perfect reflector, then the plane wave reflection coefficient estimation problem becomes significantly simpler. In this case there will be no multiple reflections present in the data, but a direct arrival will still be present.

1.5.2 Reflection Seismology

The reflection coefficient estimation objective of this thesis is loosely analogous to reflection seismic methods. In reflection seismology, the receiver array is placed at a short offset from the source so that energy reflected by the subsurface interfaces at normal incidence, or close to normal incidence, will be recorded [10]. The processing of data recorded in this manner typically consists of a three part sequence of operations. The first part consists of a stacking operation while the second part involves the use of predictive deconvolution. These two components of the processing serve to enhance primary reflections in the data relative to both multiples noise. The result is an offset-versus-time data set which will hopefully contain only primary reflections. Thus, these two steps correspond roughly to estimating the reflection coefficient signal, since the reflection coefficient signal is also an offset-versus-time domain signal with no multiply reflected energy.

The third step in the processing of seismic data is one of migration. Here, the data is mapped from the offset-time domain into the offset-depth domain. In this way, an image of the subsurface structure is obtained. In the cylindrical geometry, this operation is analogous to migrating the reflection coefficient signal from the depth-versus-time domain into the depth-versus-radius domain. Viewed another way, this step is loosely analogous to interpreting, or inverting, the reflection coefficient in terms of the radial structure of the formation.

Although we do not investigate the application of reflection seismic processing to borehole applications, it is felt that the stacking-deconvolution-migration approach merits a careful study. To summarize, the approach is to estimate the reflection coefficient signal, rather than the reflection coefficient itself, and then migrate the result from the $z-t$ domain into the $z-r$ domain. The primary complication here is the fact that the interesting reflectors in the borehole problem are weak, while those in the planar problem are strong.

1.5.3 Existing Acoustic Logging Methods and Refraction Seismology

The reflection coefficient estimation approach to the acoustic well logging problem is distinctly different from the existing approach to acoustic logging. In the existing approach, energy refracted, rather than reflected, by the formation is analyzed by the processing. From the travel-time information from the source to receiver, or more specifically, from the derivative of travel-time with respect to source-receiver offset, the velocity structure of the formation with depth can be inferred (Chapter II).

While the reflection coefficient estimation approach investigated in this thesis is closely related to reflection seismic methods, the existing approach to acoustic logging is closely related to refraction seismic methods. There, the receiver array is placed at a large offset from the source where refracted arrivals reach the surface. From the arrival-time information observed across the array, the subsurface velocity structure can be inferred. The analogy between conventional acoustic logging methods and refraction seismology is suggested in Figure 1-9.

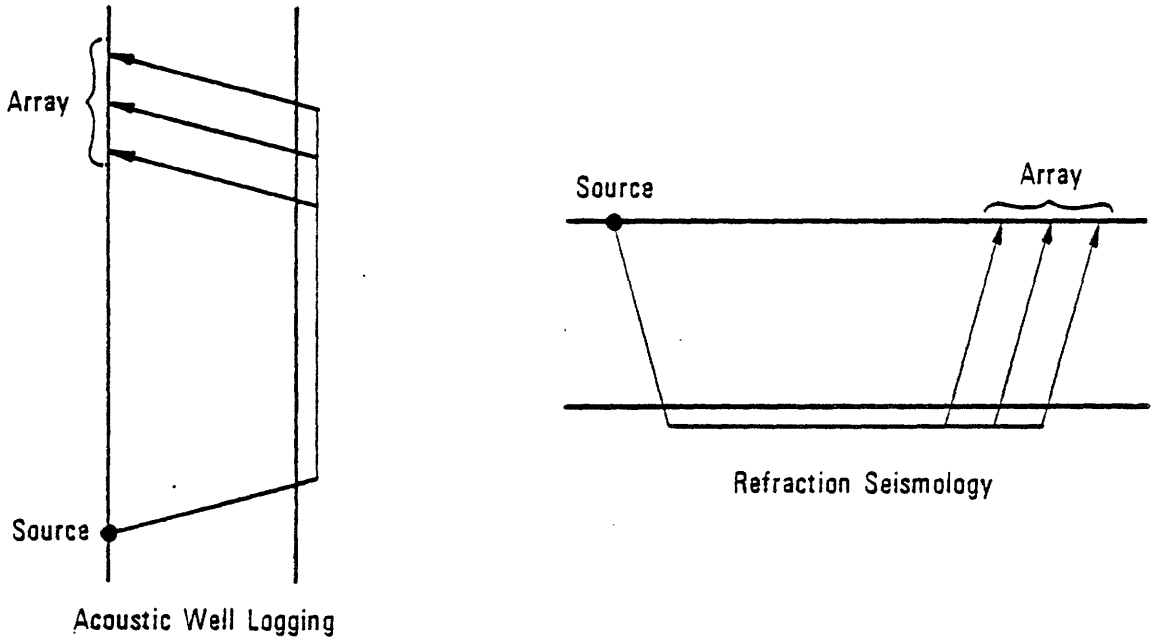

Figure 1-9. The analogy between acoustic logging and refraction seismology

1.5.4 Dereverberation and Pole-Zero Estimation

The reflection coefficient estimation problem is a signal processing problem of dereverberation, or equivalently, of removing multiples, as discussed earlier. Thus, the reflection coefficient estimation problem is similar to other problems which fit the same reverberatory model. More generally, the problem we treat here is a special case of a pole-zero estimation problem. Specifically, we have noisy observations of the output of a rational system driven by a random process. The identifying feature of the problem treated here is the way we have parameterized the rational system. As an alternative, we might have modeled our observations as the output of a pole-zero model, or an all-pole model, etc., estimated the model parameters and then mapped them into reflection coefficient sequence elements of interest.

1.6 Thesis Outline

The problem investigated in this thesis is treated in the course of the next six chapters. We briefly outline the contents of these chapters here.

In Chapter II, we present the acoustic well logging application of this thesis in some detail.

Here, we present the existing well logging method within the context of travel-time inversion before focusing on the proposed reflection coefficient estimation approach. We motivate this new approach by demonstrating the sensitivity of the reflection coefficient to the parameters of the formation for the case of a homogeneous formation model.

In Chapter III we study acoustics in cylindrically stratified media. Here we develop the properties of monochromatic cylindrical waves, and of the cylindrical wave reflection coefficient, and compare these properties to the properties of their plane wave counterparts. In addition, we develop the theoretical relationship between the cylindrical wave reflection coefficient and the field on the axis of the borehole given by equations (1.1) through (1.5). In this way, a physically-based model is obtained which relates the data to what we wish to estimate.

In Chapter IV, we discuss the numerical evaluation of the theoretical field on the axis of the hole. Arrays of synthetic data simulated in this manner will serve later as the data base upon which we test and evaluate the reflection coefficient estimation method we develop. Synthetic data is preferable to laboratory or field data in this application because the underlying formation model and noise levels are under control, as is the instrumentation design. This allows for a meaningful evaluation. The major finding in this chapter is that, through the use of table lookup and interpolation methods for evaluating Hankel functions for complex-valued arguments, the computation time needed to generate the data can be reduced by roughly an order of magnitude. This significant savings in computation time has made synthetic data a useful tool in acoustic logging related research, whereas before this development, it was far less useful.

In Chapter V, we develop a signal processing method to treat the reflection coefficient estimation problem. We first identify the 1D single wavenumber signal processing model we will be treating and then parameterize the problem as in Figure 1-8. Following this, we assume that the noise processes are jointly Gaussian and adopt a maximum likelihood (ML) estimation criterion. The estimation problem is seen to be nonlinear and we apply an iterative method due to Musicus [23]. Although Musicus applied the iterative theory to a Gaussian ML pole-zero estimation problem, we find that the method applies equally well to the dereverberation problem

here. In fact, the two problems are closely related; the dereverberation problem is equivalent to a pole-zero estimation problem in which the poles and zeros are related. The iterative dereverberation method is guaranteed to increase the log likelihood function with each pass but the sequence of estimates produced by this method is not guaranteed to converge. The method reduces the original nonlinear problem to an iterative procedure requiring the solution to two interconnected linear estimation problems in each pass and efficient computational methods have been developed to implement the method.

In Chapter VI, we apply the iterative ML technique to arrays of synthetic data. Through a sequence of experiments, we test and evaluate the performance of the iterative ML dereverberation scheme. We find that, at a single axial component of wavenumber, the reflection coefficient cannot be reliably estimated at those frequencies outside the passband of the source pulse or at those frequencies which excite modes. Within the source passband the estimation performance depends strongly on the signal-to-noise ratio and the specific array design.

Finally, in Chapter VII, we outline the contributions of this thesis as well as promising areas for further investigation. Here, we identify new areas of research relating to acoustic logging as well as remaining areas relating to the reflection coefficient approach investigated here.

II. ACOUSTIC WELL LOGGING

2.1 Introduction

In this chapter, we discuss the problem of acoustically imaging the formation structure from a perspective within a borehole. Specifically, using acoustic sources and receivers in the hole, the problem is to resolve the spatial variation of the acoustic properties of the formation. This *imaging* viewpoint is a generalization of the classical *logging* perspective in which a one dimensional (1D) image of the formation variation with depth, called a *log*, is the objective. Here, we extend the logging approach to include the radial dimension, in addition to the axial dimension, and our objective is now a two dimensional (2D) image of the formation, rather than a 1D log.

We begin this chapter with some background on the nature of the borehole environment and the general problem addressed by the well logging industry [3][13][28][34][35]. This is followed by a discussion of fundamental acoustic imaging concepts within the context of well logging. We then present two approaches to acoustic imaging; the first is based on the principle of refraction, while the second is based on a reflection concept. Refraction-based imaging methods include the existing approach to acoustic logging [4][19][20][29] while reflection-based methods include the proposed reflection coefficient estimation approach proposed in this thesis.

By presenting the application of this thesis in this manner, we develop an understanding of the general well logging problem, the contribution of acoustic methods toward solving this problem, the various approaches to acoustic logging, and how the proposed reflection coefficient method and existing refraction-based method fit into a general acoustic logging framework.

2.2 Background

As an oil or gas well is being drilled, mud is continually being pumped into the hole to

cool off the drill bit and carry away the pieces of broken rock. The mud has been specially weighted so that the pressure which the mud column exerts against the formation wall is enough to prevent the passage of formation fluids and gasses into the borehole. In this way, if a highly pressurized oil or gas zone is pierced by the well, a dangerous blow-out is averted. In fact, the pressure which the mud column exerts on the formation is usually so great that a filtrate of the mud is forced into the virgin formation. This creates what is known as the *invaded zone* of the formation and is one source of radial variation in the formation.

By design, the mud will quickly tend to cake along the borehole wall. The mud cake is essentially impermeable and serves to isolate the borehole fluids from the formation fluids and gasses and thus halt the invasion process. The invaded zone will then diffuse into the formation very slowly with time, perhaps on the order of months.

Besides infiltrating the virgin formation with borehole fluids, the drilling process also disturbs the natural stress field in the formation. In effect, the drilling process produces stress concentrations at the borehole wall which are strongly anisotropic but decrease rapidly with distance from the borehole. Distinct from the invaded zone, this region is referred to as the *altered zone* of the formation. As with the invaded zone, the altered zone will relax over a period of time, perhaps on the order of days, to a new state of static stress. The altered zone, invaded zone and mud cake are depicted in Figure 2-1.

After the well has been drilled and the drill pipe has been removed from the hole, what remains is a mud-filled borehole perhaps 2 or 3 miles deep. At this point, little is known about the structure of the formation which was drilled through, especially if the well is the first one in a particular area. In fact, it is entirely possible that if an oil or gas reservoir was pierced by the well there would be no indication of this at the surface. This then motivates the need for a well logging operation.

The primary objective of the logging operation is to resolve the *porosity* (i.e. the percent of a local volume which is comprised of pores, or cavities) of the virgin formation as a function of

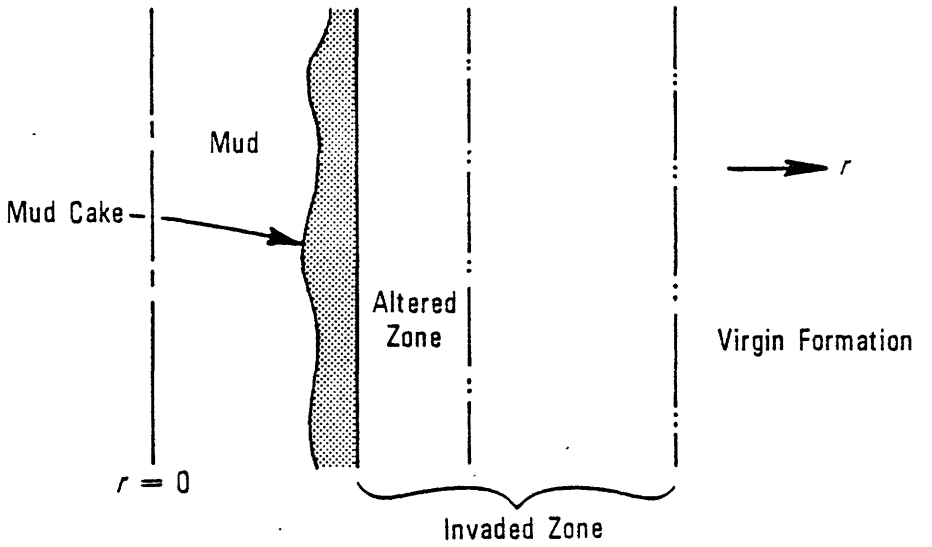

Figure 2-1. The borehole environment

space in the vicinity of the hole and the associated *hydrocarbon saturation* (i.e. the percent of the pore space which is comprised of hydrocarbons). In addition, the *permeability* of the formation (which indicates the connectedness of the pores) must be estimated so that expected flow rates can be computed.

Following the determination of these quantities is the decision as to whether or not to produce from the well. If the well is to go into production, a steel casing is cemented to the formation wall and the mud is pumped out. The casing is then perforated at the decided depth and the hydrocarbon reserves are permitted to escape up the hole in a controlled fashion.

Well logging methods determine the formation porosity, permeability and hydrocarbon saturation in an indirect fashion. A series of logging "tools" are suspended via wireline (i.e. a communication cable) into the borehole. Each of the tools has been designed with a specific measurement objective in mind, however, none of these directly measures the desired quantities. The existing, or conventional, sonic (i.e. acoustic) tool measures the acoustic velocities of the formation, a tool with a neutron source senses the density of the formation, an electrical tool measures the formation resistivity, etc. A well logging interpretation expert and an "intelligent"

computer program are used in conjunction to deduce the desired information from those measurements which are indeed made. This interpretation step is not easily quantified since a great deal of experience with the particular geologic area and educated guess work are typically required.

In this thesis, we limit our attention solely to the acoustic approach to well logging. As the name implies, this approach explores the acoustic properties of the formation in the vicinity of the borehole. The interpretation of the acoustic properties of the formation in terms of the hydrocarbon-related questions of interest is not considered here.

2.3 Acoustically Imaging the Formation from a Perspective Within the Borehole

In acoustic well logging, an acoustic source (or array of sources), and an array of receivers are lowered into the borehole for the purpose of learning about the acoustic properties of the formation which surrounds it. The source excitation is designed to "probe" the formation in some desired fashion and the elements of the receiver array are placed so as to record the formation "response". We learn about the formation, then, by analyzing this response.

The objective of acoustic logging (i.e. of analyzing the formation response) is to resolve one or more acoustic properties of the formation as a function of space. By resolving any one property, we effectively build a three dimensional (3D) acoustic image of the formation as seen through that property. In many instances, the variation in the angular dimension, θ, is weak, in which case a 2D image of the formation in r and z is sufficient. In still other instances, the radial variation in the formation (i.e. the invaded and altered zones) is either not appreciable or not interesting, relative to the axial variation. In this case, one may wish to image (i.e. log) only the 1D depth variation of the formation.

An important issue in any imaging system is that of resolution. In the following sections, we discuss the fundamental limits of resolution (i.e. how small a structure can be resolved), the resolution of large formation structures, the resolution of structure which is distant from the

borehole and the problems associated with viewing the formation from a perspective in a borehole.

2.3.1 Fundamental Resolution Limits

Acoustic logging methods are only capable of resolving structure in the formation which is larger than, or on the order of, the wavelengths associated with acoustic frequencies. Structure in the formation which is much smaller than a wavelength is, in effect, not "seen" in this frequency range. Rather, a wave with a particular wavelength tends to average, or smooth, the underlying fine structure in the formation over the distance of roughly a wavelength. Thus, for practical purposes, we can imagine spatially low-pass filtering, or smoothing, the actual structure of the formation over distances of an acoustic wavelength to obtain a new formation structure which is, in some sense, the highest resolution image we can expect.

The term *acoustic*, or *sonic*, implies frequencies which are in the range of 1 KHz to 50 KHz. (Frequencies much higher than this are termed *ultrasonic*, while those which are much lower are referred to as *seismic*.) The wavelengths associated with acoustic frequencies depend upon the sound speeds encountered in typical earth formations and drilling muds. Specifically, the wavelength, λ, associated with a given frequency, f, is determined by the sound speed of the medium, c, via the relation $\lambda = c/f$. For example, in the borehole mud, which has a sound speed of roughly 1.5 Km/s, the wavelength at 1 KHz is approximately 5 feet while the wavelength at 50 KHz is only 1 inch. In a formation with a sound speed of 3 Km/s, these wavelengths are doubled.

We conclude that acoustic well logging methods are fundamentally limited in spatial resolution to features which are on the order of inches, or greater. Structure in the formation which is smaller than a few inches in size will be difficult to resolve at acoustic wavelengths and will be smoothed in an acoustic image of the formation.

2.3.2 Resolving Global Structure

An acoustic source within the borehole will illuminate a region of the formation local to the source. This region is typically on the order of tens of wavelengths in size. Formation structures which are tens or hundreds of wavelengths in size are resolved by raising, or lowering, the instrumentation in the hole to various depths and repeating the local probe/response experiment.

An issue here is the frequency with which one performs a local acoustic experiment in the hole. If the depth interval between experiments is sufficiently large, then the data from each experiment is independent of the data from other experiments. In this case, the global resolution problem reduces to a series of independent local resolution problems. On the other hand, if successive experiments are investigating overlapping regions of the formation, then the data from successive experiments is correlated. In effect, data from all the local experiments associated with a given depth interval should be used in learning about that depth interval.

2.3.3 Resolving Structure Distant from the Borehole

As discussed in Section 2.2, the drilling process disturbs the virgin formation in the vicinity of the hole. Specifically, we imagine the invaded and altered zones which begin at the borehole wall and disappear gradually with increasing radial distance into the formation. The presence of these zones poses a problem from the standpoint of making measurements of the virgin formation. In effect, a logging method must be able to "see" beyond the invaded and altered zones and into the virgin formation. Alternatively, if the logging measurement senses only a small distance into the formation, one must understand the effects of the contamination on the properties being measured and compensate them appropriately.

Ideally, one would like to resolve the properties of the formation as a function of both r and z. In this way, an image of the contamination due to drilling could be constructed along with the natural layering of the rock formations. An issue here is the maximum distance into the formation that a particular method can sense. This limit is referred to as the *depth of investigation* of the method. The radial resolution problem, then is to image the variation in r out to the

depth of investigation.

The depth of investigation of an acoustic logging method depends strongly on the formation itself, and in particular, on the nature of the virgin formation fluids relative to the invasion fluids. Specifically, in order to image a structure at a given radial distance into the formation, acoustic energy must penetrate the formation to at least that distance and then must reflect or refract and return to the hole where it can be sensed. If the invaded zone is faster than the virgin formation (i.e. if the sound speed in the invaded zone is greater than that in the virgin formation), which is not usually the case, then any rays which enter the virgin formation will not return to the borehole and the virgin formation will be difficult to sense. On the other hand, if the virgin formation is faster than the invaded zone, then energy will reflect or refract as a result of the impedance contrast and return to the hole.

In conclusion, there is often an issue in well logging as to whether a given measurement corresponds to of the virgin formation, or to the invaded zone, or to the altered zone, or to some combination of these. In order to resolve this issue, one must at the very least have a feel for the depth of investigation of the method and the extent of the disturbed zones. Ideally, one would like to have a method which senses the formation at various radii so that the radial variation in the formation can be resolved. Acoustic logging methods offer some capabilities in this regard, particularly if the acoustic velocities increase with distance from the hole.

2.3.4 The Perspective Within the Borehole

Acoustically imaging the formation structure from a perspective within the borehole is a fundamentally difficult task. The borehole tends to prevent the source energy from entering the formation by reflecting it inwards. This internally reflected energy then gives rise to additional internal reflections which overlap with each other in space and time. The interference between the multiples produces modal phenomena which are guided by the hole to large axial distances from the source and as a result, it is difficult to "see" what is outside the hole. Viewed in reverse, it is easy to see the hole itself, which makes the problem of seeing the formation

difficult. A central issue in any acoustic logging method then is separating the interesting formation-dependent information in the measurements from the uninteresting information due solely to the fact that we are making the measurements in a waveguide.

The primary reason for the large effect which the borehole has on the wave propagation is due to the use of the acoustic frequency range. Acoustic wavelengths are on the order of the size of the hole and therefore, acoustic waves are affected by the hole. At seismic frequencies, the wavelengths are much longer and the waves cannot resolve the hole. At ultrasonic frequencies, the hole is many wavelength across so that individual reflections off the formation can be identified and isolated. In this sense, acoustic frequencies are a particularly poor choice for well logging applications.

2.4 Refraction-Based Acoustic Imaging

In this section, we present the refraction concept upon which the existing acoustic logging method is based (there is only one existing method). We then present a brief analysis of the method and identify the limitations of this approach. Following this, a travel-time inversion approach to refraction-based acoustic logging is presented which may serve as the basis of a two dimensional (2D) acoustic velocity imaging system. The conventional logging method can be viewed as a special case of the travel-time inversion problem, or equivalently, the travel-time inversion problem can be viewed as a generalization of the conventional approach.

2.4.1 The Existing Velocity Logging Method

Fermat's principle of least-time states that the first arrival of energy at a receiver will have traversed a least-time path from the source. If we imagine the formation as a homogeneous solid, then at sufficiently long source-to-receiver spacings, the fastest path from the source to the receiver consists of a ray from the source to the formation, along the wall of formation, and then back to the receiver, as shown in Figure 2-2. While in the borehole, the energy propagates at the sound speed of the mud, whereas in the formation, the energy propagates at the

compressional velocity of the formation. The energy which travels this path is called the first compressional headwave and is a refracted arrival much like those found in planar layered media. This arrival is relatively small in amplitude, but because it is the first energy to arrive, it is easily detected.

The arrival time of the first compressional headwave, t_c, can be derived from the geometry shown in Figure 2-2 as

$$t_c = \frac{z}{v_c} + \frac{2a}{v_f}\sin(\theta_c) \quad \text{for} \quad z > 2a\tan(\theta_c) \quad \text{where} \quad \cos(\theta_c) = \frac{v_f}{v_c} \tag{2.1}$$

Here, v_c and v_f denote the compressional sound speed in the solid (formation) and the sound speed in the fluid (mud), respectively. The source-receiver spacing is denoted by z and the borehole radius by a. The angle the least-time ray makes with the formation, θ_c is known as the compressional critical angle.

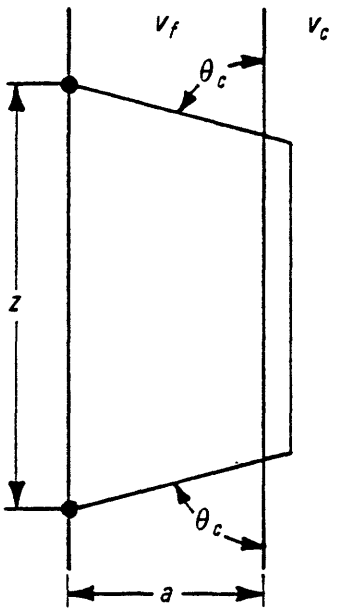

Figure 2-2. The least-time ray

From the z dependence in this relation we see that the first compressional headwave will travel across the array with a velocity equal to the compressional velocity of the formation,

Thus, by estimating the velocity of the first compressional headwave across the array, we may infer the compressional velocity of the formation in the vicinity of the array aperture.

This least-time ray concept is the basis of the conventional, or existing, approach to acoustic logging. A receiver array is placed in the borehole many wavelengths from the source. Signal processing methods are designed to look for coherent energy propagating across the array with a *linear moveout* (i.e. a constant speed across the array). The speed of propagation is then estimated and taken to be the compressional speed of the formation in the vicinity of the array. Then, to resolve the velocity structure of the formation with depth, the source and receiver array are shifted in the hole and the experiment is repeated. In this way, velocity estimates are obtained at regular depth intervals in the hole and a compressional velocity log is obtained.

Assuming that the shear velocity of the formation, v_s, is greater than the fluid speed in the borehole, v_f, there is a first shear headwave, just like the first compressional headwave, in the sense that it travels a similar path. The difference is that the critical angle is smaller and that the wave travels at v_s in the formation, not at v_c. Thus, there is energy which propagates across the receiver array with speed v_s as well as v_c. In fact, the same coherence-based processing methods that are used to estimate the compressional speed can also be used to estimate shear speed. In this way, a shear velocity log is obtained in addition to the compressional velocity log.

a. Analogy with Refraction Seismology

The analog of the acoustic well logging problem in a planar geometry is the surface refraction seismology problem. In this problem, an array of geophones is placed on the surface of the earth many wavelengths from a seismic source. The source energy is refracted by the layers in the earth and is received at the array. From the velocities of coherent energy propagating across the array with a linear moveout, the acoustic speeds in the layers below can be inferred.

The analogy between acoustic logging and refraction seismology becomes closer if the

planar geometry consists of a shallow (relative to a wavelength) water layer above an infinite solid half-space. This is suggested in Figure 2-3. Here, the water layer is analogous to the borehole mud and the solid earth is analogous to the downhole formation. As in the borehole case, the shallow water layer will tend to trap the source energy and guide it to large distances in the form of modes.

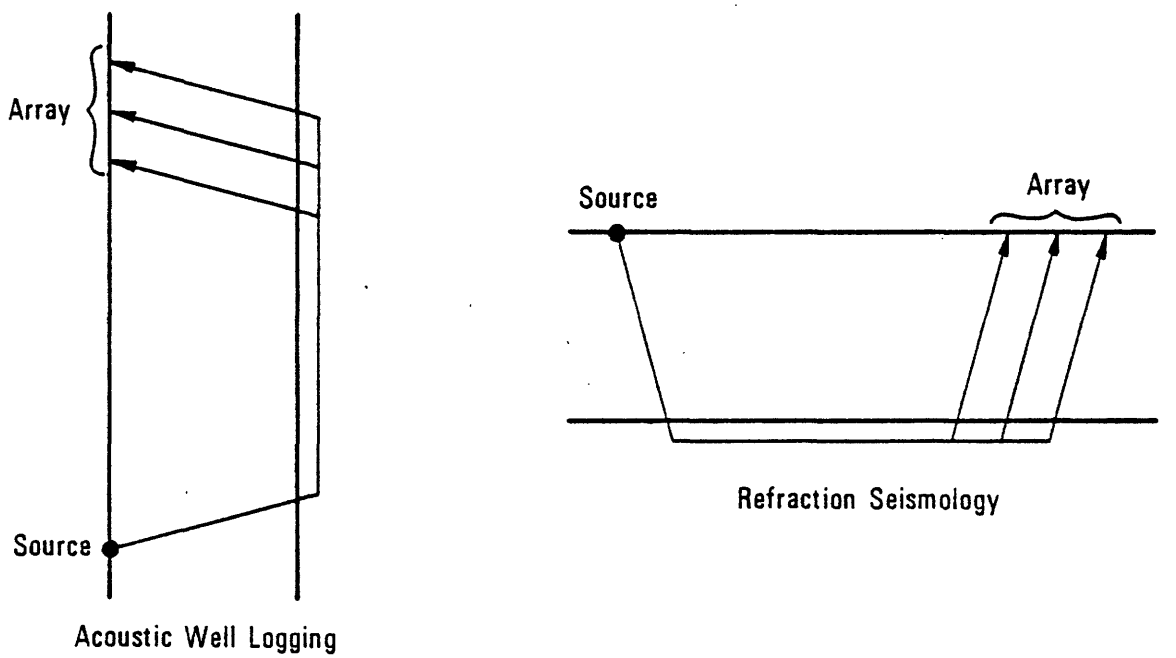

Figure 2-3. Planar and cylindrical geometry analogs

b. Analysis

Conventional acoustic logging is a refraction-based method which assumes that the formation is homogeneous across the array aperture. The method relies primarily on the existence of coherent energy propagating across the receiver array with a linear moveout. If, for whatever reason, there is no such coherent energy in the waveforms, then the method will not perform well. If there is such coherent energy in the waveforms, then there is the issue of interpreting the estimated velocities in terms of formation velocities. Here, the depth of investigation, relative to the thicknesses of the altered and invaded zones, plays a role in the interpretation.

The conventional well logging method is limited in two fundamental ways. First, the method assumes that the formation adjacent to the array is homogeneous when in fact, it will generally vary both axially and radially over distances on the order of the smallest wavelength. Secondly, the method does not exploit the correlation between successive local experiments even though the array shifts only a fraction of its aperture between successive local experiments.

2.4.2 Travel-Time Inversion

Refraction-based well logging methods can be extended beyond the current approach to incorporate a more realistic formation model and to exploit the correlation between successive local experiments. Here, we study the effects of more complicated formation models on the refracted arrivals and, in particular, discuss the problem of inverting travel-time data associated with successive local experiments to recover the velocity structure of the formation.

a. A Cylindrically Layered Formation Model

A cylindrically layered formation model is one which varies in r, but not in either z or θ. In Figure 2-4 we show a special case of such a model which consists of a system of piecewise homogeneous concentric layers. In the limit as the layer thicknesses become small relative to the wavelengths involved, this layered model can be used to accurately approximate a continuously varying formation. For this reason, we only consider the piecewise constant model here.

The time of first arrival of refracted energy associated with the k^{th} interface in this model can be obtained directly from the geometry in Figure 2-4. We find that

$$t^{(k)} = \frac{z}{v_k} + c^{(k)} \qquad \text{for} \qquad z > z^{(k)} \tag{2.2}$$

where

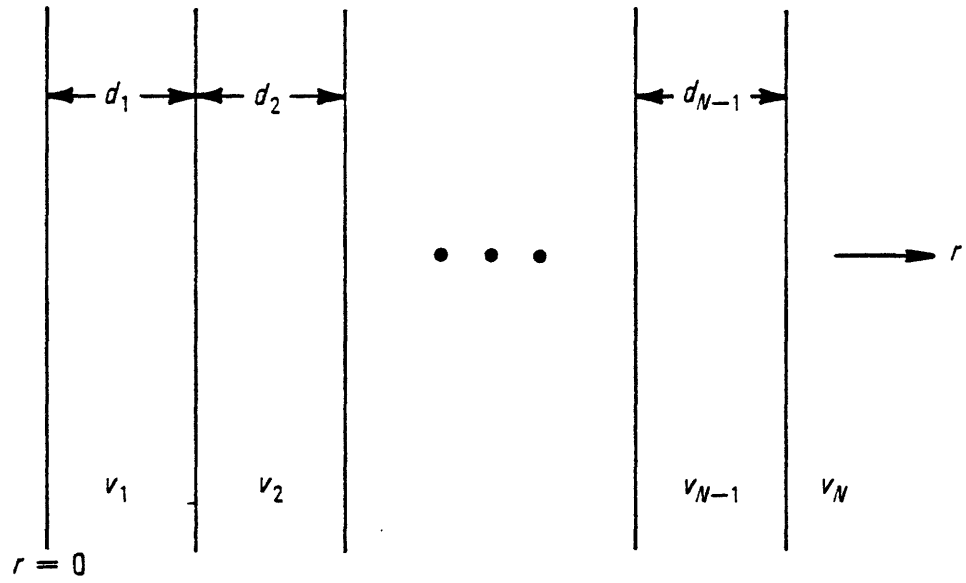

Figure 2-4. A cylindrically layered formation model

$$c^{(k)} = \sum_{j=1}^{k-1} \frac{2d_j}{v_j} \sin(\theta_j^{(k)}) \quad \text{and} \quad z^{(k)} = \sum_{j=1}^{k-1} 2d_j \tan(\theta_j^{(k)}) \quad \text{with} \quad \cos(\theta_j^{(k)}) = \frac{v_j}{v_k} \tag{2.3}$$

Here we have assumed that $v_1 < v_2 < v_3 < \cdots < v_N$ with $k = 1, 2, \cdots, N$. The notation used in equations (2.2) and (2.3) is defined in Figure 2-4. Also, the $k = 1$ arrival time corresponds to the direct arrival from the source to the receiver, and not to a refracted arrival.

From this result, we see that the refracted arrival associated with each layer is a straight line in the $z-t$ plane. The slope of each line corresponds to the velocity of one of the layers while the intercepts of the lines (i.e. the $c^{(k)}$'s) and the minimum offsets (i.e the $z^{(k)}$'s) each contain the layer thickness information. Moreover, the minimum offsets and the intercepts are each linear functions of the layer thicknesses.

In Figure 2-5, we show the collection of refracted arrivals in the space-time domain. From a large aperture receiver array in the borehole, with dense spatial sampling, one can imagine recording and resolving these refracted paths. Following this is the problem of inverting the refracted arrival information to obtain the radial velocity structure of the formation. Here,

the issue of the uniqueness of the formation structure is important. That is, is there only one velocity structure as a function of r which corresponds to the travel-time curves which were observed?

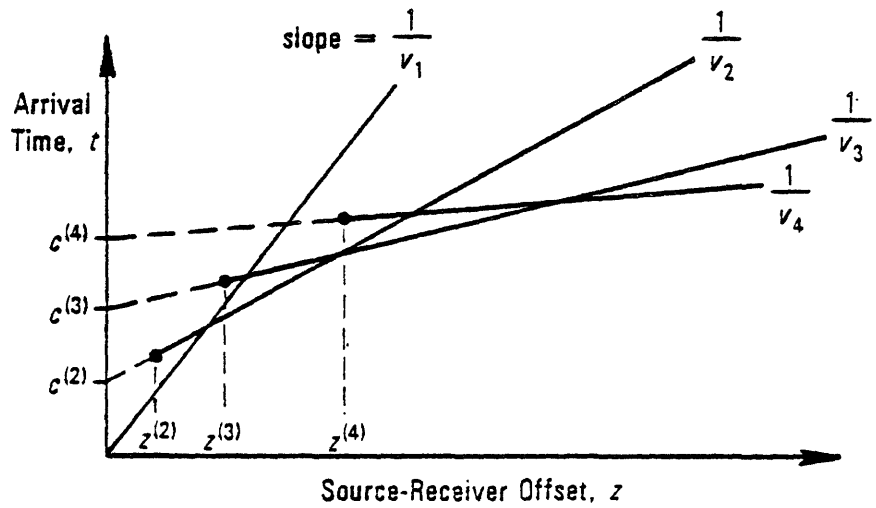

Figure 2-5. The collection of refracted arrivals from each layer

In partial answer to this question, we now show that from first-arrival-time information only, the determination of a consistent velocity structure is straightforward but the result is not unique. To see this, suppose that the first-arrival-time curve consists of N straight line segments and also suppose that the slopes of each segment can be determined as well as the t-axis intercepts (i.e. the $c^{(k)}$'s). Since the slopes give the velocities directly, the layer thicknesses can be obtained as the solution to the following lower triangular system of linear equations.

$$\begin{bmatrix} \alpha_1^{(2)} & 0 & 0 \\ \alpha_1^{(3)} & \alpha_2^{(3)} & 0 \\ \alpha_1^{(4)} & \alpha_2^{(4)} & . \\ . & . & . \\ . & . & \alpha_{N-1}^{(N)} \end{bmatrix} \begin{bmatrix} d_1 \\ d_2 \\ . \\ . \\ d_{N-1} \end{bmatrix} = \begin{bmatrix} c^{(2)} \\ c^{(3)} \\ . \\ . \\ c^{(N)} \end{bmatrix} \tag{2.4}$$

where

$$\alpha_j^{(k)} = \frac{2\sin(\theta_j^{(k)})}{v_j} = \frac{2\sqrt{v_k^2 - v_j^2}}{v_k\, v_j} \tag{2.5}$$

Alternatively, if the minimum offsets were measured, the layer thicknesses could also be found as the solution to a different lower triangular set of linear equations. In each case, the solution to these equations is unique and can be solved efficiently in a recursive fashion.

Although the solution to the above set of equations is unique and consistent with the first-arrival-time curve, there are an infinite number of structures which have this same first-arrival-time curve. In Figure 2-6 we illustrate the non-uniqueness issue with a simple two-layer example. The first-arrival-time curve for case labeled as "unique" in Figure 2-6 consists of three straight-line segments. At short offsets, the direct arrival is first to arrive, at intermediate offsets the refraction associated with the first interface arrives first, while at large offsets, the deepest interface arrives first. In the first-arrival-time curve labeled as "non-unique", at no offset does the refracted arrival from the first interface arrive first. Here, the first-arrival-time curve consists of only two straight-line segments and a one layer model can be constructed with this same two segment first-arrival-time curve.

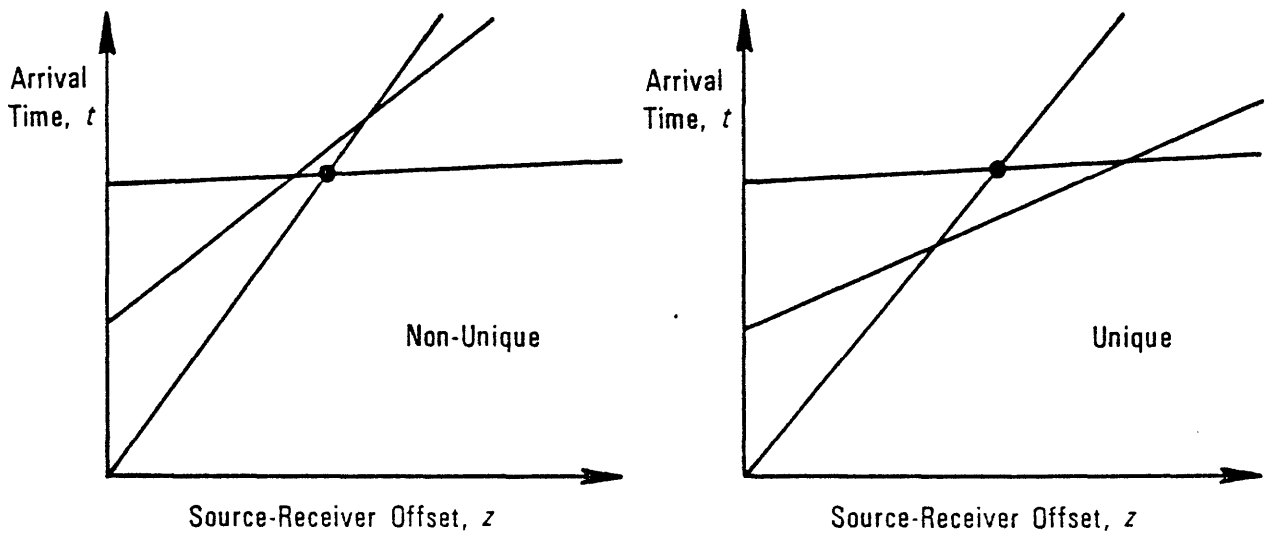

Figure 2-6. Non-uniqueness of first-arrival-time inversion

As a final note, in this cylindrically layered formation, the absolute depth of the source in the hole is irrelevant; only the offset of the receiver from the source is important. This is illustrated in Figure 2-7 where we show the first-arrival curves associated with different absolute depths in the hole. We see that data associated a given local experiment is ideally correlated with all other local experiments. This provides redundancy into the system which can be exploited to reduce the variance of the estimation error without sacrificing resolution. In effect, the travel-time curves in Figure 2-7 can be averaged together in the horizontal direction.

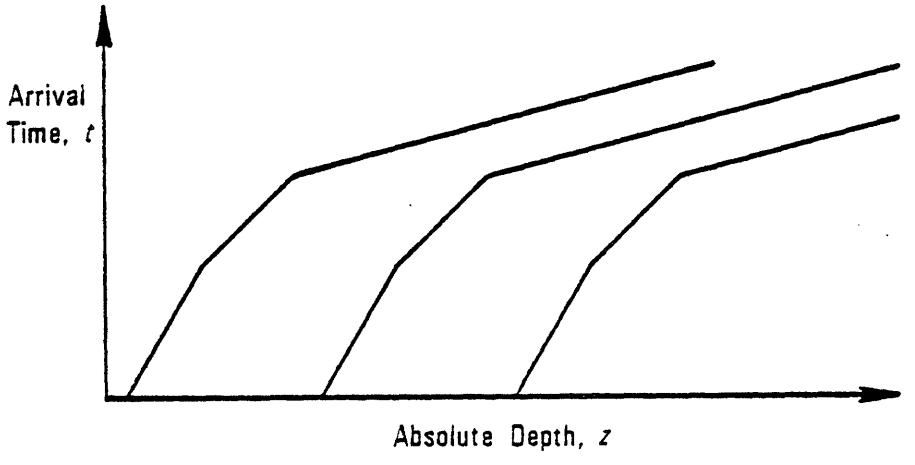

Figure 2-7. First-arrival-time curves associated with different source shots

b. A Bedded Formation Model

Now consider a formation model in which the only variation is in the axial direction. In Figure 2-8 we show an example of such a case where the axial variation is piecewise homogeneous. As before, if the bed thicknesses are small relative to a wavelength, the piecewise constant model will accurately approximate a continuously varying formation.

The axial propagation of headwaves through a system of layers is complicated due to the reflection and transmission of the waves at each layer. For this reason, we only discuss the first-

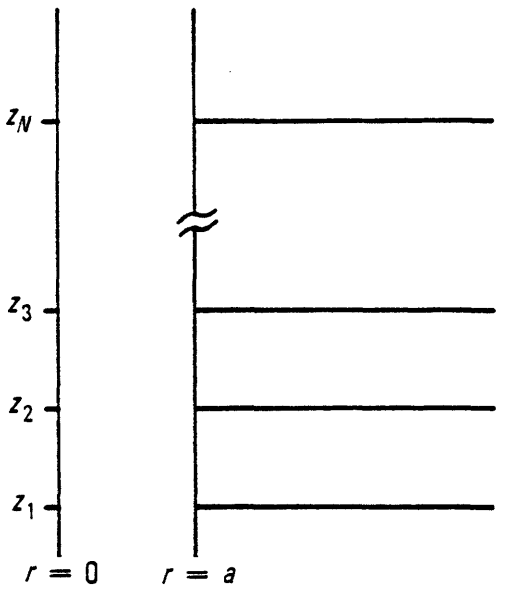

Figure 2-8. A bedded formation model

arrival-time of refracted energy from such a bedded system and ignore the multiple reflections and transmissions. Furthermore, a careful analysis of the first-arrival-time curve is complicated in the vicinity of the bed boundaries. For this reason, we only present an approximate analysis here.

In Figure 2-9 we show the approximate first-arrival-time curve for the system of beds shown in Figure 2-8. Again, the actual first-arrival-time curve differs slightly from this curve at the bed boundaries. It is clear from Figure 2-9 that the velocities and the layer depths and thicknesses can be obtained directly from the first-arrival curve.

Data associated with successive local experiments can be incorporated into the processing as shown in Figure 2-10. There, we show the first-arrival-time curves associated with different local experiments. It is clear from this figure that, in estimating the velocity in a particular layer, one should effectively average the first-arrival-time curves in the vertical direction. In addition, the averaging process will reduce the estimation variance without sacrificing axial resolution. This vertical averaging is contrasted to the case of cylindrical layers in which we averaged horizontally.

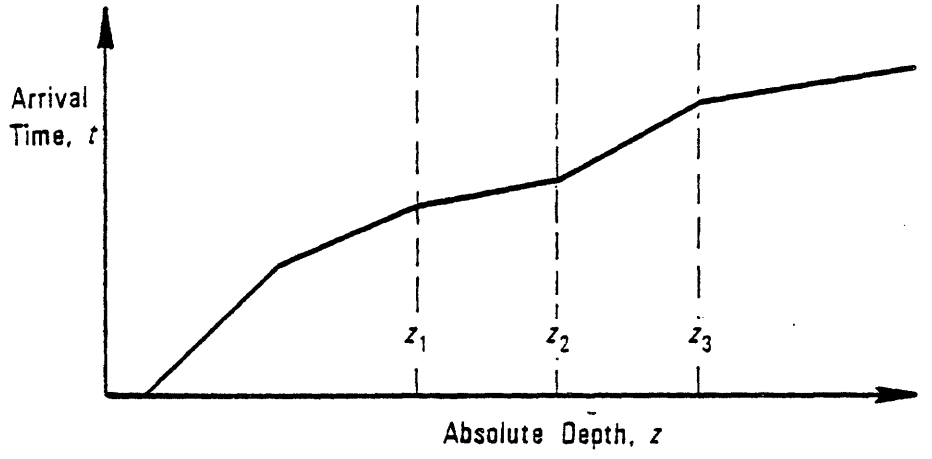

Figure 2-9. An approximate first-arrival-time curve for a bedded formation model

c. A Heterogeneous Formation Model

Finally, consider a formation model which varies in both r and z, but not in θ. In Figure 2-11 we show first-arrival-time curves for such a formation model for successive local experiments. Intuitively, we expect that, if there is no radial variation in the formation, then Figure 2-11 will look like Figure 2-10. That is, the slope of each first-arrival-time curve will be the same at each depth. On the other hand, if the formation contains radial variation, but no axial variation, then Figure 2-11 will look like Figure 2-7. That is, the curves in Figure 2-11 will all be the same shape but will be translated horizontally with respect to each other. Deviations from these conditions, then, indicate the presence of both radial structure and horizontal bedding.

The interesting theoretical issue in this more complicated formation model is how to interpret, or invert, the first-arrival-time curves in the presence of both radial and axial variation. First-arrival-time information by itself will not be sufficient to image the formation everywhere. However, the derivative of the first-arrival-time curve associated with a particular source shot

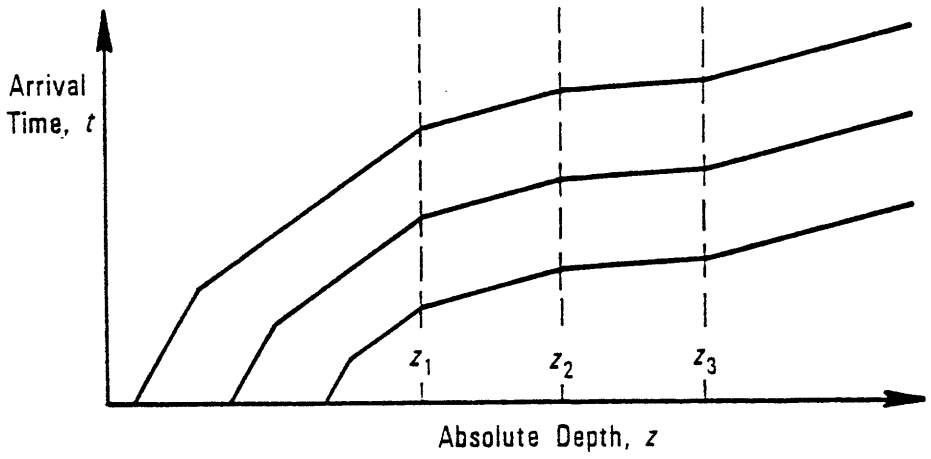

Figure 2-10. First-arrival-time curves for successive source shots

and evaluated at a particular absolute depth corresponds to a velocity in the formation somewhere. The inversion problem, then, is to identify this spatial point. This is illustrated in Figure 2-12. Viewed in this light, the travel-time inversion problem is one of positioning, or *migrating*, the velocities observed on the borehole axis to their proper positions in space.

d. Conclusions

The conventional refraction-based approach to processing acoustic logging data can be viewed as a restricted case of travel-time inversion in which the formation is modeled as homogeneous and the correlation between successive local experiments is not exploited. With this viewpoint, the arrival-time curves across the array aperture are approximated by straight lines and variation with depth is resolved if the straight line estimates from successive local experiments changes. If the array is many wavelengths long, and if it shifts only a fraction of its aperture between successive source shots, then this approach will produce stable estimates at the expense of axial resolution. Furthermore, if the formation variation in r is insignificant, then from our analysis earlier, higher resolution estimates can be obtained with no loss in stability by averaging the arrival-time curves vertically thereby exploiting the correlation between successive

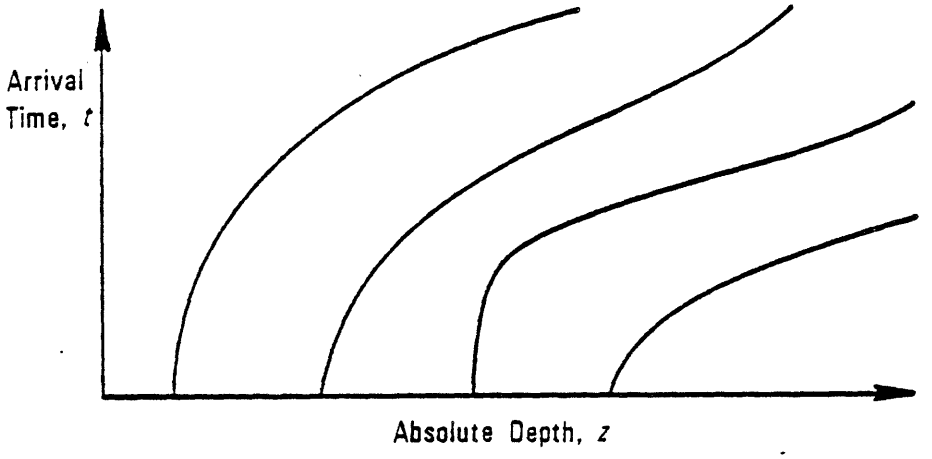

Figure 2-11. First-arrival-time curves for a heterogeneous formation model

source shots.

A subset of the travel-time inversion problem is the first-arrival-time inversion problem. Here, there is an issue of uniqueness as we saw in the case where the formation model varied radially, but not axially. Of fundamental concern then is the characterization of the set of formation models consistent with the first-arrival-time information and the identification of any additional restrictions which can be imposed to make the inversion problem unique.

The extension of the refraction-based method to an axially and radially heterogeneous formation model represents an area for future theoretical research. In general, the problem can be thought of as one of migrating the velocities measured on the borehole axis into their proper spatial positions. If successful, such a method would produce a 2D image of the velocity structure of the formation.

2.4.3 Refraction Tomography

The problem addressed in tomography is the reconstruction of an object from a set of its projections (i.e. line integrals of its properties). In general, the more projections, or views, of

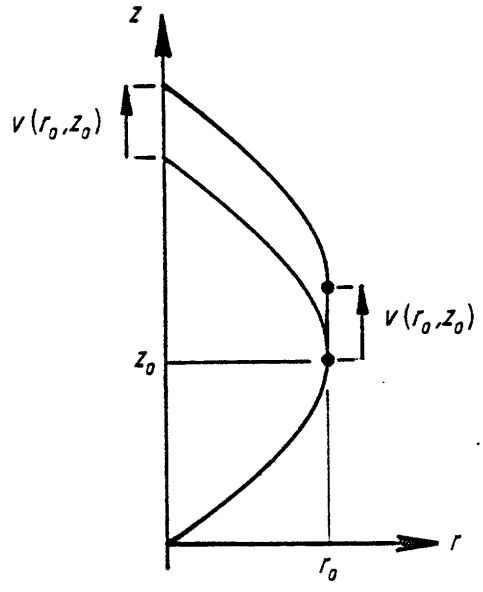

Figure 2-12. A migration interpretation of travel-time inversion

the object that one has, the better the reconstruction, or image.

The time at which a particular refraction arrives is equal to an integral of the slowness (i.e. inverse velocity) of the velocity structure along the ray path which the energy followed. In this sense, the arrival time is a projection of the formation slowness structure. A collection of source-receiver pairs results in travel-time information from one depth to another, denoted $t(z_1,z_2)$. From projections of this type, one can consider reconstructing the velocity structure of the formation.

The primary complication with the application of tomographic concepts to the refraction geometry is the fact that the ray paths are unknown. However, the ray paths are not random, but depend upon the velocity structure itself. Given the velocity structure, one can solve for the ray paths, and conversely, given the ray paths, one can solve for the velocity structure. This observation suggests that an iterative processing approach might be appropriate. In such an approach, one might assume that the ray paths are known and then reconstruct the velocity structure. Following this, the ray paths can be recomputed, which will then lead to a new velocity structure. The process will repeat in this manner until convergence is achieved.

All the rays which pass through a given depth interval should be used in reconstructing the velocity structure in that region. Ray paths which pass through the region currently being reconstructed and into a region not yet reconstructed will not be useful. Thus, one can imagine that the formation velocity structure has been reconstructed from the bottom of the hole up to some point and the problem is to extend the reconstruction upwards by some amount. Rays starting in the region already reconstructed but ending in the interval currently being reconstructed will be used in the current reconstruction. The reconstruction process can then proceed in small steps from the bottom of the hole upwards.

2.5 The Proposed Reflection-Based Method

A distinctly different approach to acoustic well logging, and the approach investigated in this thesis, is based on a principle of reflection, rather than refraction. In such an approach, a receiver array is placed in close proximity to the source so that the primary, or spectral, reflection off the formation wall will be received. The processing will then analyze the measured reflection in order to learn about the formation.

The major complications encountered in a reflection measurement are the presence of multiple reflections and the presence of a large direct arrival from the source. These additional arrivals at the receiver array disturb the measurement of the primary reflection and must be compensated for in some manner. Following this is the issue of interpreting the primary reflection in terms of the formation parameters of interest.

From Chapter I we saw that the primary reflection can be parameterized using the concept of the cylindrical wave reflection coefficient. This concept will be fully developed in the next chapter. In this section, we present the theoretical cylindrical wave reflection coefficient associated with a homogeneous formation model and discuss its interpretation in terms of the parameters of the formation. Radially varying formation models are not discussed here. In the remaining chapters, we treat the estimation of the reflection coefficient from the sum of all the reflected arrivals, but with no direct arrival. The issue of the direct arrival from the source is not

considered here.

We begin this section with a space-time domain interpretation to the reflection coefficient and follow this with some insights into the frequency-wavenumber domain. In particular, we will emphasize the sensitivity of the reflection coefficient to the formation sound speeds, attenuations and density.

2.5.1 A Space-Time Domain Interpretation

We denote the cylindrical wave reflection coefficient as $R(k_z,\omega)$ and its 2D Fourier transform by $r(z,t)$. Specifically,

$$r(z,t) = \frac{1}{(2\pi)^2} \int_{-\infty}^{\infty} \int_{-\infty}^{\infty} R(k_z,\omega)\, e^{-i\omega t}\, e^{ik_z z}\, dk_z\, d\omega \tag{2.6}$$

We refer to $r(z,t)$ as the reflection coefficient signal.

In Figure 2-13 we show 3 waveforms representing the reflection coefficient signal convolved with the Hilbert transform of the source pulse (i.e. $s_h(t) * r(z,t)$) for three different offsets from the source. The formation model associated with these signals is perfectly elastic and homogeneous. The method used to generate these waveforms is discussed in Chapter IV. In this figure, one can see that the primary reflection off the formation takes the form of a single wavelet at short offsets from the source but spreads into three distinct wavelets with increasing offset. The first wavelet to arrive is the first compressional headwave and the second is the first shear headwave. The third wavelet is actually the sum of two arrivals traveling at roughly the same speed so that they are difficult to resolve. One of the components of the third wavelet is a reflection off the formation wall while the other is a surface wave attached to the fluid/solid interface. The surface wave propagates slightly slower than the reflected wave, which travels at the fluid speed, and is closely related to the Stoneley, or tube, wave present in the full acoustic signals [33].

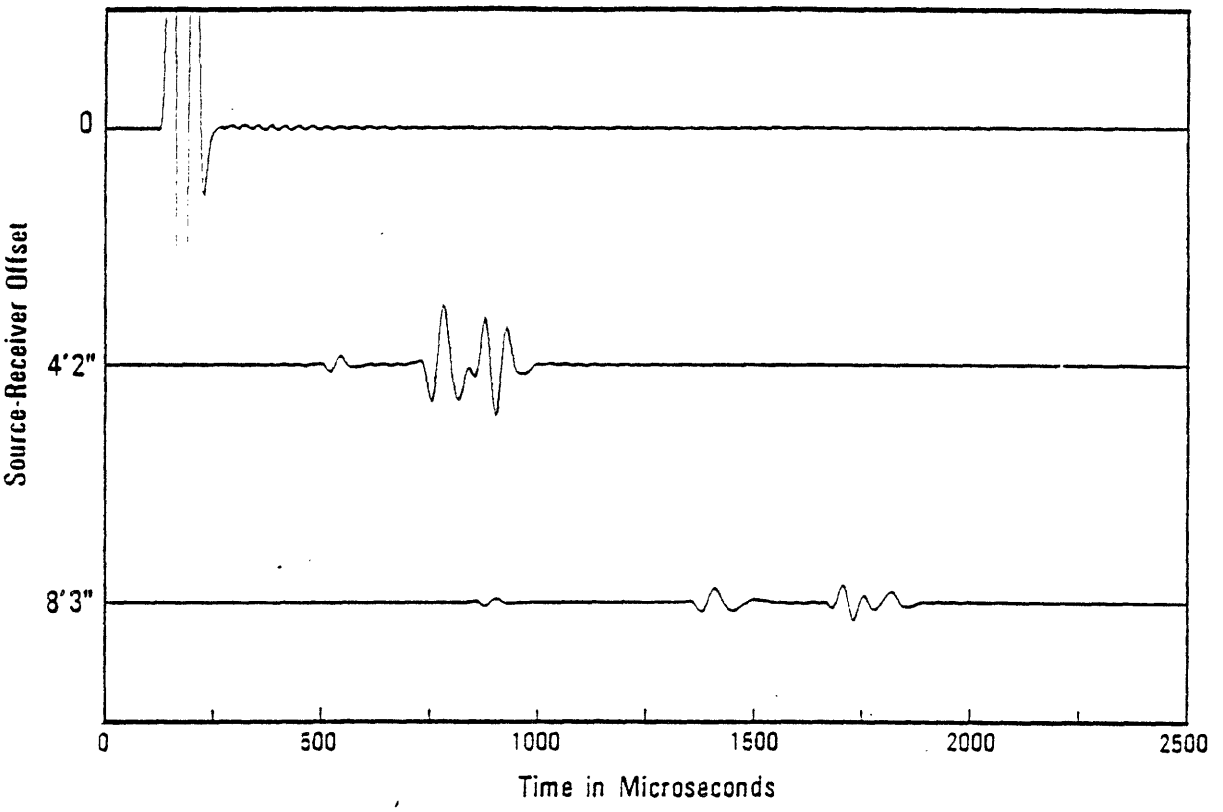

Figure 2-13. The primary reflection at three source-receiver offsets

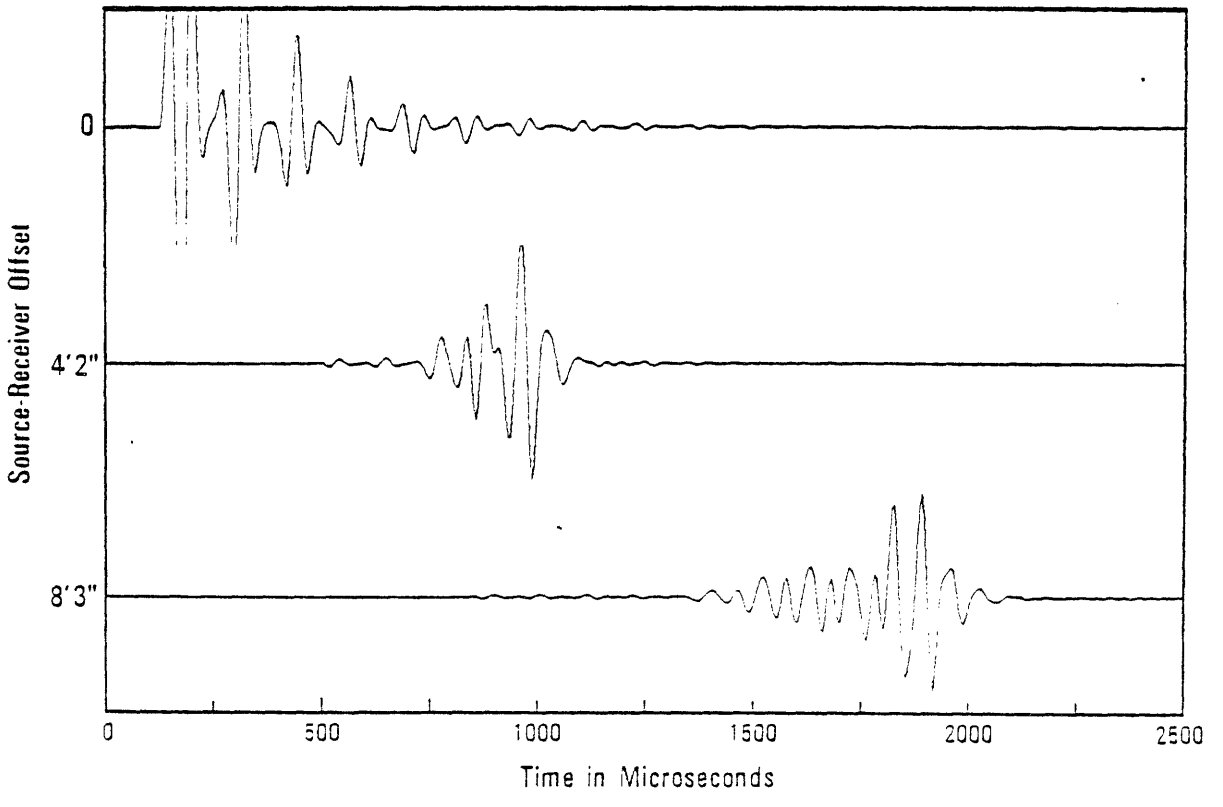

Figure 2-14. The reflected component of the total field at three source-receiver offsets

In Figure 2-14 we show three waveforms representing the reflected component of the total field for the same three offsets shown in Figure 2-13. The amplitude scale in Figure 2-14 has been scaled down by a factor of 2 relative to Figure 2-13. Physically, the reflected component of the total field corresponds to the sum of the primary reflection and all the multiple reflections. The total pressure field on the axis of the borehole is obtained by adding the direct arrival from the source to each of these signals.

Note that the first compressional and shear headwaves can be identified in 2-14 by comparing the waveforms with those in Figure 2-13. Furthermore, note in 2-14 that these first headwaves are followed by a series of multiple headwaves not present in the reflection coefficient signals. In addition, following the first shear headwave in 2-14, the waveforms become more difficult to interpret. In the first waveform (corresponding to zero offset from the source) the individual reflections of the source pulse can be resolved. Note that each successive reflection has a distinct change in shape. Furthermore, every fourth reflection has roughly the same shape. This is due to the fact that each successive reflection is roughly the Hilbert transform of the previous reflection [31]. In the second waveform (a 4'1" offset), we begin to see modal phenomena following the first shear headwave, while in the third waveform (a 8'3" offset) the modal phenomena more evident. The large feature in this waveform is the Stoneley, or tube, wave.

From this comparison of Figures 2-13 and 2-14, we conclude that 2-14 is dominated at large offsets by the interference effects of the multiple reflections (i.e. the modes), while 2-13 is not. Rather, the reflection coefficient signals clearly delineate the headwave arrivals. The fact that these arrivals are well separated is useful since these wavelets travel a path within the formation itself and will be sensitive to the formation parameters. At the very least, the arrival times of these wavelets can be used to infer the compressional and shear sound speeds in the formation. The signals in Figure 2-14 contain significant energy which has traveled a path within the fluid column and this energy is not as formation dependent as the first headwaves.

In Figure 2-15 we show a 100 receiver array of synthetic reflection coefficient signals from

which the first, middle and last signals were plotted in Figure 2-13. This array is plotted in a variable density log (VDL) format where the grey-scale indicates amplitude. In Figure 2-16 we show the corresponding 100 receiver array of theoretical reflected field waveforms. The transition from individual reflections at short offsets to modal phenomena at large offsets can be seen in Figure 2-16. This behavior is absent in Figure 2-15 because there is no multiply reflected energy. Furthermore, the compressional and shear velocities are easier to identify in 2-15 than 2-16.

2.5.2 A Frequency-Wavenumber Domain Interpretation

In Figure 2-17 we show a perspective plot and a contour plot of the magnitude of the cylindrical wave reflection coefficient as a function of frequency and wavenumber. Note the clear delineation of the compressional, shear and fluid speeds in the problem and in addition, note the sharp thin ridge at a slope corresponding to a speed just slower than the fluid speed. This is a Stoneley wave feature and is responsible for exciting the surface wave discussed earlier.

In the first signal in Figure 2-18, we show a slice of the reflection coefficient shown in Figure 2-17 and made at a constant value of axial wavenumber. This slice contains all the features of the 2D reflection coefficient and we discuss its interpretation here.

Starting at high frequencies, note that the reflection coefficient magnitude approaches a constant final value. This value is given by the plane wave reflection coefficient at normal incidence for the analogous problem of a liquid/solid interface in a planar geometry. Specifically,

$$\lim_{\omega \to \infty} |R(k_z, \omega)| = \frac{\rho_1 v_c - \rho v_f}{\rho_1 v_c + \rho v_f} \tag{2.7}$$

where ρ denotes the density in the fluid (i.e. mud), ρ_1 denotes the density in the formation and v_c and v_f are the compressional speed in the formation and the compressional speed in the fluid respectively. We conclude that the high frequency limit of the reflection coefficient is sensitive to the densities and velocities of the media.

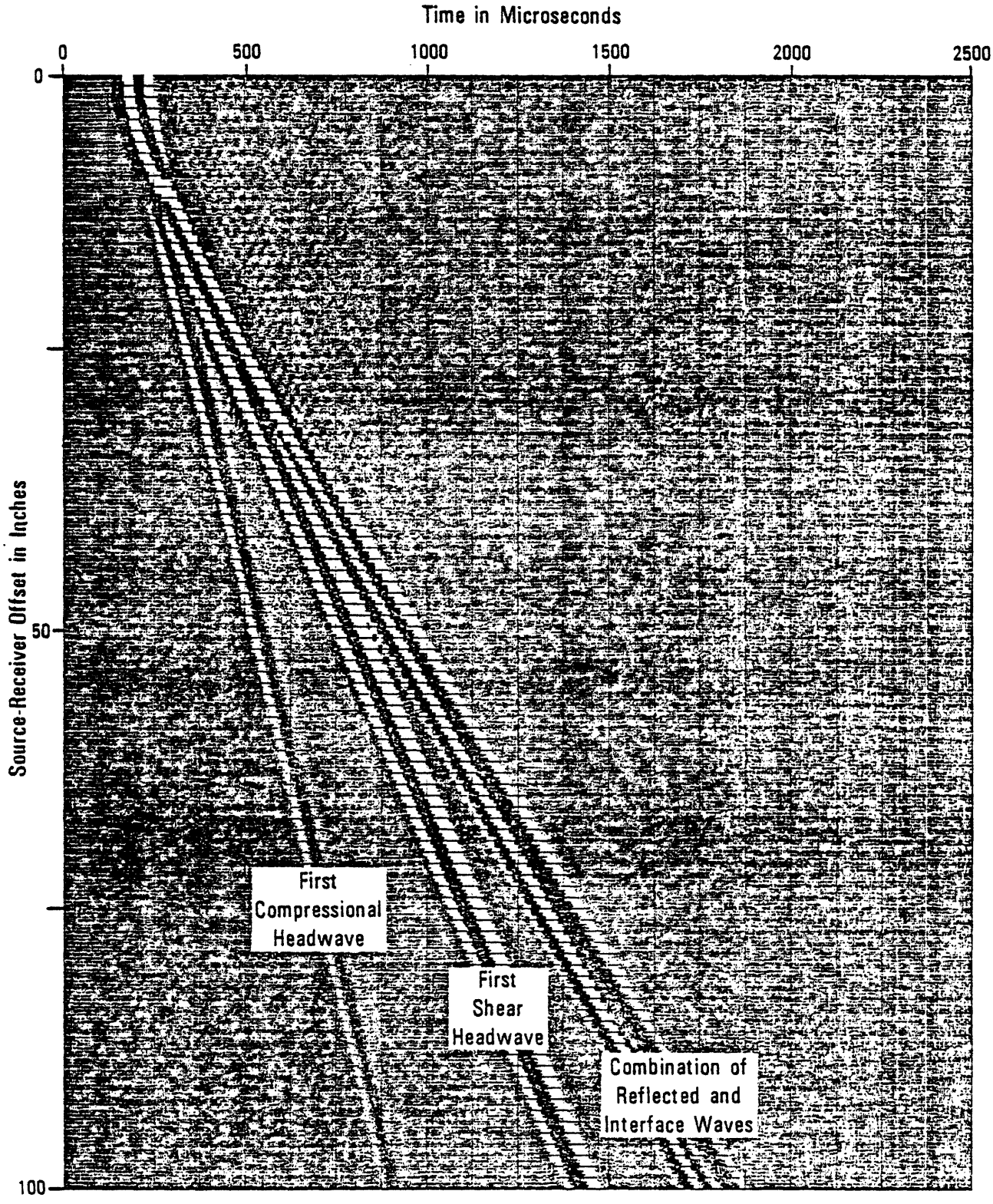

Figure 2-15. A VDL of the primary reflection

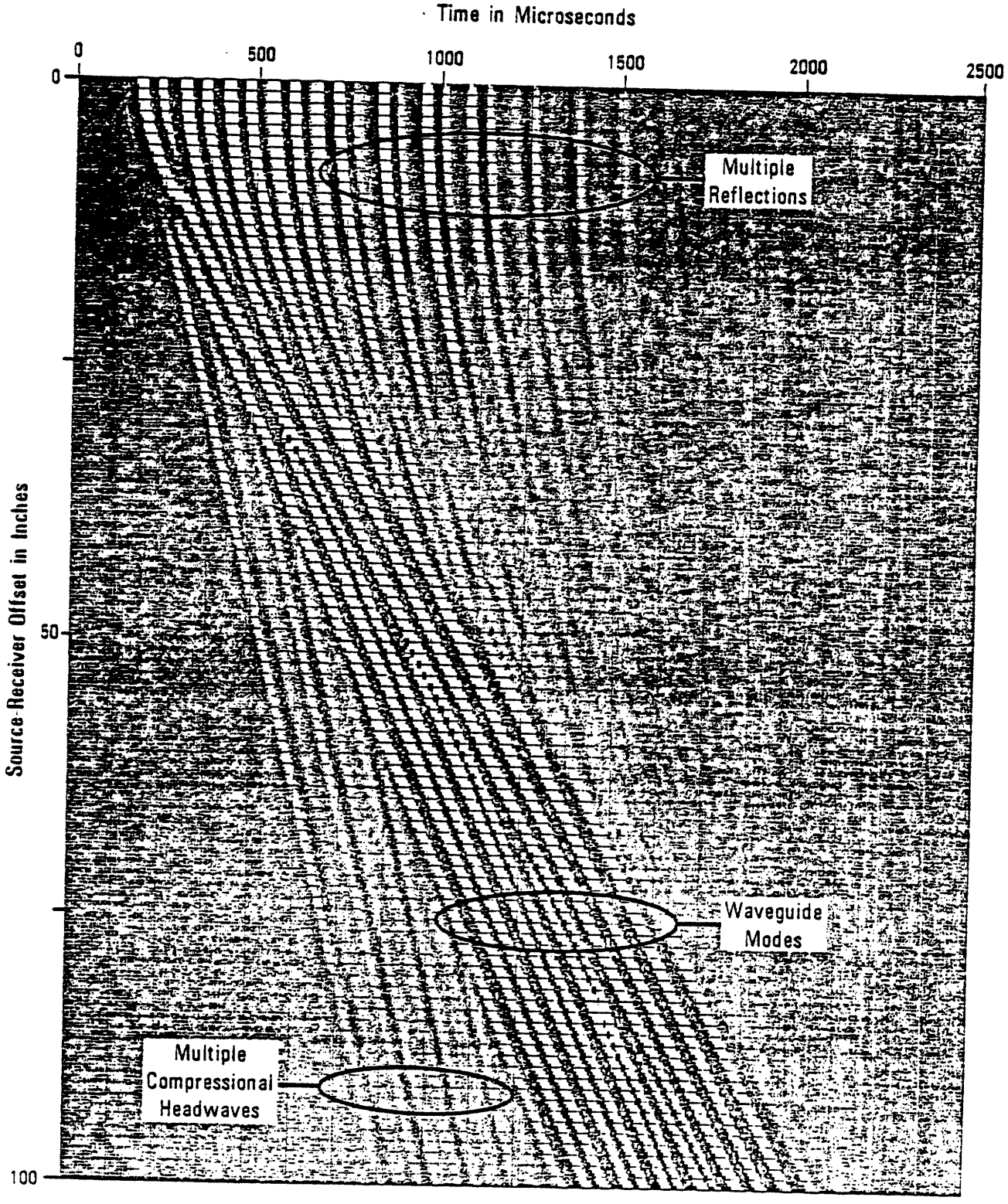

Figure 2-16. A VDL of the reflected component of the total field

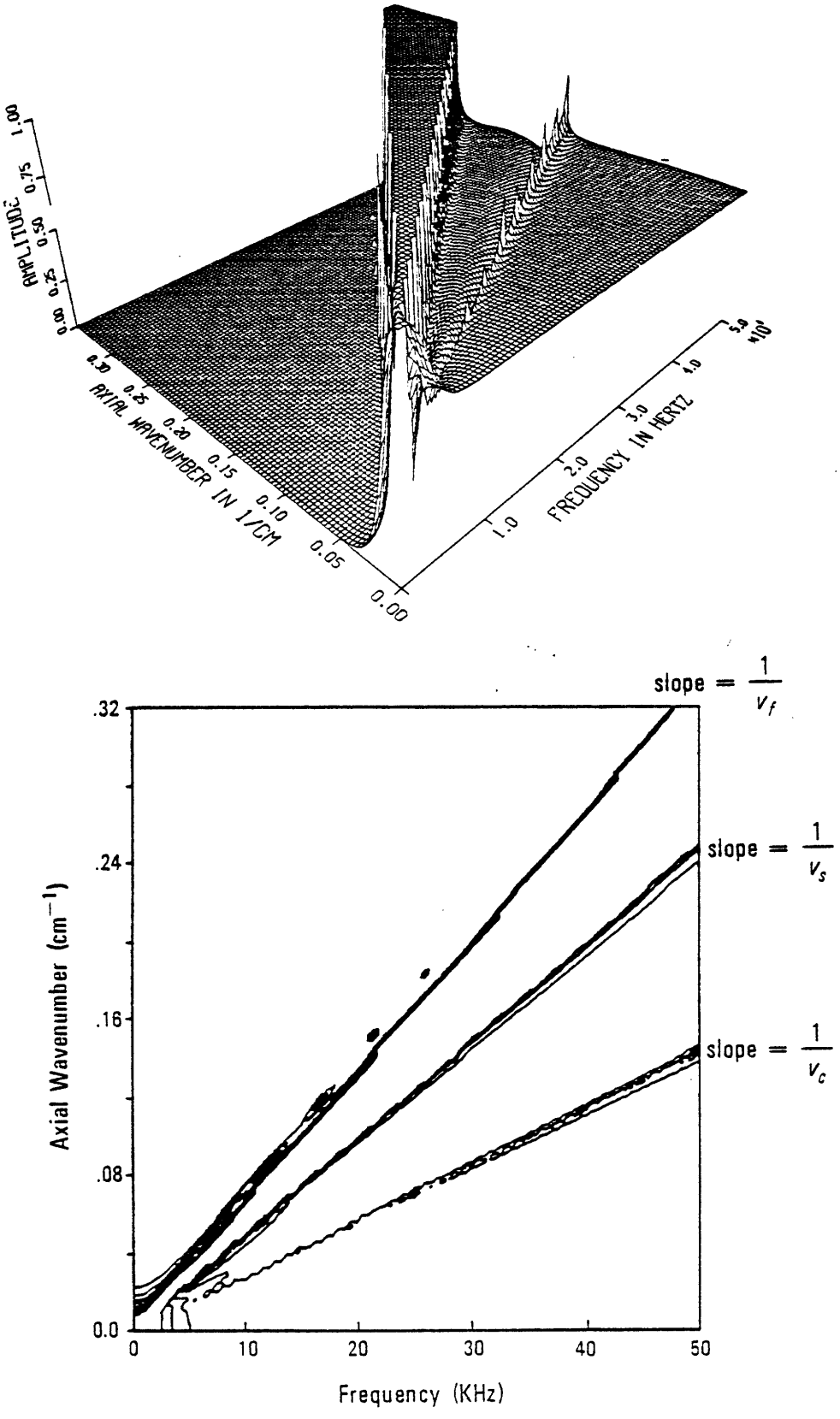

Figure 2-17. The magnitude of the reflection coefficient

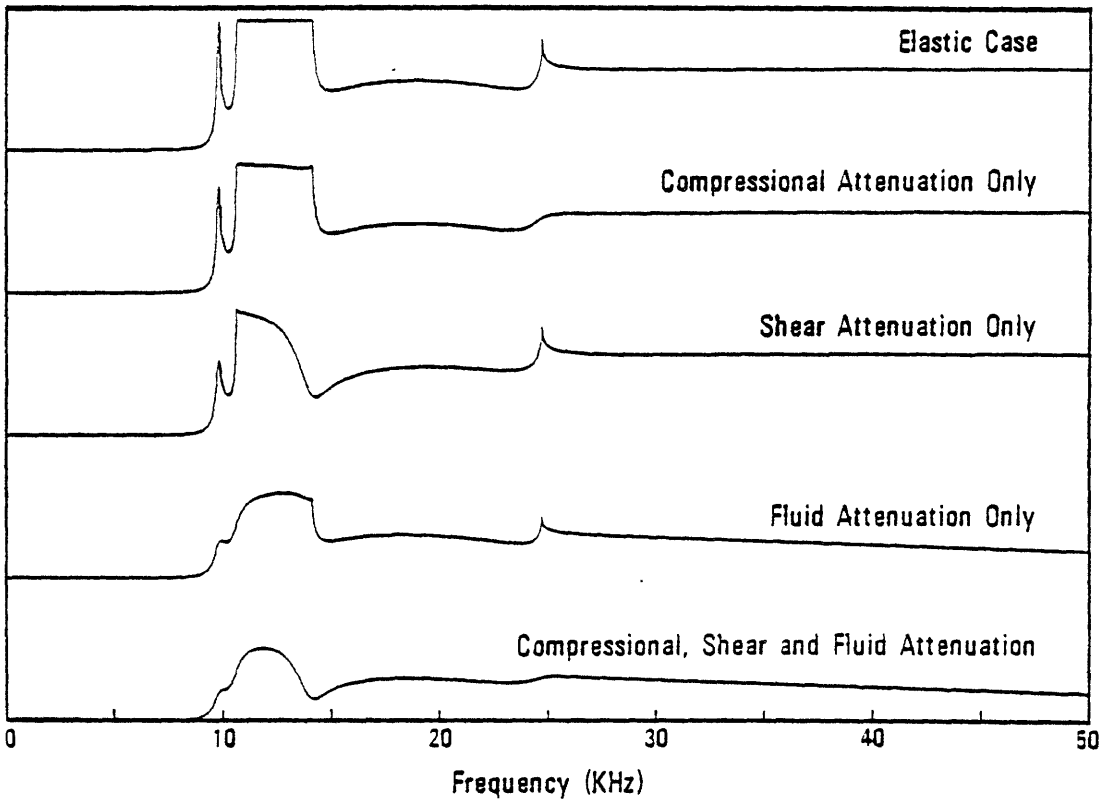

Figure 2-18. A slice of the reflection coefficient and sensitivity to attenuation

Moving down in frequency, the sharp peak at 25 KHz corresponds to the excitation of the compressional headwave. The frequency and wavenumber associated with this feature correspond to an incidence angle equal to the compressional critical angle. At this angle, there is no transmitted shear wave into the formation and the transmitted compressional wave is critically refracted. If the reflection coefficient were sampled more finely in this figure, we would see it jump up to unity magnitude at this point. These same comments apply to the perspective plot in Figure 2-17.

Between 11 and 14 KHz, the reflection coefficient is seen to have a magnitude of unity. On either side of this region, the reflection coefficient drops off sharply, giving the image of a table top. For this reason, we will frequently refer to this as the table region of the reflection

coefficient. Incident cylindrical waves having frequencies and wavenumbers in this region are totally internally reflected and do not transmit propagating waves into the formation. The right edge of the table, at 14 KHz, corresponds to incidence at the shear critical angle. At this frequency and wavenumber, the transmitted shear wave becomes critically refracted. The left edge of the table, at 11 KHz, corresponds to grazing incidence. At this point, the axial component of wavenumber is equal to the total wavenumber so that there is no radial component. At frequencies below 11 KHz, the radial component of wavenumber becomes imaginary, indicating that there will be exponential attenuation in the radial propagation out to the formation wall and back. For this reason, the reflection coefficient drops off exponentially. The exception to this rule is the sharp peak occuring at roughly 10 KHz. This peak corresponds to the excitation of an interface wave closely related to the Stoneley, or tube, wave which is prominent in full acoustic waveforms. Note that this wave is excited by an inhomogeneous incident cylindrical wave (i.e. the axial component of wavenumber is larger than the total wavenumber) and that the reflection coefficient has unity magnitude at this point. This is unlike the analogous situation in a planar geometry where the plane wave reflection coefficient is infinite at the wavenumber associated with a surface wave [15].

In the remaining four signals in Figure 2-18 we show the effects of introducing attenuation into the formation model and into the borehole fluid medium. There are three sound speeds in this model, v_c, v_s and v_f, and we model attenuation by adding a small negative imaginary component to each speed [2]. In the second signal in the figure, we have added an imaginary component of compressional speed equal to 1/40 of the real-part while keeping the other two speeds real-valued. Note that the dominant effect of introducing only compressional attenuation is to smear out the compressional feature at 25 KHz. Similarly, in the third figure, we introduce only shear attenuation and again make the imaginary part 1/40 of the real-part. Here, we see that the compressional feature returns, but the right edge of the table region is rounded off. This is expected since this area is associated with the shear critical angle. The fourth signal corresponds to introducing the same amount of attenuation into the fluid medium, but none in the formation. Note that this rounds off the left side of table region, as expected, but also

reduces the amplitude at all frequencies. This is because, at all frequencies, the wave must propagate from the axis to the formation and back within the fluid. The final signal in Figure 2-18 shows the effect of adding imaginary velocity components of 1/40 of the real-parts to all three velocities. Comparing the elastic case to this case, we see that they are significantly different.

We conclude that the reflection coefficient has features which are sensitive to the formation density, velocities and attenuations. Furthermore, these parameters affect the reflection coefficient in an manner which is interpretable.

As a final note, in Figure 2-19 we show contour and perspective plots of the sum of all the reflections in the frequency-wavenumber domain (i.e. the reflected component of the field). Here we see that the speeds in the geometry still delineate the features in this figure, but not as clearly as in Figure 2-17. For example, between the shear and fluid lines, corresponding to the table region in the reflection coefficient, the figure is dominated by mountain-range behavior. These ranges and valleys correspond to the interference of the multiple reflections. Because the reflection coefficient has unity magnitude in this region, when constructive interference occurs infinitely high peaks can occur. Outside of this wedge-shaped region, the reflection coefficient is less than unity in magnitude and, although constructive and destructive interference occurs, the waves lose energy to the formation and do not propagate as far. The ridges in this region are smaller and these waves are referred to as leaky modes since they continually leak energy into the formation as they propagate.

2.5.3 Conclusions

We conclude that the reflected component of the field is dominated by interference phenomena while the reflection coefficient is dominated by the formation parameters of interest. For this reason, we examine the estimation of the reflection coefficient from measurements of the reflected component of the field in the remainder of this thesis.

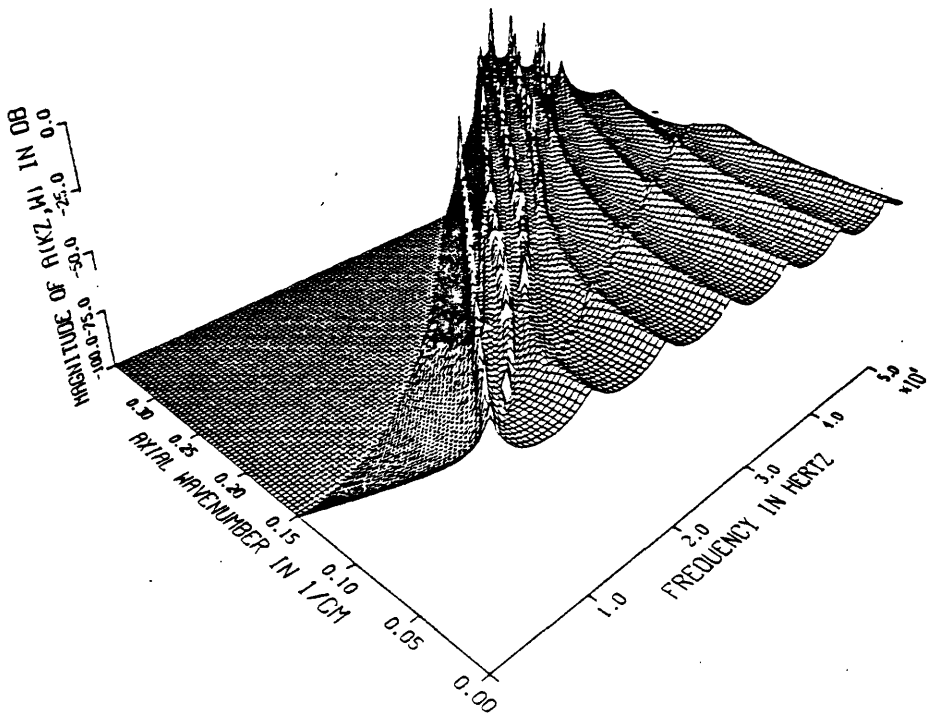

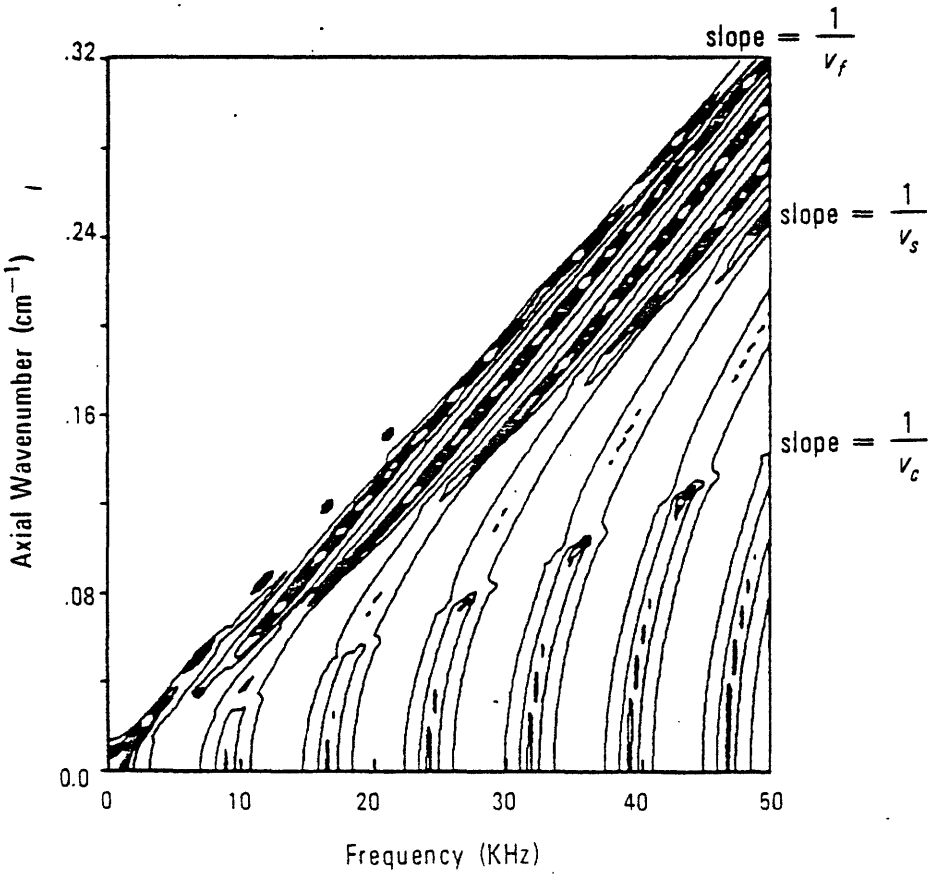

Figure 2-19. The magnitude of the sum of all the reflections

III. BOREHOLE ACOUSTICS

3.1 Introduction

In order to estimate the cylindrical wave reflection coefficient from measurements of the reflected component of the pressure field in the borehole, some relationship between the two must first be established. In this chapter we explore the propagation of acoustic waves in cylindrical axi-symmetric geometries to derive such a relationship. In Chapter V, this relation will serve as the basis for the development of several signal processing models, one of which will be examined in detail in Chapter VI. In addition, a modal representation of the field is developed in this chapter which will serve in Chapter IV as the basis for the numerical evaluation of synthetic acoustic fields. In this chapter, then, we build the foundation upon which the remainder of this thesis rests.

We begin this chapter with a study of the properties of monochromatic cylindrical waves in an infinite homogeneous fluid medium. We then place a point source in the medium and discuss the representation of the field due to the source as a weighted integral of cylindrical waves. Following this, we introduce cylindrical stratification into the geometry and place the point source, or an array of point sources, on the axis. We then develop the concept of the cylindrical wave reflection coefficient and examine its properties. Finally, we derive an expression for the field in terms of the cylindrical wave reflection coefficient. This expression is valid in a homogeneous cylindrical region around the axis which has a radius just large enough to include the farthest receiver from the axis. In this way, all the receivers are in a homogeneous fluid medium. The geometry under consideration, then, is shown in Figure 3-1.

3.2 Monochromatic Cylindrical Waves

Consider a cylindrical axi-symmetric coordinate system set in an infinite source-free, homogeneous fluid medium with sound speed v_f. Assuming $e^{\pm i\omega t}$ time dependence, the

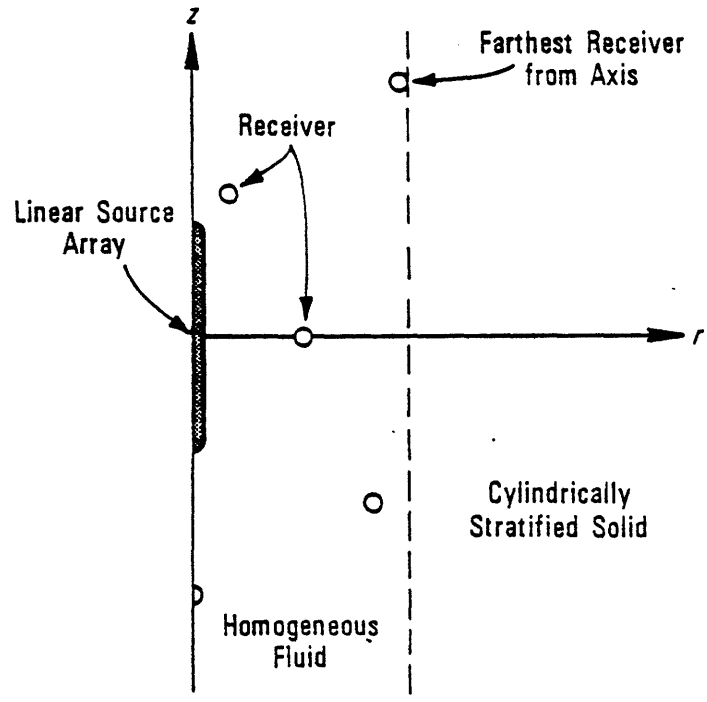

Figure 3-1. The geometry under consideration.

homogeneous scalar wave equation for such a situation is given by

$$(\nabla^2 + k^2) \, p(z,r) = 0 \tag{3.1}$$

where k is the total wavenumber, given by $k=\omega/v_f$, and

$$\nabla^2 = \frac{\partial^2}{\partial r^2} + \frac{1}{r}\frac{\partial}{\partial r} + \frac{\partial^2}{\partial z^2} \tag{3.2}$$

Here, $p(z,r)$ denotes the monochromatic acoustic pressure field in the medium. Any monochromatic pressure field in a source-free region of the medium must satisfy this equation.

Solutions to equation (3.1), with the time dependence explicitly included, are of the form

$$H_0^{(r)}(k_r r)\, e^{\pm i k_z z}\, e^{\pm i\omega t} \tag{3.3}$$

or any linear combination (i.e. weighted integral) of terms of this form. Here, k_r and k_z denote

the radial and axial components of wavenumber (i.e. $k^2 = k_r^2 + k_z^2$) and $H_o^{(\nu)}$ denotes a Hankel function of order 0 and type ν, where $\nu = 1$ or 2. Hankel functions will appear regularly throughout this chapter and in Table 3-1 we have listed their most fundamental properties [1]. The relations in this table will be referred to frequently.

The waves represented in equation (3.3) are termed monochromatic cylindrical waves and are analogous to the monochromatic plane wave solutions in Cartesian coordinates. However, the analogy is not complete. While a plane wave is so called because its wavefront is planar, a cylindrical wave does not have a cylindrical wavefront. In this sense, the terminology "cylindrical wave" is a misnomer.

The interpretation of the waves in equation (3.3) depends upon the choice of the Hankel function type and the signs on the exponentials. In this thesis, we select the customary $e^{-i\omega t}$ time dependence and, corresponding with this choice, we choose $e^{+ik_z z}$ dependence on z. In this way, for positive values of ω and k_z, waves of the form $e^{-i(\omega t - k_z z)}$ propagate axially upward as time increases. Also associated with this choice of time dependence, the $H_o^{(1)}$ Hankel function has the interpretation of a wave which is propagating radially outward. This interpretation is particularly evident when the magnitude of $k_r r$ is large and we approximate $H_o^{(1)}$ with its large argument limiting form (Table 3-1). Similarly, $H_o^{(2)}$ is interpreted as a wave which is traveling radially inward.

It is convenient to think of k_z, ω and v_f as independent quantities in the description of a monochromatic cylindrical wave and to think of the radial component of wavenumber, k_r, as a dependent variable. Specifically, the radial wavenumber is given in terms of the independent variables by

$$k_r = \sqrt{k^2 - k_z^2} \tag{3.4}$$

where, as always, $k = \omega / v_f$. The sign of the square root in (3.4) must be chosen such that $\arg(k_r)$ is greater than or equal to zero but less than π in order that outward propagating waves

TABLE 3-1. HANKEL FUNCTION RELATIONS

Large Argument Limiting Forms

$$H_o^{(1)}(z) \sim \left[\frac{2}{\pi z}\right]^{\frac{1}{2}} e^{i(z-\pi/4)} \qquad H_o^{(2)}(z) \sim \left[\frac{2}{\pi z}\right]^{\frac{1}{2}} e^{-i(z-\pi/4)}$$

$$H_1^{(1)}(z) \sim \left[\frac{2}{\pi z}\right]^{\frac{1}{2}} e^{i(z-3\pi/4)} \qquad H_1^{(2)}(z) \sim \left[\frac{2}{\pi z}\right]^{\frac{1}{2}} e^{-i(z-3\pi/4)}$$

Small Argument Limiting Forms

$$H_o^{(1)}(z) \sim \frac{2i}{\pi}\ln(z) \qquad H_o^{(2)}(z) \sim -\frac{2i}{\pi}\ln(z) \qquad H_1^{(1)}(z) \sim -\frac{2i}{\pi}\frac{1}{z} \qquad H_1^{(2)}(z) \sim \frac{2i}{\pi}\frac{1}{z}$$

Analytic Continuation

$$H_o^{(1)}(-z^*) = -H_o^{(1)*}(z) \qquad H_o^{(2)}(-z^*) = H_o^{(2)*}(z) + 2H_o^{(1)*}(z)$$

$$H_1^{(1)}(-z^*) = H_1^{(1)*}(z) \qquad H_1^{(2)}(-z^*) = -H_1^{(2)*}(z) - 2H_1^{(1)*}(z)$$

Relationship to Bessel Functions

$$H_o^{(1)} = J_o + iY_o \qquad H_0^{(2)} = J_o - iY_o \qquad H_1^{(1)} = J_1 + iY_1 \qquad H_1^{(2)} = J_1 - iY_1$$

$$J_o = \frac{1}{2}\left[H_o^{(1)} + H_o^{(2)}\right] \qquad Y_o = \frac{1}{2i}\left[H_o^{(1)} - H_o^{(2)}\right] \qquad J_1 = \frac{1}{2}\left[H_1^{(1)} + H_1^{(2)}\right] \qquad Y_1 = \frac{1}{2i}\left[H_1^{(1)} - H_1^{(2)}\right]$$

Wronskian Relations

$$H_1^{(1)}(z)\,H_o^{(2)}(z) - H_o^{(1)}(z)\,H_1^{(2)}(z) = -\frac{4i}{\pi z} \qquad J_1(z)\,Y_o(z) - J_o(z)\,Y_1(z) = \frac{2}{\pi z}$$

Derivatives (ν=1 or 2)

$$\frac{d}{dz}H_o^{(r)}(z) = -H_1^{(r)}(z) \qquad \frac{d}{dz}H_1^{(r)}(z) = \frac{1}{z}H_1^{(r)}(z) - H_o^{(r)}(z)$$

do not grow with r. The inward propagating cylindrical waves, $H_n^{(2)}$, do grow with increasing r for this choice of sign on k_r. However, this is not a problem since there are no waves of this form propagating in from $r = \infty$.

In this chapter, ω, k_z and v_f will be taken to be real-valued quantities. While the sound speed is a positive quantity, the axial component of wavenumber and frequency can each be positive or negative. Under these assumptions, the radial component of wavenumber is seen from (3.4) to be either purely real or positive imaginary, depending upon whether k^2 is greater than k_z^2 or not. If k_r is real-valued, we say that the wave is propagating (or homogeneous), while if k_r is positive imaginary, the wave is non-propagating (or inhomogeneous, or evanescent).

3.2.1 The Impedance of a Cylindrical Wave

The radial component of acoustic impedance, z_r, is given by the ratio of pressure to the radial component of the velocity field [6]. That is,

$$z_r = \frac{p}{v_r} \tag{3.5}$$

The pressure and radial velocity are each related to the displacement potential of the acoustic field, ϕ, by the relations [14]

$$p = \omega^2 \rho \phi \qquad v_r = -i\omega \frac{\partial \phi}{\partial r} \tag{3.6}$$

where ρ denotes the density of the medium. Substituting (3.6) into (3.5) gives the impedance in terms of the displacement potential as

$$z_r = i\omega\rho\,\phi \left[\frac{\partial \phi}{\partial r} \right]^{-1} \tag{3.7}$$

We now identify the form of z_r for the case where the displacement potential is in the

form of a monochromatic cylindrical wave. Specifically, for an outgoing cylindrical wave of the form $\phi = H_0^{(1)}(k_r r)$, equation (3.7) becomes

$$z^{out} = -j \frac{\omega\rho}{k_r} \frac{H_0^{(1)}(k_r r)}{H_1^{(1)}(k_r r)} \tag{3.8}$$

while for an incoming wave of the form $\phi = H_0^{(2)}(k_r r)$, we find that

$$z^{in} = -j \frac{\omega\rho}{k_r} \frac{H_0^{(2)}(k_r r)}{H_1^{(2)}(k_r r)} \tag{3.9}$$

In the limit as $k_r r \to \infty$, using the large argument limiting forms given in Table 3-1, we find that the cylindrical wave impedances approach the impedances of their plane wave counterparts. That is

$$z^{out} \sim \frac{\rho v_f}{\cos(\theta)} \qquad z^{in} \sim -\frac{\rho v_f}{\cos(\theta)} \tag{3.10}$$

where $k_r = k\cos(\theta)$. In the small argument limit (i.e. as $k_r r \to 0$), these impedances each approach the same form

$$z^{out} \sim z^{in} \sim i\omega\rho r \ln(k_r r) \tag{3.11}$$

We see from this that as r goes to zero (for non-zero k_r), the impedance approaches zero. This peculiar behavior of the impedance of a monochromatic cylindrical wave near the axis is unlike the impedance of a plane wave which is constant throughout space.

3.2.2 The Energy Density of a Cylindrical Wave

Following Brekhovskikh [6], for $e^{\pm i\omega t}$ time dependence, the radial component of time-averaged energy density, or radial power density, is given by

$$< I_r > = \frac{1}{2} \mathrm{Re} \left\{ p \, v_r^* \right\} \tag{3.12}$$

where, as before, p and v_r are the pressure and the radial component of velocity of the field and $< >$ denotes a time average. Using (3.6) we may express $< I_r >$ in terms of displacement potential as

$$< I_r > = - \frac{\omega^3 \rho}{2} \mathrm{Re} \left\{ -i\phi \left\{ \frac{\partial \phi}{\partial r} \right\}^* \right\} \tag{3.13}$$

where we have assumed, as always, that ω is real-valued. This expression is valid only for positive values of frequency.

A statement of conservation of energy is that the time-averaged radial energy density must be non-negative. That is, it must be true that

$$< I_r > \geq 0 \tag{3.14}$$

This statement means that power can only flow radially away from the axis, or equivalently, power cannot be absorbed by the axis.

Just as we did with impedance, we now examine $< I_r >$ for the case of incoming and outgoing monochromatic cylindrical waves. Specifically, for $\phi = H_0^{(1)}(k_r r)$, equation (3.13) becomes

$$< I_r > = - \frac{\omega^3 \rho}{2} \mathrm{Re} \left\{ i k_r^* \, H_0^{(1)}(k_r r) \; H_1^{(1)*}(k_r r) \right\} \tag{3.15}$$

We now examine this relation separately for the case where k_r is real-valued (i.e. for a propagating wave) and for the case where k_r is positive imaginary (i.e. for an evanescent wave). In the propagating case, equation (3.15) reduces to

$$\langle I_r \rangle = \frac{\omega^3 \rho}{\pi r} \tag{3.16}$$

where we have made use of the Wronskian relations (Table 3-1). Here, the $1/r$ dependence is due to geometrical spreading. Specifically, in order for the total energy to be constant for all values of r, the density must behave as $1/r$. This result differs from the plane wave case, where the energy density is a constant throughout space.

In the evanescent region, equation (3.15) reduces to $\langle I_r \rangle = 0$, indicating that there is no power flow when the radial component of wavenumber is positive imaginary. This same result occurs in the plane wave case.

For the case of an incoming cylindrical wave, $\phi = H_0^{(2)}(k_r r)$, in the propagating region, we find that $\langle I_r \rangle$ is given by the negative of equation (3.16) indicating that the incoming cylindrical wave carries energy toward the axis, on the average. In the evanescent region, however, the energy density in the incoming cylindrical wave is not zero, as it is in the outgoing case. This is because, for the choice of the sign on k_r, the $H_0^{(2)}$ wave grows exponentially rather than decays. The result in the evanescent region is given by

$$\langle I_r \rangle = \frac{2\omega^3 \rho}{\pi r} \tag{3.17}$$

The zeroth order Bessel function, J_0, is given by the sum of incoming and outgoing cylindrical waves (Table 3-1), and consequently, takes on the interpretation of a standing wave radially. For such a wave, the radial time-averaged energy density is zero in both the homogeneous and inhomogeneous regions.

3.3 Representation of the Source Field

It is well known that the (direct) pressure field due to a point source, with waveform $s(t)$, in an infinite homogeneous fluid medium of speed v_f, located on the axis of a cylindrical coordinate system at a distance z_0 from the origin, is given by

$$p_d(z,r,t) = \frac{1}{R_o}\, s(t - R_o / v_f) \tag{3.18}$$

where R_o is the distance from the field point to the source and is given by

$$R_o = + \sqrt{r^2 + (z - z_o)^2} \tag{3.19}$$

Here we see that the signal observed at any point in space is simply a delayed and scaled version of the source pulse. The $1/R_o$ decay is due to geometrical spreading in three dimensions. The singularity at the source location is due to the point nature of the source. Infinite pressure is required from the point in order to achieve a non-zero illumination of the medium.

In order to decompose the direct source field into outward propagating cylindrical waves, we first recast (3.18) in term of the Fourier transform of the source pulse, $S(\omega)$, as follows

$$p_d(z,r,t) = \frac{1}{2\pi} \int_{-\infty}^{\infty} S(\omega) \left\{ \frac{1}{R_o}\, e^{i\omega R_o / v_f} \right\} e^{-i\omega t}\, d\omega \tag{3.20}$$

We then make use of the following identity [16]

$$\frac{1}{R_o}\, e^{i\omega R_o / v_f} = \frac{1}{2\pi} \int_{-\infty}^{\infty} \pi i\, H_0^{(1)}(k_r r)\, e^{ik_z(z - z_o)}\, dk_z \tag{3.21}$$

Substituting (3.21) into (3.20) gives

$$p_d(z,r,t) = \frac{1}{(2\pi)^2} \int_{-\infty}^{\infty} \int_{-\infty}^{\infty} \left\{ \pi i\, S(\omega)\, H_0^{(1)}(k_r r)\, e^{-ik_z z_o} \right\} e^{ik_z z} e^{-i\omega t}\, d\omega\, dk_z \tag{3.22}$$

This is the desired source field representation. Note that it is in the form of a 2D Fourier transform. Specifically, the 2D transform of the direct field over z and t, with r as a parameter, is given by the expression in brackets in (3.22).

The field due to an array of point sources along the axis can be obtained as the sum of the fields associated with each of the points which comprise the array. Specifically, for a source spatial distribution of the form $d(z)\ \delta(r)$, the field is obtained by multiplying (3.22) by $d(z_0)$ and integrating over all z_0. It follows directly that

$$p_d(z,r,t) = \frac{1}{(2\pi)^2} \int_{-\infty}^{\infty} \int_{-\infty}^{\infty} \left\{ \pi i\ S(\omega)\ D(k_z)\ H_0^{(1)}(k_r r) \right\} e^{ik_z z} e^{-i\omega t}\, d\omega\, dk_z \tag{3.23}$$

where $D(k_z)$ is the Fourier transform of $d(z)$. The direct pressure field due to a source array is necessarily infinite in the domain of the source (i.e. at $r = 0$ and at those values of z such that $d(z) \neq 0$) because the field is singular at each of the point sources which make up the distribution.

3.4 The Cylindrical Wave Reflection Coefficient

We now complicate the geometry by surrounding the homogeneous fluid medium we have been considering with a cylindrically stratified solid formation and consider the interaction of the cylindrical waves which compose the source with such a formation model. Specifically, in equation (3.23) the field due to the source was decomposed into a weighted integral of cylindrical waves of the form

$$H_0^{(1)}(k_r r)\ e^{ik_z z}\ e^{-i\omega t} \tag{3.24}$$

This wave, in propagating radially outward, will enter the cylindrically stratified medium and a reflected wave will result. The reflected cylindrical wave will carry information about the stratified medium. Because we have assumed cylindrical stratification, the reflected wave will necessarily be of the form

$$R(k_z,\omega)\ H_0^{(2)}(k_r r)\ e^{ik_z z}\ e^{-i\omega t} \tag{3.25}$$

That is, a cylindrical wave incident on a cylindrically stratified medium will result in a reflected cylindrical wave. The frequency of the reflected wave is the same as the incident wave and the angle of incidence (i.e. the axial component of wavenumber) will equal the angle of reflection. In this sense, the cylindrical wave is an eigenfunction of a cylindrically stratified medium.

The quantity $R(k_z, \omega)$ in (3.25) is referred to as the cylindrical wave reflection coefficient and is the eigenvalue associated with the cylindrical wave eigenfunction. The reflection coefficient is rigorously defined by the relations (3.24) and (3.25). This coefficient is, in general, a complex-valued quantity which depends upon the frequency and incidence angle of the incident wave. Any information about the stratified medium is summarized in this coefficient.

3.4.1 An Impedance Formulation

It is instructive at this point, and useful in Chapter IV, to express the cylindrical wave reflection coefficient in terms of the impedance functions discussed in Section 3.2.1. Specifically, the form of the radial component of acoustic impedance for a displacement potential of the form

$$\phi = H_0^{(1)}(k_r r) + R\, H_0^{(2)}(k_r r) \tag{3.26}$$

is obtained by substituting (3.26) into (3.7). The result is

$$z_r = -i \left\{ \frac{\omega \rho}{k_r} \right\} \frac{H_0^{(1)}(k_r r) + R\, H_0^{(2)}(k_r r)}{H_1^{(1)}(k_r r) + R\, H_1^{(2)}(k_r r)} \tag{3.27}$$

If we solve for R in (3.27), we obtain the result

$$R(k_z, \omega) = -\frac{H_1^{(1)}(k_r r)}{H_1^{(2)}(k_r r)} \frac{z_r - z^{out}}{z_r - z^{in}} \tag{3.28}$$

where z^{out} and z^{in} are given by (3.8) and (3.9).

We now offer a physical interpretation to equation (3.28). Suppose that the medium

which surrounds the axis is a homogeneous fluid from the axis out to the borehole/formation interface, $r=a$. Then, by evaluating (3.28) at $r=a$, z_r acquires the interpretation of the total impedance of the formation, which we refer to from now on as z^{form}, and z^{out} and z^{in} are, as before, the impedances of the incident and reflected cylindrical waves. All these impedances are measured at the borehole wall.

The Hankel function ratio, $H_1^{(1)}/H_1^{(2)}$, represents the phase shift incurred in propagating from the borehole axis out to the formation and back in the homogeneous fluid. This is evident from the large argument limiting form for this ratio (Table 3-1) given by

$$\frac{H_1^{(1)}(k_r a)}{H_1^{(2)}(k_r a)} \sim i\, e^{2ik_r a} \tag{3.29}$$

Note that this asymptotic phase shift differs from that of the plane wave case by the factor of i. This implies that, in the limit as $k_r a \to \infty$, the cylindrical wave reflection coefficient approaches $-i$ times the corresponding plane wave reflection coefficient. This is true since the incident and reflected wave impedance terms in (3.28) approach their planar analogs, as does the impedance of the solid formation (Chapter IV).

Two degenerate cases of the cylindrical wave reflection coefficient are that of a perfectly hard formation, $z^{form} = \infty$, and that of a perfectly soft formation, $z^{form} = 0$. In these cases, the cylindrical wave reflection coefficient reduces to

$$R_{hard} = -\frac{H_1^{(1)}(k_r a)}{H_1^{(2)}(k_r a)} \qquad R_{soft} = -\frac{H_0^{(1)}(k_r a)}{H_0^{(2)}(k_r a)} \tag{3.30}$$

These degenerate cases are particularly useful when analytic, as opposed to numerical, results are desired.

3.4.2 Implications of Energy Conservation

In this section, we examine the time-averaged radial energy density, $< I_r >$, for the case of a displacement potential of the form (3.26). Upon substituting (3.26) into (3.13), we find that

$$< I_r > = -\frac{\omega^3 \rho}{2} \mathrm{Re} \left\{ (ik_r) \left[H_o^{(1)}(k_r r) + R\ H_o^{(2)}(k_r r) \right] \left[H_1^{(1)*}(k_r r) + R^* H_1^{(2)*}(k_r r) \right] \right\} \tag{3.31}$$

For k_r real-valued, equation (3.31) reduces to

$$< I_r > = \frac{\omega^3 \rho}{\pi r} \left(1 - |R|^2 \right) \tag{3.32}$$

Here we see that, for the case of propagating cylindrical waves the condition $|R| \leq 1$ must be true so that $< I_r >$ is a non-negative quantity. For non-propagating (inhomogeneous) cylindrical waves, equation (3.31) reduces to

$$< I_r > = \frac{2\omega^3 \rho}{\pi r} \left(\mathrm{Re}(R) - |R|^2 \right) \tag{3.33}$$

In order that $< I_r >$ be non-negative, it must be true that

$$|R| \leq \cos(\theta) \leq 1 \tag{3.34}$$

where $R = |R|\, e^{i\theta}$. However, in order for (3.34) to be satisfied, it must also be true that

$$\mathrm{Re}\,(R) \geq 0 \tag{3.35}$$

These last conditions are even more restrictive than $|R| < 1$. This evanescent result differs from that of the plane wave case where Frisk [15] and other have shown that the plane wave reflection coefficient may become infinitely large.

3.5 The Acoustic Field in the Borehole

The reflected wave in (3.25) will propagate in towards the borehole axis and give rise to

an outward propagating wave again. In propagating out for the second time, the formation will be encountered again, there will be another reflection which propagates in, and then out, and the process continues ad infinitum. Summing all these wave gives the field in the borehole due to an incident monochromatic cylindrical wave. Ignoring the $e^{ik_z z}e^{-i\omega t}$ factor common to each term, we have

$$H_o^{(1)}(k_r r) + \left\{ H_o^{(1)}(k_r r) + H_o^{(2)}(k_r r) \right\}\left[R(k_z,\omega) + R^2(k_z,\omega) + R^3(k_z,\omega) + \cdots \right] \tag{3.36}$$

The first term in (3.36) represents the initial incident cylindrical wave, due to the source. The remaining terms correspond to either incoming or outgoing waves having undergone some number of encounters with the borehole wall.

To find the total solution for the field in the borehole when the source is a temporal transient, with waveform $s(t)$, and a spatial filament, with distribution $d(z)\,\delta(r)$, we insert (3.36) into (3.23) in place of $H_o^{(1)}(k_r r)$. In this way, the first term will be synthesized into the direct source field and the remaining terms become the total reflected field in the borehole due to the source. We write this as follows

$$p(z,r,t) = p_d(z,r,t) + p_r(z,r,t) \tag{3.37}$$

where $p_d(z,r,t)$ is given by (3.23) and $p_r(z,r,t)$, the reflected field, is given by

$$p_r(z,r,t) = \frac{1}{(2\pi)^2}\int_{-\infty}^{\infty}\int_{-\infty}^{\infty}\left\{ 2\pi i\, S(\omega)\, D(k_z)\, J_o(k_r r) \sum_{m=1}^{\infty} R^m(k_z,\omega) \right\} e^{-i\omega t}e^{ik_z z}\,dk_z\,d\omega \tag{3.38}$$

Here we have used the fact that $H_o^{(1)}+H_o^{(2)}=2J_o$, where J_o is the zeroth order Bessel function. As discussed earlier, from the outgoing and incoming wave interpretations of $H_o^{(1)}$ and $H_o^{(2)}$, we interpret J_o as a standing wave in the radial direction.

Equations (3.23), (3.37) and (3.38) represent the ray theoretic integral solution [31][38]

for the field in the borehole in terms of the cylindrical wave reflection coefficient and the source descriptors, $s(t)$ and $d(z)$. These relations are valid for all z and from $r=0$ out to the radius where the cylindrical stratification begins (which may be infinitesimally close to the axis, or as far away as the borehole/formation interface).

Rather than view the field within the borehole as a sum of multiply reflected waves, one can alternatively adopt a modal theory viewpoint. In this approach, the field within the borehole is assumed to be of the form

$$H_0^{(1)}(k_r r) + A(k_z, \omega)\, J_0(k_r r) \tag{3.39}$$

rather than of the form of (3.36). Here, A is referred to as the cylindrical wave modal coefficient. Equation (3.39) leads directly to the solution

$$p_r(z,r,t) = \frac{1}{(2\pi)^2} \int_{-\infty}^{\infty} \int_{-\infty}^{\infty} \left\{ \pi i\, S(\omega)\, D(k_z)\, J_0(k_r r)\, A(k_z, \omega) \right\} e^{-i\omega t} e^{ik_z z}\, dk_z\, d\omega \tag{3.40}$$

The locus of (k_z, ω) pairs for which $A(k_z, \omega)$ is infinite define the dispersion relations for the modes of the cylindrical waveguide [5][27][33][36][42]. This modal representation of the field will serve in Chapter IV as the basis for the numerical evaluation of synthetic acoustic well logging data.

3.6 Comments

The relation between $R(k_z, \omega)$ and $A(k_z, \omega)$ is given by

$$A(k_z, \omega) = 2 \sum_{m=1}^{\infty} R^m(k_z, \omega) \tag{3.41}$$

We can sum this series in closed form if and only if the reflection coefficient is strictly less than unity in magnitude. As we saw in the last section, for positive real-valued frequencies the

reflection coefficient is theoretically guaranteed by conservation of energy to be less than or equal to unity in magnitude. It follows that if there is any attenuation in the geometry (i.e. if the medium is not perfectly elastic everywhere) then the reflection coefficient (at positive frequencies) will be strictly less than unity in magnitude. Since we can safely assume that this is the case, then we can perform the closed form sum to obtain the relations

$$A(k_z,\omega) = \frac{2\,R(k_z,\omega)}{1-R(k_z,\omega)} \qquad R(k_z,\omega) = \frac{A(k_z,\omega)}{A(k_z,\omega)+2} \qquad \text{for} \quad \omega > 0 \tag{3.42}$$

Here, we see that the relation between A and R is one-to-one and that the condition $|R| < 1$ implies the condition $\mathrm{Re}\,(A) > -1$, and vice versa. In addition, the (k_z,ω) pairs for which $R=1$ define the dispersion relations for the modes of the waveguide.

At negative real-valued frequencies, we note from equation (3.40) that the modal coefficient must have negative conjugate symmetry in frequency so that the reflected component of the total field will be real-valued. That is,

$$A(k_z,-\omega) = -A^*(k_z,\omega) \tag{3.43}$$

In this way, the transform of A over frequency will be imaginary-valued and, when multiplied by the factor of i in (3.40), a real-valued result follows. Using this frequency symmetry of A in equation (3.43) to determine the frequency symmetry in the reflection coefficient, we see that

$$R(k_z,-\omega) = \frac{-R^*(k_z,\omega)}{1-2\,R^*(k_z,\omega)} \tag{3.44}$$

Here we see that if $R(k_z,\omega) = 1/2$, then $R(k_z,-\omega) = \infty$. We conclude that the reflection coefficient is not constrained to be less than unity in magnitude at negative frequencies and, in fact, may become infinitely large.

The lack of conjugate symmetry in frequency in equation (3.44) implies that the Fourier

transform of the reflection coefficient will be a complex-valued time signal. In addition, it can be shown that the Fourier transform of the reflection coefficient is a non-causal time signal. These two facts together imply that the primary reflection of a real-valued causal source pulse off the formation wall will arrive at a receiver before $t = 0$ and in addition, the reflection will have a complex-valued pressure field. Clearly this is not physically meaningful and we conclude that the representation of the field in the hole as a sum of individual reflections is not physical.

The non-physical nature of the reflection representation can be argued on the grounds that an individual reflection is not measurable. That is, one cannot design an experiment to measure an individual reflection. In any experiment an infinite number of reflections will necessarily be generated. This is not the case in a planar waveguide where one side of the guide can be removed to infinity, thus leaving only the primary reflection. In the cylindrical case, as the borehole radius becomes infinitely large, there are still an infinite number of reflections.

Part of the problem with the physical interpretation of the individual reflections has to do with the lack of conjugate symmetry in frequency. That is, if the reflection coefficient at negative frequencies were equal to the conjugate of the reflection coefficient at positive frequencies, then the transform of the reflection coefficient would be real-valued and the reflection coefficient would be less than unity in magnitude for both positive and negative values of frequency. The transform of the reflection coefficient would remain non-causal, however. Nevertheless, we will find it convenient to redefine the reflection coefficient in this manner. From equation (3.42), we see that if R is conjugate symmetric, then so is A. With this observation, we can rewrite (3.40) as

$$p_r(z,r,t) = \frac{1}{(2\pi)^2} \int_{-\infty}^{\infty} \int_{-\infty}^{\infty} \left\{ \pi i \, \mathrm{sgn}(\omega) \, S(\omega) \, D(k_z) \, J_o(k_r r) \, A(k_z, \omega) \right\} e^{-i\omega t} e^{ik_z z} dk_z d\omega \tag{3.45}$$

and equation (3.38) as

$$p_r(z,r,t) = \frac{1}{(2\pi)^2}\int_{-\infty}^{\infty}\int_{-\infty}^{\infty}\left\{ H(\omega)\ S(\omega)\ D(k_z)\ J_0(k_r r)\ \sum_{m=1}^{\infty} R^m(k_z,\omega)\right\} e^{-i\omega t} e^{ik_z z}\, dk_z\, d\omega \tag{3.46}$$

where

$$H(\omega) = 2\pi i\ \mathrm{sgn}(\omega) \tag{3.47}$$

Here, $H(\omega)$ is recognized as a Hilbert transform [26] and has a Fourier transform of $h(t) = 2/t$, which is noted to be non-causal

As a final comment, the expression for the reflected component of the total field simplifies if $r = 0$ since the zeroth order Bessel function has a value of unity at the origin. Thus, if the receivers are restricted to lie on the borehole axis, then the Bessel function in equation (3.45) effectively disappears from the relationship.

3.7 Relating the Reflection Coefficient to Reflected Component of the Field

The goal of this chapter was to develop a relationship between the reflection coefficient and the reflected component of the field. We have found that this relationship takes the form of a 2D Fourier transform and that, if the receivers are restricted to lie on the borehole axis, then the relationship simplifies considerably. Specifically, the reflected component of the field on the axis is related to the cylindrical wave reflection coefficient by

$$p_r(z,t) = \frac{1}{(2\pi)^2}\int_{-\infty}^{\infty}\int_{-\infty}^{\infty}\left\{ H(\omega)\ S(\omega)\ D(k_z)\ \sum_{m=1}^{\infty} R^m(k_z,\omega)\right\} e^{-i\omega t} e^{ik_z z}\, dk_z\, d\omega \tag{3.48}$$

where $p_r(z,t)$ will be used to denote the reflected component of the field on the axis. Again, the reflection coefficient in this formulation is strictly less than unity in magnitude so that the integration and summation operations can be interchanged, or so that the series can be summed in closed form. In addition, the reflection coefficient is conjugate symmetric in frequency so that it transforms to a real-valued time signal.

If we now denote the 2D Fourier transform of the reflection coefficient as $r(z,t)$, and refer to it as the reflection coefficient signal, then we can interpret equation (3.48) in terms of 2D space-time invariant convolutions as

$$p_r(z,t) = s_h(t)\ d(z) \ ** \left\{ r(z,t) + r(z,t) ** r(z,t) + \cdots \right\} \tag{3.49}$$

where $s_h(t)$ denotes the convolution of the source pulse waveform, $s(t)$, with the Hilbert transform, $h(t) = 2/t$, and the two asterisks denote 2D convolution. A block diagram of this 2D reverberatory system is shown in Figure 3-2.

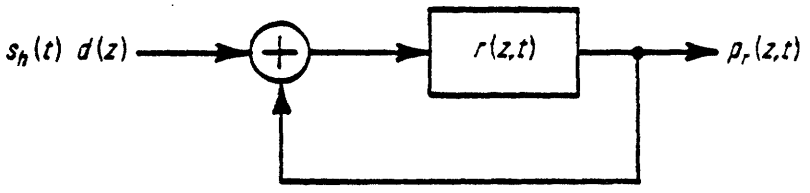

Figure 3-2. Relating the reflection coefficient to the reflected component of the field on the axis

3.8 Conclusions

In this chapter we developed a relationship between the reflection coefficient and the reflected component of the pressure field on the axis of the hole. In the remaining chapters of this thesis we will discuss the estimation of the reflection coefficient from measurements of this field. The relationship we found takes the form of a 2D reverberation system and the processing problem we will encounter is one of dereverberation.

In deriving this relationship, a number of interesting aspects concerning wave propagation in cylindrically stratified media were uncovered. In particular, the impedance and energy density properties of monochromatic cylindrical waves, the impedance interpretation of the reflection

coefficient and the implications of conservation of energy on the reflection coefficient were all examined and found to be different than the analogous properties in a planar geometry. In addition, the reflection process in a cylindrical geometry was found to be non-physical, also unlike the planar case. It is felt that the properties of cylindrical waves and of the cylindrical wave reflection and modal coefficients which we have studied in this chapter are fundamental to a thorough understanding of wave propagation in cylindrically stratified media.

IV. THE NUMERICAL EVALUATION OF SYNTHETIC DATA

4.1 Introduction

In this chapter, we develop a fast and accurate method for the computation of arrays of synthetic acoustic well logging waveforms. In Chapter VI we will use arrays of synthetic data generated by this method to test and evaluate the iterative maximum likelihood (ML) dereverberation we develop for estimating the reflection coefficient (Chapter V). The testing and evaluation of the ML technique (or more generally, any new processing method for the estimation of any formation parameters) using synthetic data is desirable for several reasons. Synthetic data provides a more flexible and controlled environment in which to develop and test a new processing method than that provided by either data recorded in a laboratory or data taken in the field. The model which underlys the waveforms is known, as are the parameters of the model. This allows for a meaningful evaluation of an estimation technique. In the case of actual data in particular, the model and/or parameters are not often known with sufficient confidence to afford a meaningful test. Also, with synthetic data, the level of numerical noise is under some control and can often be made negligibly small. Furthermore, there is complete control over the choice of a source waveform, as well as the number and placement of the receiver array elements. In both experimental laboratory and real data, the amount of noise in the data is much harder to control, and not often known, and the instrumentation system used to acquire the data is far less flexible. Following the successful performance of a new estimation method on synthetic data, the method should then be applied to laboratory data, if available, or to actual well logging data recorded in the field.

Synthetic data is useful in other acoustic well logging contexts which are not treated in this thesis. For example, arrays of synthetic waveforms are useful as an aid in interpreting and understanding actual sonic well logging waveforms. The influence of formation parameters on the data is often complicated and not well understood. Arrays of theoretical waveforms

corresponding to arbitrary choices of formation parameters can be used to study their effects. Also, in a related area, synthetic data can, in theory, be used in an analysis-by-synthesis approach to data inversion. In such a scheme, synthetic data is generated to match actual data as closely as possible. The estimates of the formation parameters are then taken to be the parameters of the theoretical model of the formation. In practice, a series of iterations on the set of formation parameters will be required before convergence to a closest match occurs.

4.1.1 Previous Work

The primary reference on the subject of numerically generating synthetic acoustic well logging waveforms is a paper by Tsang and Rader [37]. In this paper, a "real axis integration" method is developed for the numerical evaluation of an individual waveform. The emphasis in this work, however, is on the issue of numerical accuracy while the associated issue of computation time is largely ignored. We have found that while the method is numerically stable, it can consume inordinate amounts of computation time because of the large number of Hankel functions which must be repeatedly evaluated for complex-valued arguments. Furthermore, when an entire array of synthetic waveforms in needed, the individual generation of each waveform in the array using this approach is certain to be prohibitively slow.

Other literature involving the generation of synthetic data [9][32][40] contain surprisingly few details concerning the method which was used. These papers used synthetic data as an aid to understanding wave propagation in the borehole and consequently, the numerical aspects of how the data was computed were of secondary importance. This is particularly true of the two papers which appeared prior to the Tsang and Rader paper; one by White and Zechman [40] and the other by Rosenbaum [32]. In the more recent paper by Cheng and Toksöz [9], Tsang's "real axis" method was used, but details on issues of numerical accuracy and computation time were not included.

4.1.2 Contribution of this Work

In this chapter, unlike the previous efforts, we place the major emphasis on minimizing the computation time for a given level of numerical accuracy. Briefly, we adapt Tsang's "real axis" method so that it will compute entire arrays of waveforms simultaneously, and we speed up the method through the use of a table lookup and interpolation scheme for the repeated evaluation of Hankel functions for complex-valued arguments.

More specifically, the major contribution of this chapter is in the efficient evaluation of the modal coefficient on a grid in the frequency-wavenumber domain. The repeated evaluation of this coefficient is responsible for the overwhelming majority of the computation time required to generate synthetic data. In fact, a percentage reduction in the time to evaluate this coefficient translates to roughly the same percentage reduction in the overall computation time. A closer inspection reveals that, within the theoretical expression for the modal coefficient, there are a number of Hankel functions which must be evaluated for complex-valued arguments. This differs from the analogous problem in a planar geometry, where only trigonometric function evaluations are required and consequently, data can be rapidly generated. The evaluation of the Hankel functions using a dedicated evaluation subroutine has been found to consume essentially all of the computation time. In this chapter we show that, for the specific case of an infinite homogeneous solid formation model, the use of a table lookup and interpolation scheme for the evaluation of these special functions results in roughly an order of magnitude savings in computation time, relative to the direct evaluation approach. This remarkable savings easily outweighs the modest increase in storage requirements needed to accomodate the table.

With the savings in computation time reported here, fast table-based methods have since been developed for the layered formation model [7][8]. Furthermore, the development of analysis-by-synthesis methods for data inversion in borehole applications may now be feasible, as they are in planar problems. This is the subject of ongoing research and may eventually have a significant effect on the way data from the from the field is processed.

4.1.3 Overview and Outline

In this chapter, we consider the numerical evaluation of space-time samples of the reflected component of the acoustic field along the axis of a cylindrical axi-symmetric elastic geometry. We denote this field as $p_r(z,t)$. The source is, in general, spatially distributed along the axis and is described mathematically by $d(z)$. Temporally, the source is a transient, with waveform $s(t)$. The theoretical expression for this field was derived in Chapter III and is repeated here.

$$p_r(z,t) = \frac{1}{(2\pi)^2} \int_{-\infty}^{\infty}\int_{-\infty}^{\infty} \left\{ \pi i \, \mathrm{sgn}(\omega) \; S(\omega) \; D(k_z) \; A(k_z,\omega) \right\} e^{ik_z z} \, e^{-i\omega t} \, dk_z \, d\omega \qquad (4.1)$$

To review, $S(\omega)$ and $D(k_z)$ denote the Fourier transforms of the source descriptors, $s(t)$ and $d(z)$, and $A(k_z,\omega)$ is referred to as the cylindrical wave modal coefficient. Physically, k_z is the axial component of the total wavenumber, k, which is given by $k = \omega/v_f$. This formulation for the field is a recast but identical version of the point source formulation presented by both Tsang [37] and Cheng [9] (i.e. when $d(z)=\delta(z)$ and $D(k_z)=1$). In this sense, this formulation is more general.

The treatment of the numerical generation of samples of $p_r(z,t)$ in equation (4.1) is divided into 3 sections. In the first, we briefly present Tsang's "real axis integration" method for numerically approximating equation (4.1). In the second part, we discuss the efficient evaluation of the cylindrical wave modal coefficient. Then, in the third part, we discuss the design of parametric models for the source descriptors, $s(t)$ and $d(z)$.

4.2 Tsang's "Real Axis Integration" Method

In this section we discuss the discretization and approximation of the continuous 2D Fourier transform representation of the field given in equation (4.1). Our approach will be to truncate the limits of integration and sample the transform of the field (i.e. the expression in brackets in (4.1)) on a uniform grid in the frequency-wavenumber domain. We then approximate the continuous transforms with discrete Fourier transforms (DFT's) and implement

these using the radix-2 fast Fourier transform (FFT) algorithm. In this way, entire arrays of waveforms are efficiently generated. This approach is different from that of both Tsang [37] and Cheng [9] who generated only a single waveform by using Simpson's rule to perform the axial wavenumber integral. It should be noted that if only a few waveforms are needed, then the generation of each signal individually using a Simpson's rule approach will be faster than our approach using the FFT in which hundreds of waveforms are necessarily generated.

This section is divided into two parts. In the first, we discuss the region of frequency-wavenumber space in which the transform is significant and therefore must be sampled. By avoiding unnecessary evaluations of the modal coefficient, a significant savings in computer time will result. In the second, we discuss the selection of appropriate sampling periods in both frequency and wavenumber. In this part, the essence of the "real axis" method is presented.

4.2.1 The Region of Integration

The region of (k_z, ω) space in which we must sample the transform of the field is defined by the intersection of the regions in which $A(k_z, \omega)$ and the product, $S(\omega)\ D(k_z)$, are each significant. This is illustrated in Figure 4-1. The region of frequency-wavenumber space which the source excites will, in general, consist of a set of rectangular shaped areas defined by the intersection of the pass-bands in $S(\omega)$ and $D(k_z)$. In contrast, the modal coefficient is significant in a roughly triangular region defined approximately by $k_z < \omega/v_f$. Outside this region, the axial component of wavenumber is larger than the total wavenumber, implying that the radial component is imaginary. Thus, waves in this region decay exponentially in the radial direction and decay significantly in propagating out to the wall and back. These waves make a negligible contribution to the field in the hole and can be neglected.

4.2.2 The Selection of the Sampling Periods

Having defined the finite sized region of (k_z, ω) space in which we must sample the theoretical transform of the field, we now consider the selection of appropriate values for the

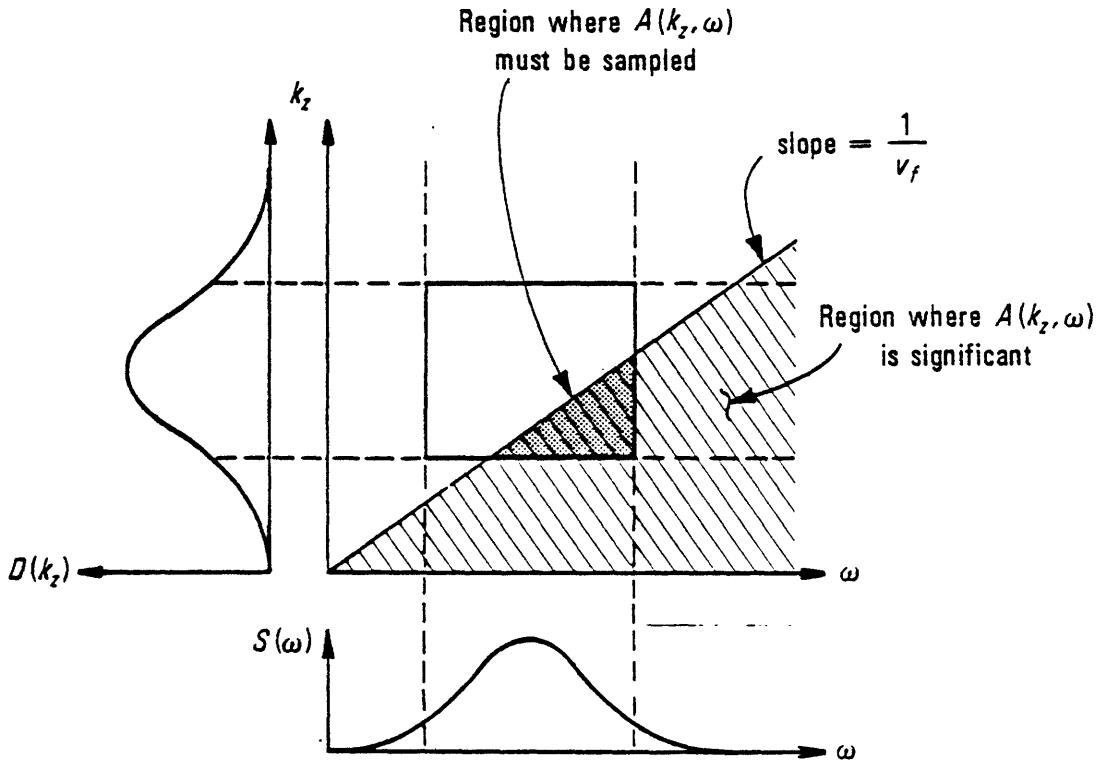

Figure 4-1. The region of integration

sampling periods in frequency and wavenumber, $\Delta\omega$ and Δk_z. Here we develop the "real axis integration" method of Tsang from a somewhat different perspective.

By sampling the transform of the field in the frequency-wavenumber domain, the effects of aliasing will be present in the synthetic data. The actual space-time domain region of support of the borehole wavefield will be periodically reproduced every T_{max} and Z_{max} in time and space, where $T_{max} = 2\pi/\Delta\omega$ and $Z_{max} = 2\pi/\Delta k_z$. In order to ensure the numerical accuracy of the resulting synthetic waveforms, T_{max} and Z_{max} must be chosen large enough so that the aliasing is not significant. We now examine the region of support of the space-time field so that appropriate values of T_{max} and Z_{max}, and consequently, $\Delta\omega$ and Δk_z, can be made.

In Figure 4-2, we show the space-time region of support for the reflected component of the pressure field on the axis of the borehole for the case of a perfectly elastic formation model. Note that at long source-to-receiver spacings the energy is contained in a wedge-shaped region defined roughly by the maximum and minimum sound speeds in the geometry. Because we

have assumed that the geometry is perfectly elastic, the energy in each time signal remains essentially the same as the source-receiver spacing increases. That is, no energy is lost to the formation, or equivalently, the energy is ideally trapped in the borehole waveguide system. Because the signal duration (i.e. a horizontal slice of the wedge region) increases linearly with increasing spacing, the "average amplitude" of the signal must be decaying roughly as $1/\sqrt{z}$ in order that the energy remain constant with z. This is a slow decay rate and is the reason why we have drawn the region of support in Figure 4-2 as open-ended.

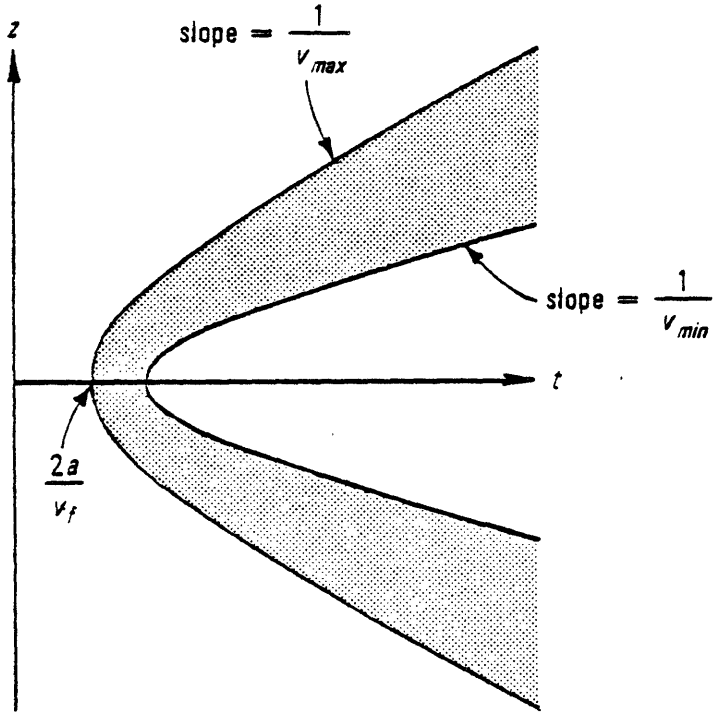

Figure 4-2. The space-time region of support of the borehole field

The semi-infinite nature of the region of support raises major issues with respect to aliasing. In an effort to reduce the aliasing problem, one might consider deforming the contour of integration from the real frequency axis to a Laplace contour, defined by $\omega = \omega' + i\omega''$ where $-\infty < \omega' < \infty$ and ω'' is a positive constant. In this way, equation (4.1) becomes

$$p_r(z,t) = \frac{e^{\omega'' t}}{(2\pi)^2} \int_{-\infty}^{\infty}\int_{-\infty}^{\infty} \left\{ \pi i \, \mathrm{sgn}(\omega') \, S(\omega) \, D(k_z) \, A(k_z,\omega) \right\} e^{ik_z z} \, e^{-i\omega' t} \, dk_z \, d\omega' \tag{4.2}$$

By numerically evaluating samples of $e^{-\omega'' t} \, p_r(z,t)$ instead of $p_r(z,t)$ itself, the region of support in Figure 4-2 is exponentially tapered in time and, in effect, becomes finite in size. In this way, periodic reproduction of finite region will produce significantly less aliasing.

The use of a Laplace contour of integration in the frequency transform is due to Tsang, who referred to this approach as the "real axis integration" method because the integration over k_z is done along the real k_z-axis. However, Tsang motivated the method from a different perspective. For a given real-valued frequency, he located the singularities of the modal coefficient in the complex k_z-plane and found that, for a perfectly elastic geometry, the singularities lie on the real k_z-axis. Therefore, the modal coefficient is unbounded at places on the contour where we wish to sample it. To circumvent this problem, Tsang showed that the singularities move off the real k_z-axis if the frequency is made complex-valued. Furthermore, he showed that the distance they move off is at least a distance of ω''/v_{max}, where, as always, the double prime denotes the imaginary part and v_{max} denotes the fastest speed in the problem. Given this guaranteed separation between the singularities and the path of integration, a selection of $\Delta k_z = \omega''/3v_{max}$ was made to insure that the most rapid variation in the modal coefficient is captured.

The selection of $\Delta\omega'$ is made by appealing to the causality of $p_r(z,t)$ in time for all values of z. For $e^{-i\omega t}$ time dependence, the transform of this field over time must be analytic in the upper half of the complex-valued ω-plane. Since a Laplace contour is used in the frequency integral, we are precisely a distance of ω'' from the lower half plane and a selection of $\Delta\omega' = \omega''/5$ was made to insure adequate sampling.

The selection of ω'' will depend to some degree on the precision of the computer system being used. To see this, consider the tradeoff involved in the selection of this parameter. We would ideally like to make ω'' as large as possible so that the sampling periods are large and

computation can be saved. However, having numerically generated the integral in (4.2), an exponentially increasing taper will be applied to the result. This will magnify any numerical errors associated with the approximation of the integral and, in effect, ensures us that as time increases, the noise will eventually overtake the signal. In order to ensure a high level of numerical accuracy in the waveforms out to a time t_{max}, we have found a selection of $\omega'' = 3/t_{max}$ to be adequate. However, this selection is tied to the level of numerical noise in the synthetic data, and therefore, to the selection rules for $\Delta\omega'$ and Δk_z, as well as to the precision of the computer system. The selection rules stated were found appropriate on a VAX machine using single precision floating point arithmetic in which 23 bits of storage are used for the mantissa, implying roughly 7 decimal digits of numerical accuracy. If double or quadruple precision computation is used, it is believed that the value of t at which the numerical noise dominates the signal will increase considerably. In this way, ω'' can be decreased and a large savings in computation time will result, at the expense of added storage.

The selection rules presented by Tsang, and also used here, are conservative and reflect our insistence on a high level of numerical accuracy in the synthetic waveforms. If one is willing to tolerate relatively small numerical artifacts in the waveforms, then the sampling periods can be increased and a significant savings in computation time will result.

4.3 The Evaluation of the Cylindrical Wave Modal Coefficient

In this section, we present the theoretical expression for the modal coefficient associated with an infinite homogeneous solid formation and develop an efficient table lookup and interpolation method for its evaluation. We also discuss, in less detail, the evaluation of the modal coefficient associated with a formation model consisting of cylindrical fluid layers. And finally, in still less detail, we consider a solid layered formation model. It is not possible to derive a theoretical expression for the modal coefficient associated with a continuously stratified cylindrical axi-symmetric geometry. However, such a situation can always be accurately approximated by a system of homogeneous cylindrical layers if the layer thicknesses are made

sufficiently small relative to the wavelengths involved.

In Chapter III, we related the modal coefficient, $A(k_z, \omega)$, to the cylindrical wave reflection coefficient, $R(k_z, \omega)$, by

$$A(k_z, \omega) = \frac{2\, R(k_z, \omega)}{1 - R(k_z, \omega)} \tag{4.3}$$

Assuming that the fluid in the borehole is homogeneous from the axis out to the formation, then, from Chapter III, we saw that the reflection coefficient could be formulated in terms of cylindrical wave impedances as follows

$$R(k_z, \omega) = -\Phi(k_r a)\, \frac{z^{form} - z^{out}}{z^{form} - z^{in}} \tag{4.4}$$

where z^{form} denotes the total impedance of the formation, z^{out} is the impedance of the incident outward propagating cylindrical wave and z^{in} is the impedance of the reflected inward traveling cylindrical wave. All the impedances are measured at the formation wall, $r=a$. The Φ term represents the phase shift incurred in propagating from the axis, out to the wall, and back again, and the argument to this term is the product of the borehole radius, a, with the radial component of wavenumber, k_r, which is given by

$$k_r = \sqrt{k^2 - k_z^2} \tag{4.5}$$

where $k = \omega / v_f$.

While the impedance of the formation depends upon the particular formation model under consideration, the other quantities in (4.4) do not and are given by

$$z^{out} = -\frac{i\omega\rho}{k_r}\Psi_1(k_r a) \qquad z^{in} = -\frac{i\omega\rho}{k_r}\Psi_2(k_r a) \tag{4.6}$$

and

$$\Phi(Z) = \frac{H_1^{(1)}(Z)}{H_1^{(2)}(Z)} \qquad \Psi_1(Z) = \frac{H_0^{(1)}(Z)}{H_1^{(1)}(Z)} \qquad \Psi_2(Z) = \frac{H_0^{(2)}(Z)}{H_1^{(2)}(Z)} \tag{4.7}$$

Here, Z is used to denote a complex-valued argument. In eq. (4.6), ρ represents the density of the mud in the hole and in eq. (4.7), $H_m^{(n)}$ denotes a Hankel function of order m and type n.

In this section, we consider three models for the formation and, in two cases, their associated impedance expressions. These impedances are then incorporated into (4.4) to obtain the theoretical expression for the reflection coefficient, and in turn, in (4.3), to obtain the modal coefficient. We have found this nested type of representation of the modal coefficient to be preferable to that used by both Tsang and Cheng, who each examined the particular case of an infinite homogeneous solid formation model. The representation of the modal coefficient which we use has a physical interpretation in terms of the reflection coefficient and impedances, has a one-to-one correspondence with the analogous problem of a planar liquid/solid interface geometry, and most importantly, leads to the efficient table-based scheme for its evaluation.

4.3.1 The Infinite Homogeneous Solid Formation Model

a. The Formation Impedance

The impedance of an infinite homogeneous formation model is given by

$$z^{form} = z_c^{out} \cos^2(2\theta) + z_s^{out} \sin^2(2\theta) + \zeta \tag{4.8}$$

Here, z_c^{out} and z_s^{out} denote the impedances of the transmitted outward propagating compressional and shear cylindrical waves in the formation and ζ is a function of $1/\omega$. These quantities are given by

$$z_c^{out} = -\frac{i\omega\rho_1}{k_r^{(c)}}\Psi_1(k_r^{(c)}a) \qquad z_s^{out} = -\frac{i\omega\rho_1}{k_r^{(s)}}\Psi_1(k_r^{(s)}a) \qquad \zeta = 2i\,\frac{\rho_1 v_s^2}{\omega a} \tag{4.9}$$

Here, ρ_1 is the density of the formation and $k_r^{(c)}$ and $k_r^{(s)}$ are the radial components of the compressional and shear wavenumbers in the formation, given by

$$k_r^{(c)} = \sqrt{k_c^2 - k_z^2} \qquad k_r^{(s)} = \sqrt{k_s^2 - k_z^2} \tag{4.10}$$

where the total wavenumbers, k_c and k_s, are related to the compressional and shear acoustic velocities, v_c and v_s, by $k_c = \omega/v_c$ and $k_s = \omega/v_s$. Finally, the angle, θ, in (4.8) is the transmission angle of the shear wave, defined by

$$k_r^{(s)} = k_z \cos(\theta) \tag{4.11}$$

This representation of the impedance of an infinite homogeneous formation is analogous to the impedance of an elastic half-space developed by Brekhovskikh [6]. In the limit as $\omega a \to \infty$, the impedances in (4.6), (4.8) and (4.9) approach the plane wave impedances in his formulation. However, the phase shift term, Φ, is asymptotic to $i\, e^{2i\omega a/v_f}$, which differs from the planar result by the factor of i. Thus, when inserted into (4.4), the cylindrical wave reflection coefficient differs from the plane wave reflection coefficient by a factor of $-i$.

b. A Formula for Computation

We now recast the impedance interpretation of the reflection coefficient into a slightly different form which we will use for computation.

$$R(k_z, \omega) = -\Phi(k_r a)\, \frac{\Theta - \Psi_1(k_r a)}{\Theta - \Psi_2(k_r a)} \tag{4.12}$$

where Φ and the Ψ's are defined in (4.7) and Θ is given by

$$\Theta = k_r a\, \frac{\rho_1}{\rho} \left[\frac{\Psi_1(k_r^{(c)} a)\, \cos^2(2\theta)}{k_r^{(c)} a} + \frac{\Psi_1(k_r^{(s)} a)\, \sin^2(2\theta)}{k_r^{(s)} a} - \frac{2}{k_s^2 a^2} \right] \tag{4.13}$$

In this last equation, it is useful to evaluate the trigonometric terms using the relation

$$\cos^2(2\theta) = 1 - \sin^2(2\theta) = \left\{ 1 - 2 \left\{ \frac{k_r}{k_z} \right\}^2 \right\}^2 \tag{4.14}$$

For a given set of parameters, $\{v_f, v_c, v_s, \rho, \rho_1, a\}$, and a given (k_z, ω) pair, we first compute the three total and radial components of wavenumber, using (4.5) and (4.10), and the trigonometric terms using (4.14). These quantities are then algebraically combined with the Hankel function ratio terms, according to prescription in (4.12) and (4.13), to compute the cylindrical wave reflection coefficient. Finally, the modal coefficient is obtained using (4.3).

In computing R, one should be aware of several degenerate cases. If $k_r = 0$, then $R = 1$ and the modal coefficient is infinite. If $\omega = 0$ or $k_r^{(s)} = 0$ or $k_r^{(c)} = 0$, then $R = -\Phi(k_r a)$.

c. The Efficient Evaluation of the Hankel Function Ratios

In this section, we develop an efficient table lookup and interpolation scheme for the three Hankel function ratios given in eq. (4.7). The treatment here is divided into three parts. In the first, we identify the region of the complex-valued argument plane in which we need to evaluate the ratios. In the second, we examine the behavior of each ratio in this region. Finally, the sampling, storage and interpolation designs are presented.

(i) Domain of the Arguments

The arguments to the Hankel function ratios are all in the form of a radial component of wavenumber multiplied by the borehole radius. Assuming for the moment that frequency and the velocities are each real-valued quantities, then from (4.5) and (4.10), we see that the arguments to the ratios will be either positive real or positive imaginary. If we now let frequency become complex-valued, with a positive imaginary-part as is the case in the "real-axis integration" method, then the arguments become complex-valued and lie in the first quadrant of the

complex-plane near either the real or imaginary axes.

If any of the velocities are complex-valued, then at low frequencies the associated radial wavenumber will enter the second quadrant. (An attenuative medium is often modeled by a complex sound speed, as in $v=v'-iv''$ where $v''>0$ [2]). Specifically, the argument will enter the second quadrant when the condition $\omega' v' < \omega'' v''$ is satisfied, where single primes denote real-parts and double primes denote imaginary-parts. Typically, the imaginary component of velocity is a small fraction of the real-part, and the imaginary component of frequency is a small constant, so that the argument will enter the second quadrant for only the first few samples of ω'. Therefore, only a relatively small number of second quadrant function evaluations will be required. For this reason, we use a direct algorithmic evaluation when the argument is in the second quadrant.

(ii) The Behavior of the Ratios

In Figures 4-3 and 4-4 we plot the magnitude and phase of the two impedance-related ratios, Ψ_1 and Ψ_2, for an argument in the first quadrant of the complex plane. In Figure 4-5 we plot the magnitude and phase of a demodulated version of the phase shift ratio, given by $e^{-2iZ}\Phi(Z)$. The exponential term has been included to remove the rapid large argument behavior of the phase shift ratio. In this way, a significantly smaller number of samples of the function are required.

Note from the figures that each of these ratios varies slowly for an argument with magnitude greater than roughly 2, and that for arguments of smaller magnitude, the variation is more rapid, but still well behaved. We conclude that these ratios are sufficiently slowly varying to sample and store in a table.

(iii) Sampling, Interpolation and Storage

In order to efficiently evaluate the desired ratios from the table, the computation associated with the lookup and interpolation schemes must be minimal. For this reason, we have

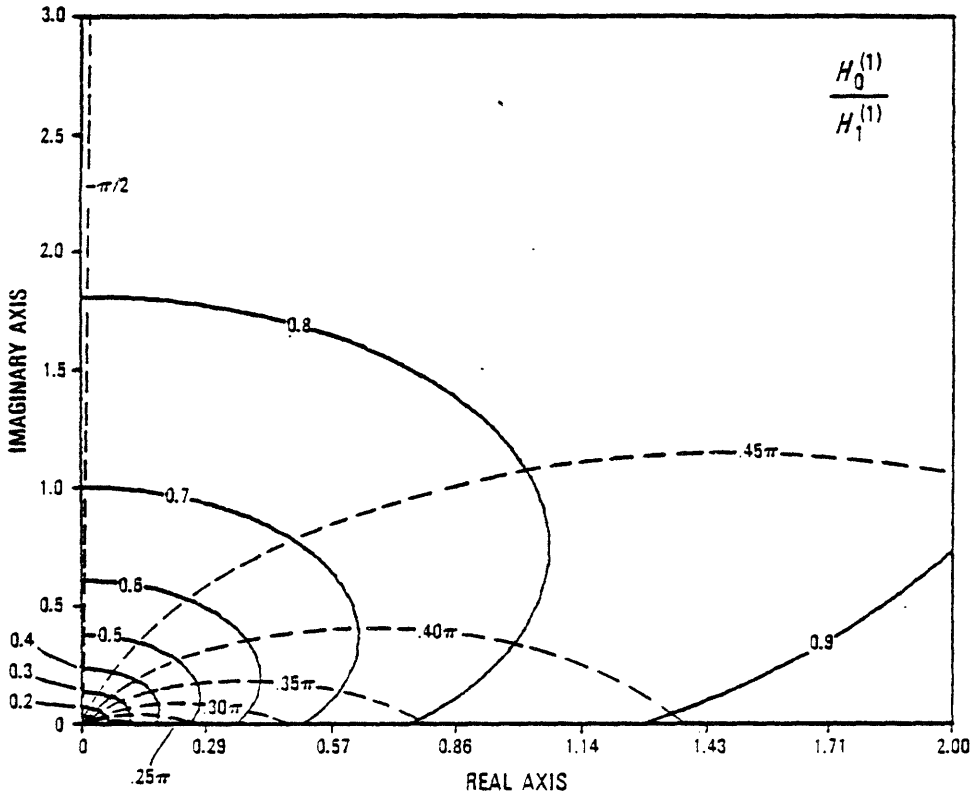

Figure 4-3. Magnitude and phase of the $H_0^{(1)}/H_1^{(1)}$ impedance related ratio

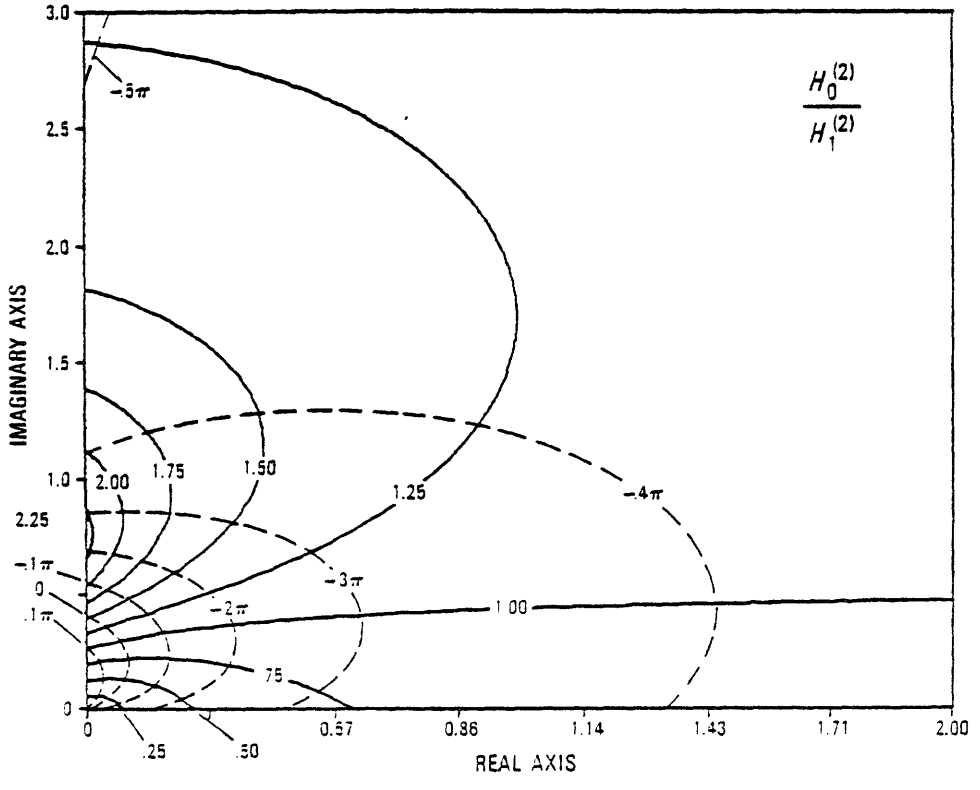

Figure 4-4. Magnitude and phase of the $H_0^{(2)}/H_1^{(2)}$ impedance related ratio

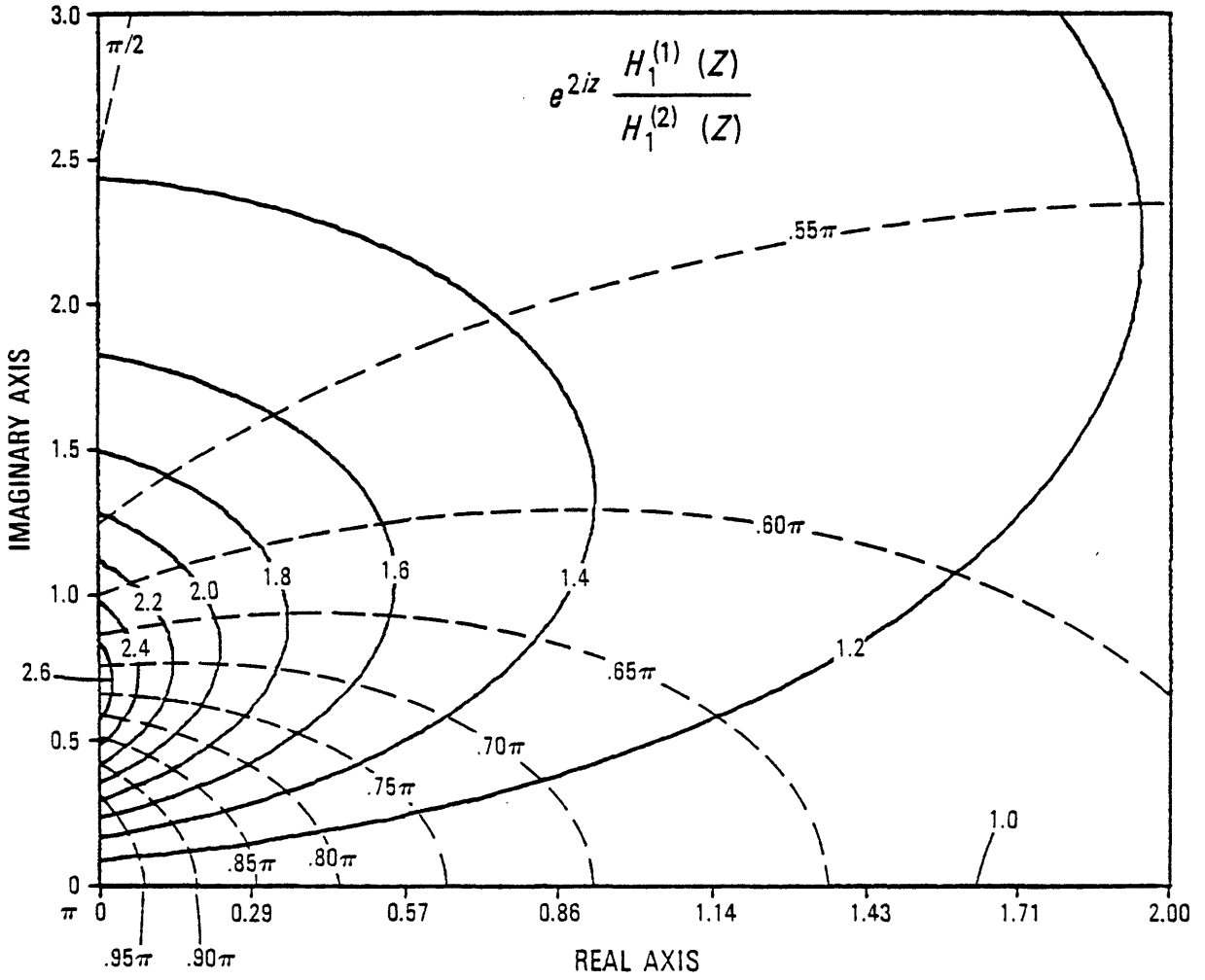

Figure 4-5. The magnitude and phase of the demodulated phase shift ratio

sampled each ratio in a rectangular region in the first quadrant, rather than just near the real and imaginary axes, and have used a bilinear interpolator.

Because the variation of the functions in Figures 4-3, 4-4 and 4-5 is most rapid for small arguments and is quite slow for large arguments, we have sampled each ratio on a Gaussian grid, defined by the points $Z[m,n]$, where

$$Z[m,n] = \left\{ e^{c_M m^2} - 1 \right\} + i \left\{ e^{c_N n^2} - 1 \right\} \qquad \begin{matrix} m = 0,1,\ldots,M-1 \\ n = 0,1,\ldots,N-1 \end{matrix} \tag{4.15}$$

In this way, the sampling is dense near the origin and sparse away from the origin. For a given

number of samples in the real-axis direction, M, the parameter c_M will determine the extent of the table. Similar comments apply to N and c_N in the imaginary-axis direction. The use of the Gaussian grid, instead of, say, an exponential grid, has been found to distribute the relative error associated with the table scheme more evenly throughout the domain of the table.

We have found that, with $M = N = 80$ and $Z[79,79] = (20,8)$, the maximum relative error in the table lookup and interpolation scheme for each of the ratios is strictly less than .5% throughout the domain of the table and is almost always much less than .1%. More precisely, for the $H_0^{(1)}/H_1^{(1)}$ ratio, the relative error becomes larger than .1% only for arguments with magnitude less than 1/10. This is consistent with Figure 4-3 which shows the most rapid variation of this ratio in this region. However the arguments are rarely this small, so that a larger relative error in this unlikely region is acceptable.

In a similar manner, the $H_0^{(2)}/H_1^{(2)}$ ratio has a relative error which is always less than .1% except near the origin and in the region along the imaginary axis in Figure 4-4 where the ratio varies more rapidly. Along the imaginary axis, the relative error never exceeds .3%, and as with the Ψ_1 ratio, if the argument has a magnitude less than .1 then a relative error larger than .1% but less than .5% will result.

In the case of the phase shift ratio, Φ, the relative error is less than .22% everywhere. The maximum error occurs along the imaginary axis where, from Figure 4-5, this function varies most rapidly.

4.3.2 The Cylindrically Layered Fluid Formation Model

In this section, we present an efficient method for the evaluation of the impedance of a formation which consists of concentric annular fluid layers. Such a formation model is shown in Figure 4-6. We do this by computing both the pressure and radial velocity of the formation, evaluated at $r=a$, and taking the ratio of the two. The cylindrical wave reflection coefficient for such a formation is then given by (4.3) with this value of z^{form}.

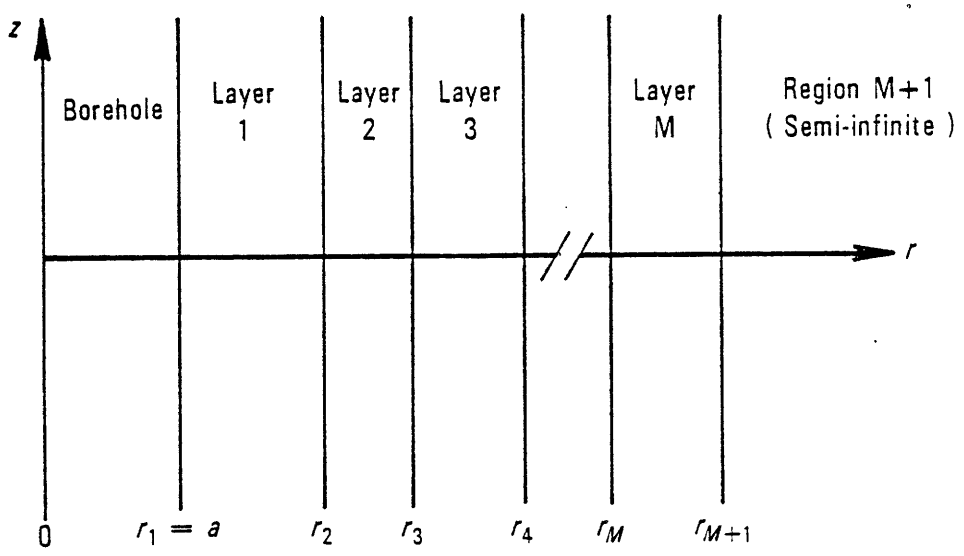

Figure 4-6. The cylindrically layered liquid formation geometry

As discussed in Chapter III, in a fluid medium, the pressure, p, and the radial component of velocity, v_r, are each related to the displacement potential, ϕ, of the medium by the relations (equation (3.6))

$$p = \omega^2 \rho \phi \qquad v_r = -i\omega \frac{\partial \phi}{\partial r} \tag{4.16}$$

Recognizing that the potential in the $n-th$ layer will be of the form

$$\phi_n(r) = A_n^+ H_0^{(1)}(k_r^{(n)} r) + A_n^- H_0^{(2)}(k_r^{(n)} r) \tag{4.17}$$

where $k_r^{(n)}$ is the radial wavenumber in the $n-th$ layer, given by $k_n^2 = k_r^{(n)2} + k_z^2$ with $k_n = \omega / v_n$. The pressure and radial velocity in the $n-th$ layer is then given by

$$\begin{bmatrix} p(r) \\ v_r(r) \end{bmatrix} = \Phi_n(r) \begin{bmatrix} A_n^+ \\ A_n^- \end{bmatrix} \qquad r_n \leq r \leq r_{n+1} \tag{4.18}$$

where

$$\Phi_n(r) = \omega \begin{bmatrix} \omega\rho_n H_0^{(1)}(k_r^{(n)} r) & \omega\rho_n H_0^{(2)}(k_r^{(n)} r) \\ ik_r^{(n)} H_1^{(1)}(k_r^{(n)} r) & ik_r^{(n)} H_1^{(2)}(k_r^{(n)} r) \end{bmatrix} \tag{4.19}$$

Because both pressure and radial velocity are continuous across a fluid/fluid interface, and since the potential in the $n-th$ layer is valid from $r=r_n$ to $r=r_{n+1}$, then we may write that

$$\begin{bmatrix} A_n^+ \\ A_n^- \end{bmatrix} = \Phi_n^{-1}(r_n) \begin{bmatrix} p(r_n) \\ v_r(r_n) \end{bmatrix} = \Phi_n^{-1}(r_{n+1}) \begin{bmatrix} p(r_{n+1}) \\ v_r(r_{n+1}) \end{bmatrix} \tag{4.20}$$

therefore

$$\begin{bmatrix} p(r_n) \\ v_r(r_n) \end{bmatrix} = \Phi_n(r_n)\, \Phi_n^{-1}(r_{n+1}) \begin{bmatrix} p(r_{n+1}) \\ v_r(r_{n+1}) \end{bmatrix} \tag{4.21}$$

If we now define a new matrix, Ψ_n, as

$$\Psi_n = \Phi_n(r_n)\, \Phi_n^{-1}(r_{n+1}) \tag{4.22}$$

then the pressure and radial velocity ar $r=r_1$ can be expressed in terms of the pressure and radial velocity in the outermost region as follows

$$\begin{bmatrix} p(r_1) \\ v_r(r_1) \end{bmatrix} = \left\{ \prod_{n=1}^{M} \Psi_n \right\} \begin{bmatrix} p(r_{M+1}) \\ v_r(r_{M+1}) \end{bmatrix} \tag{4.23}$$

Since region $M+1$ is semi-infinite, its pressure and radial velocity are of the form given by equation (4.16). Therefore, equation (4.23) dictates how to compute the total pressure and radial velocity at $r=r_1=a$.

The usefulness of this formulation depends upon the speed at which we can compute a particular Ψ_n. It follows directly from (4.19) and (4.22) that Ψ_n is given by

$$\Psi_n = -i \frac{\pi}{4} k_r^{(n)} r_{n+1} \begin{bmatrix} \Omega(r_n, r_{n+1}) & \beta \Lambda_0(r_n, r_{n+1}) \\ -\beta^{-1} \Lambda_1(r_n, r_{n+1}) & \Omega(r_{n+1}, r_n) \end{bmatrix} \tag{4.24}$$

where

$$\Omega(r_n, r_{n+1}) = H_0^{(1)}(k_r^{(n)} r_n) H_1^{(2)}(k_r^{(n)} r_{n+1}) - H_0^{(2)}(k_r^{(n)} r_n) H_1^{(1)}(k_r^{(n)} r_{n+1}) \tag{4.25}$$

and

$$\Lambda_\nu(r_n, r_{n+1}) = H_\nu^{(2)}(k_r^{(n)} r_n) H_\nu^{(1)}(k_r^{(n)} r_{n+1}) - H_\nu^{(1)}(k_r^{(n)} r_n) H_\nu^{(2)}(k_r^{(n)} r_{n+1}) \tag{4.26}$$

with

$$\beta = -i \frac{\omega \rho_n}{k_r^{(n)}} \tag{4.27}$$

From this result, we see that we need to compute the zero-th and first order Hankel functions of the first and second type at each interface. Because these functions are well behaved everywhere except at the origin, efficient table-based methods can presumably be developed for their rapid evaluation away from the origin and a small argument asymptotic expansion can be used near the origin. The pressure and radial velocity at $r=a$ can then be quickly computed since only M 2-by-2 matrix multiplies are required. The formation impedance is the ratio of these two quantities. Finally, this is used in (4.4) to compute the cylindrical wave reflection coefficient. This approach for the evaluation of the modal coefficient associated with a layered fluid formation has yet to be implemented.

4.3.3 The Cylindrically Layered Solid Formation Model

The theoretical expression for $R(k_z, \omega)$ when the formation is a layered solid, is not presented here. The interested reader can find the relevant equations in the paper by Schoenberg, et.al. [33]. We briefly describe what is involved.

A compressional and shear potential are required in each solid layer. Each potential has

two unknown amplitudes, as in equation (4.17), so that there are a total of four unknowns in each layer. If we include the two unknowns in the outermost half-space and the one unknown in the borehole, there are $4M+3$ unknowns in the geometry. Boundary conditions at a solid/solid interface relate the unknowns in one medium to those in the adjacent medium. A propagator matrix solution, analogous to that developed for the layered fluid formation, can be constructed where the matrices are 4-by-4 instead of 2-by-2. Alternatively, one can solve a banded set of $4M+3$ linear equations in $4M+3$ unknowns. The major added difficulty with the solid layered formation, relative to the liquid layered formation, is in the larger number of Hankel function evaluations required

4.4 Parametric Source Models

4.4.1 The Temporal Response

The source pressure waveform, $s(t)$, must be bandlimited so that the infinite limits on the frequency transform can be truncated and the discrete Fourier transform can be used. However, in addition to this, the source waveform must have a Fourier transform, $S(\omega)$, which goes to zero at zero frequency at least as fast as ω^2. That is

$$\lim_{\omega \to 0} S(\omega) \sim \omega^n \qquad \text{where } n \geq 2 \tag{4.28}$$

This low frequency constraint in effect implies that a bandpass source must be used.

The reason for this low frequency constraint is perhaps best explained via the relationship between pressure and displacement. Mathematically, the displacement field, denoted $\underline{u} = u_r \hat{i}_r + u_z \hat{i}_z$, is related to pressure via the relation [14]

$$\underline{u} = \frac{1}{\omega^2 \rho} \left\{ \frac{\partial p}{\partial r} \hat{i}_r + \frac{\partial p}{\partial z} \hat{i}_z \right\} \tag{4.29}$$

Here we see from the ω^{-2} dependence that the pressure field must be integrated twice in time to obtain the associated displacement field. This means that, by specifying an arbitrary pressure field, the corresponding displacement field may be non-physical. To see this, suppose that the pressure field is temporally impulsive. The displacement field, then, will be ramp-like, implying that it monotonically increases in amplitude with time. That is, there is a steady flow, or current, in the fluid.

We define a physically meaningful displacement signal as one that has a final value of zero. This means that, long after the source activates, the particles in the medium return to their rest position, or equivalently, the acoustic field we measure is a perturbation of the ambient field. Using the properties of the Fourier transform, this implies that the transform of the displacement field must be asymptotic to ω^n as $\omega \rightarrow 0$ where $n \geq 0$. From this result, equation (4.28) follows immediately.

This low frequency constraint on the pressure waveform was overlooked by both Tsang and Cheng. They used a source pulse whose transform was asymptotic to a non-zero constant at zero frequency. We have found that, by using this source waveform, the synthetic waveforms do not go to zero as time gets large. Rather, they tend to a constant non-zero final value. The synthetic waveforms presented by Tsang were not plotted out far enough in time to see this behavior, while in Chengs paper, the waveforms were presumably post-filtered to remove this effect.

Physically, the final value to the waveforms is due to the Stoneley mode of propagation in the borehole. This mode does not have a cutoff frequency, and thus propagates down to zero frequency [33]. Furthermore, the residue of the Stoneley pole of the modal coefficient has been examined [27] and found to behave roughly as $1/\omega$. Therefore, the Stoneley wave component of a synthetic waveform is shaped much like the integral of the source pulse. Consequently, a final value to the Stoneley wave will result if the integral of the source pulse has a non-zero final value. Such was the case with the waveform used by both Tsang and Cheng.

The observation concerning the relationship between displacement and pressure suggests that it may be more useful to design the displacement waveform corresponding to the physical movement of the source. Then, the pressure waveform is obtained by taking two derivatives of this waveform. In Figure 4-7 we plot a 4-point optimal Blackman window function, corresponding to a bump-like displacement waveform, and its second derivative, corresponding to the associated pressure signal. It is interesting to note the similarity between the second derivative of the window and the classical Ricker wavelet often used in seismology [30]. Also shown in Figure 4-7 are the magnitudes of the Fourier transforms of these pulses. Mathematically, the pulses and their transforms are given by

$$b(t) = \begin{cases} \sum_{n=0}^{3} b_n \cos\left\{\frac{2\pi nt}{T}\right\} & 0 \le t \le T \\ 0 & \text{otherwise} \end{cases} \tag{4-30}$$

$$B(\omega) = \left\{2\omega \sin(\omega T/2)\, e^{j\omega T/2}\right\}\left\{\sum_{n=0}^{3} \frac{b_n}{\omega^2 - (2\pi n/T)^2}\right\} \tag{4-31}$$

$$\ddot{b}(t) = \begin{cases} \sum_{n=1}^{3} -b_n\left\{\frac{2\pi n}{T}\right\}^2 \cos\left\{\frac{2\pi nt}{T}\right\} & 0 \le t \le T \\ 0 & \text{otherwise} \end{cases} \tag{4-32}$$

$$\ddot{B}(\omega) = \left\{-2\omega \sin(\omega T/2)\, e^{j\omega T/2}\right\}\left\{\sum_{n=1}^{3} \frac{b_n\,(2\pi n/T)^2}{\omega^2 - (2\pi n/T)^2}\right\} \tag{4-33}$$

where $b(t)$ is used to denote the Blackman window function and $\ddot{b}(t)$ denotes its second derivative. The b_n constants are given by b_0=+.35869, b_1=−.48829, b_2=+.14128 and b_3=−.01168. Also, in evaluating the transforms above at $\omega = 0$ we use the relations $B(0)=b_0T$ and $\ddot{B}(0)=0$.

Note from Figure 4-7 that the transform of the Blackman window is down 92dB at a frequency of 4/T Hertz while its second derivative is down 67dB at this point. Thus, besides

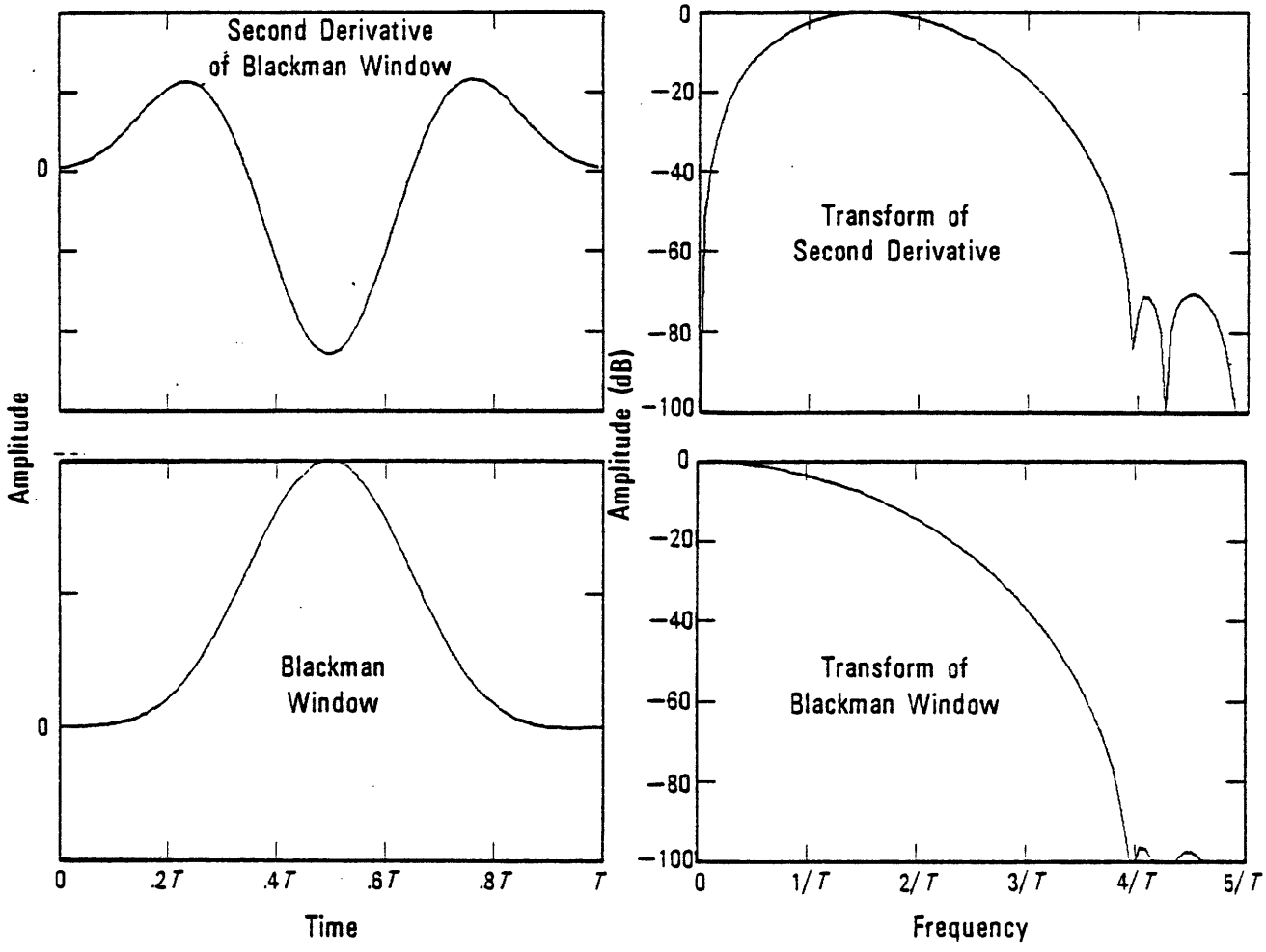

Figure 4-7. The blackman window function, its 2nd derivative and their transforms

being ideally time-limited signals, these pulses are also effectively bandlimited. Furthermore, the transform of the second derivative of the Blackman pulse is seen to satisfy the constraint in equation (18). For these reasons, the signal $\ddot{b}(t)$ is an attractive choice for a source pulse model.

A possible drawback to the choice of a $\ddot{b}(t)$ source pulse is that there is no independent control of both bandwidth and center frequency. If such control is desired, the second derivative of the Tsang-type pulse has been found to work well, as has a modulated version of the

Blackman pulse.

4.4.2 The Spatial Distribution

The source filament distribution, $d(z)$, can be designed in conjunction with the source pulse to selectively excite, or not excite, a desired rectangular region in the frequency-wavenumber domain. In this way, one has more control over the excitation of modes and/or headwaves in the synthetic data than if a point source were used. Conventional linear phase FIR filter design techniques can be used to design the source array from wavenumber domain stop-band and pass-band specifications. Alternatively, if a normal incidence beam is desired, a Blackman window function design can be used here as well.

4.5 Representative Examples

In this section, we present examples of arrays of synthetic waveforms associated with an infinite homogeneous solid formation model. We use the table lookup and interpolation method described in Section 4.3.1 and compare the computation time required to generate these examples with that required to generate the same examples, only a Hankel function evaluation method was used to evaluate the required ratios rather than the table method. By over riding the table in this manner, a test of the savings in computation time can be made.

In Figure 4-8 we show 3 waveforms, selected from an array of 100, which were generated using the table-based method. In Figure 4-9 we show a VDL (variable density log) of the entire 100 waveforms. The source used was a 2^{nd} derivative of a Blackman window, 100μs in duration, and was spatially impulsive (i.e. a point source). The waveforms begin at zero offset from the source and the distance between receivers is 1 inch. The borehole radius was taken to be 10cm and the density ratio, ρ_1/ρ, was taken to be 2. The velocities were all taken as real-valued and are given by v_f = 1.5 Km/s, v_s = 2 Km/s and v_c = 3.5 Km/s. Note how, at small offsets, the individual reflections off the borehole wall are well resolved, while at the distant receivers, the modal energy dominates the waveforms.

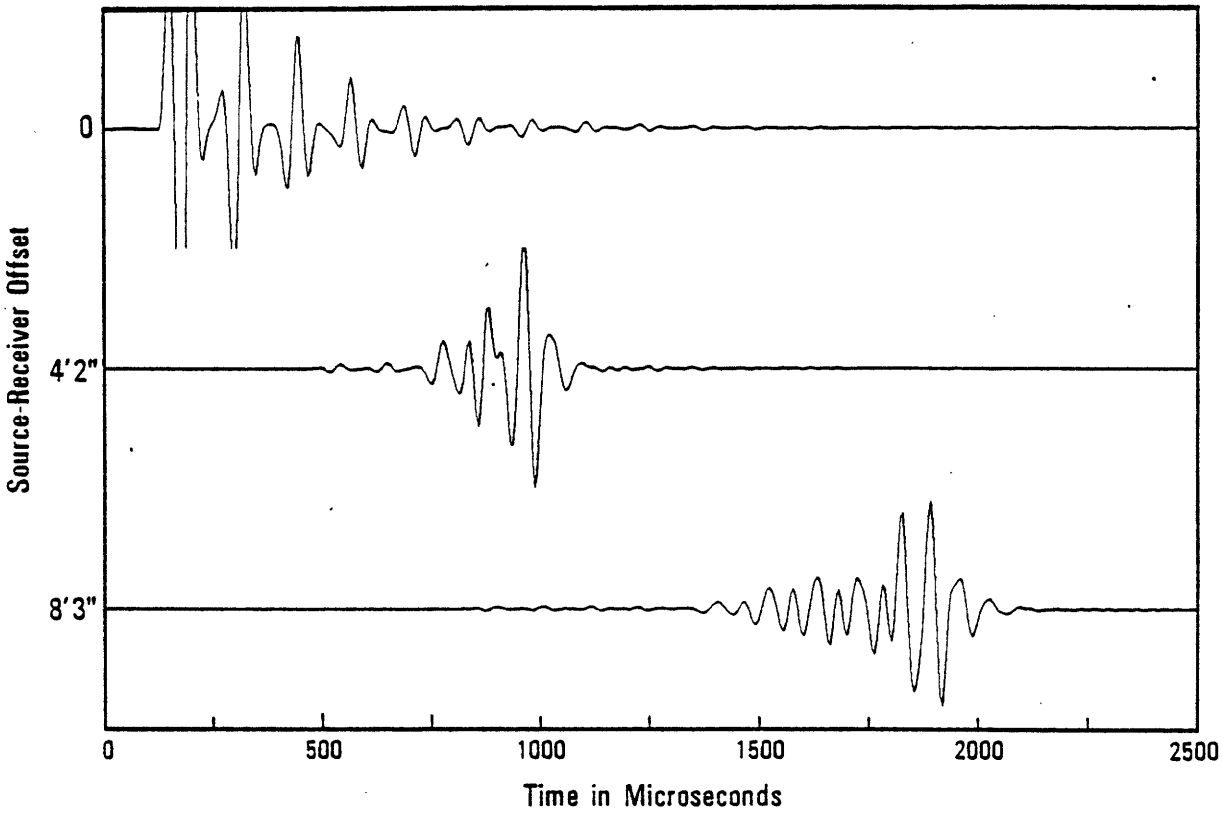

Figure 4-8. 3 synthetic waveforms selected from an array of 100

These waveforms were generated on a VAX machine with a VMS operating system and the programming was done in FORTRAN using single precision floating point arithmetic. Precisely 2489945 evaluations of the modal coefficient were required to generate this data. Using the table-based method, 2.72 hours of computation time was required, implying an average of 254 evaluations of $A(k_z, \omega)$ per second, or 3.93 ms per evaluation.

To determine the savings in computation time associated with the table method, we generated the same synthetic data set, only instead of using the table for the evaluation of the Hankel function ratios, a direct algorithmic approach was used in its place. Unfortunately, the algorithmic approach was more accurate than the table lookup method, so that the comparison in computation time was not fair and therefore, not particularly meaningful. Nevertheless, we found that, for the same number of evaluations, 33 hours and 22 minutes of computation time

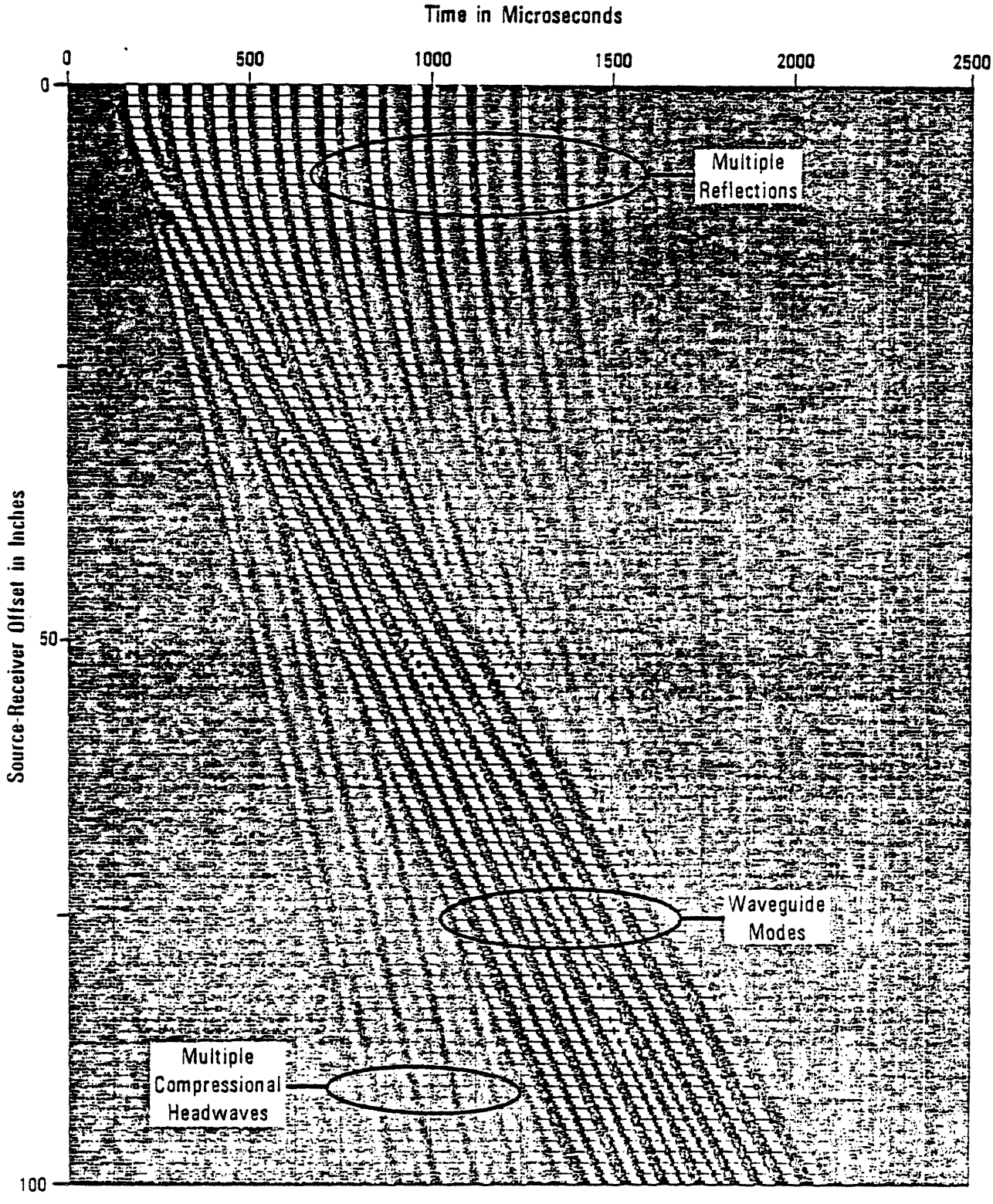

Figure 4-9. A variable density log (VDL) of the entire 100 waveforms

was required, implying 21 evaluations per second or 48ms per evaluation. We conclude that the use of the table lookup and interpolation approach produces roughly an order of magnitude savings in computation time. Because only three complex-valued 80-by-80 tables must be stored, the added storage is well worth the savings in time.

In Figure 4-10 we show three synthetic waveforms for the same set of parameters as in Figure 4-8, except that a source filament was used instead of a point source. The distribution of the source was taken to be a Blackman window function with a half-length of 15cm. The use of this array forms a beam at normal incidence to the formation. The effect of array is to low-pass filter the data in the spatial direction. Note that the higher frequency modal energy in the distant waveforms has disappeared, while the lower frequency Stoneley mode has been smeared out in time.

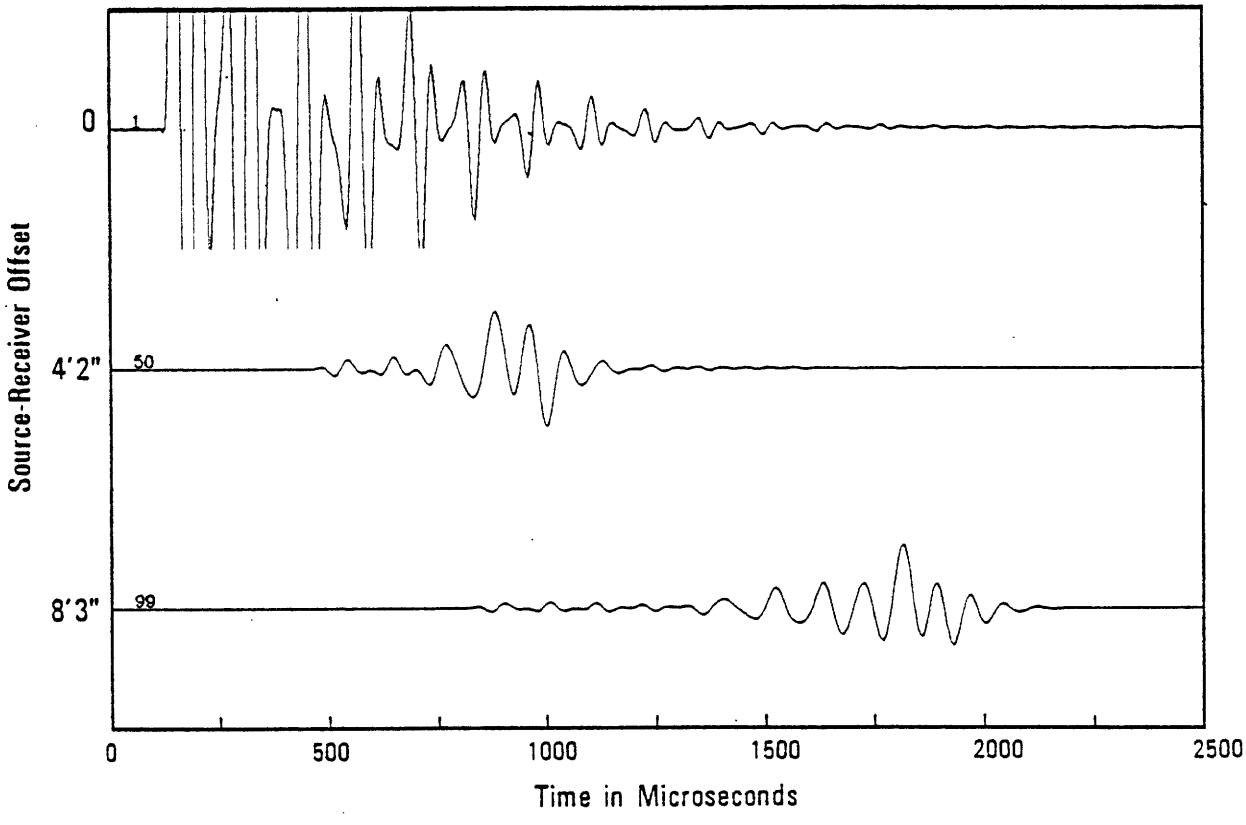

Figure 4-10. 3 synthetic waveforms associated with a filament source

4.8 Summary

In summary, we have found that the repeated evaluation of Hankel functions for complex-valued arguments is responsible for the majority of computation time required to generate synthetic acoustic well logging data. Through an understanding of wave propagation in cylindrical geometries, a table lookup and interpolation scheme for the rapid and accurate evaluation of the Hankel functions has been developed which results in an order of magnitude savings in the computation time required to generate the data. The storage requirements for the table are easily outweighed by this savings.

Since the development of this table based method, table-based approaches have been developed for the case of a cylindrically layered formation [7][8] and, with the increase in speed reported here, the previously prohibitive analysis-by-synthesis approach to data inversion may now be feasible in a cylindrical geometry.

In the area of future improvements, it appears that a further substantial savings can be had by sampling the modal coefficient on an irregular grid. At present, the uniform grid sampling periods are chosen small enough to capture the most rapid variation in the modal coefficient. By sampling the coefficient frequently only where it varies rapidly, and slowly where it varies slowly, a large savings may result. A possible detraction of this approach is that the irregular grid will have to be interpolated onto a regular grid if the efficient FFT algorithm is to be used.

V. ITERATIVE MAXIMUM LIKELIHOOD DEREVERBERATION

5.1 Introduction

In this chapter we take the relationship derived in Chapter III between the reflected component of the field on the axis of the hole and the cylindrical wave reflection coefficient and extract three signal processing models from it. The first is a two dimensional space-time signal model while the other two are one dimensional signal models corresponding to single frequency data as a function of space and single wavenumber data as a function of time. All three models are seen to share a common structure, that of a reverberatory system, although the details of the models differ. We select one of these models, the single wavenumber model, for thorough investigation in this and the next chapter, while the other two are left for possible future examination.

The estimation of the reflection coefficient at a single axial wavenumber is seen to be a signal processing problem of dereverberation, or equivalently, of removing multiples. We begin by parametrically modeling the Fourier transform of the reflection coefficient by a finite number of its samples and, in this way, the reflection coefficient estimation problem is reduced to a problem in parameter estimation. Uncertainties in the form of additive Gaussian noise processes are then added to the processing model and a maximum likelihood (ML) estimation criterion is adopted [39]. We find that the estimation problem is nonlinear in that a highly complicated function of the parameters of interest must be maximized. We conclude from this that the ML problem is difficult to solve.

Following this, we develop an iterative method for solving the ML dereverberation problem which is both theoretically elegant and computationally efficient. In effect, the estimation system is augmented by the introduction of an internal signal into the problem formulation. This auxiliary signal effectively decouples the original nonlinear problem into two interconnected linear estimation problems. Specifically, within each pass of the iterative method,

a "classical" linear filtering problem must first be solved, and then a linear "classical" system identification problem must be solved. At the end of each iterative pass a new estimate for the reflection coefficient parameters is put forth. The log likelihood function evaluated at this new estimate is theoretically guaranteed to be greater than the log likelihood estimate evaluated at the last estimate however the sequence of estimates produced by this iterative method is not guaranteed to converge.

The iterative ML dereverberation method developed in this chapter arose directly from the iterative ML theory developed by Musicus [23]. He applied the theory to estimate the coefficients of a pole-zero model where the noise processes were jointly Gaussian, as they are here. We show that the dereverberation problem is closely related to the pole-zero estimation problem and in fact, the dereverberation problem is equivalent to a pole-zero estimation problem in which the numerator and denominator polynomial coefficients are linearly related. In this sense, the dereverberation problem can be viewed as a constrained pole-zero problem.

In Chapter VI, we will apply the iterative ML dereverberation method developed in this chapter to the single wavenumber signal processing model we have chosen to investigate. There, we make use of synthetic data generated using the method described in Chapter IV to test and evaluate the ML estimation scheme we develop here.

5.2 Processing Models

The study in Chapter III of the relationship between the cylindrical wave reflection coefficient, $R(k_z,\omega)$, and the reflected component of the acoustic field along the axis of the borehole, $p_r(z,t)$, resulted in equation (3.48), which we repeat here

$$p_r(z,t) = \frac{1}{(2\pi)^2}\int_{-\infty}^{\infty}\int_{-\infty}^{\infty}\left\{H(\omega)\,S(\omega)\,D(k_z)\sum_{m=1}^{\infty}R^m(k_z,\omega)\right\}e^{-i\omega t}e^{ik_z z}\,dk_z\,d\omega \tag{5.1}$$

To review, $S(\omega)$ is the Fourier transform of the source waveform, $D(k_z)$ is the transform of the

source distribution, and $H(\omega) = 2\pi i\,\mathrm{sgn}(\omega)$. The Fourier transform of $H(\omega)$ is given by $h(t) = 2/t$ [26].

We see from (5.1) that the relationship between the reflection coefficient and the field is directly interpretable in terms of 2D space-time invariant convolutions. Specifically, denoting the 2D transform of the reflection coefficient as $r(z,t)$, and referring to it as the reflection coefficient signal, we may write as we did in equation (3.49), that

$$p_r(z,t) = s_h(t)\ d(z) ** \left\{ r(z,t) + r(z,t) ** r(z,t) + \cdots \right\} \tag{5.2}$$

where the two asterisks denote 2D convolution and $s_h(t)$ denotes the convolution of $s(t)$ with $h(t)$. This 2D linear system can be cast into feedback form as shown in Figure 5-1. We refer to the system in Figure 5-1 as the "2D system model".

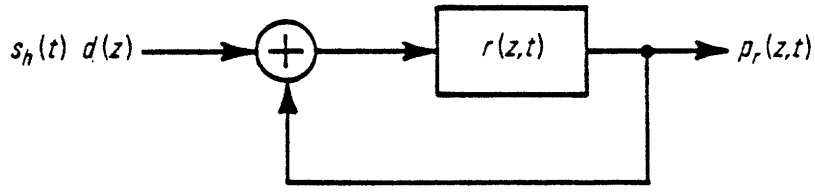

Figure 5-1. The 2D system model

Besides the 2D model, equation (5.1) immediately suggests two 1D models which are obtained when either the transform of the source pulse or the transform of the source distribution is impulsive. We consider these two cases separately below.

5.2.1 The Single Frequency Model

If a single frequency source is used, i.e. if $S(\omega) = 2\pi S_o \delta(\omega - \omega_o)$, then we see from

equation (5.1) that the system becomes one-dimensional. Specifically, denoting the Fourier transform of $R(k_z, \omega)$ over k_z as $r(z \mid \omega)$ (or equivalently, the Fourier transform of $r(z,t)$ over time), then we may write (supressing the $e^{-i\omega_0 t}$ time dependence)

$$p_r(z \mid \omega_0) = \left\{ H(\omega_0)\ S_0 \right\} d(z) * \left\{ r(z \mid \omega_0) + r(z \mid \omega_0) * r(z \mid \omega_0) + \cdots \right\} \tag{5.3}$$

where the asterisk denotes 1D spatial convolution and $p_r(z \mid \omega_0)$ denotes the reflected component of the field at a single frequency, ω_0. This same 1D system model can be obtained using a transient source by transforming $p_r(z,t)$ over time and evaluating the result at the desired frequency. As before, equation (5.3) can be cast into a feedback form as shown in Figure 5-2. We refer to this system as the "single frequency system model". In this system, we will only be able to estimate a slice of the reflection coefficient as a function of axial wavenumber for a fixed frequency.

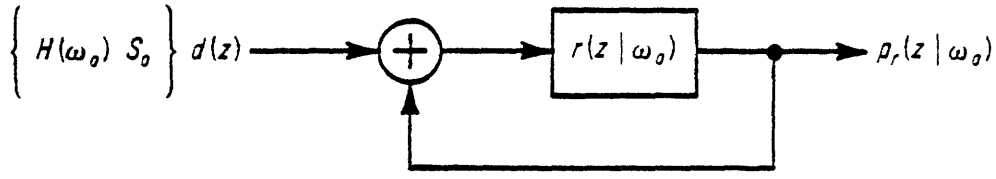

Figure 5-2. The 1D single frequency system model

5.2.2 The Single Wavenumber Model

If, in equation (5.1), a line source is used whose spatial transform is given by $D(k_z) = 2\pi D_0 \delta(k_z - k_{z0})$, then we see that the system also becomes one dimensional. Specifically, denoting the Fourier transform of the reflection coefficient over k_z as $r(t \mid k_z)$ (or equivalently, the Fourier transform of $r(z,t)$ over z), then we may write (supressing the $e^{ik_{z0}z}$

space dependence)

$$p_r(t \mid k_{z0}) = D_o \; s_h(t) * \left\{ r(t \mid k_{z0}) + r(t \mid k_{z0}) * r(t \mid k_{z0}) + \cdots \right\} \tag{5.4}$$

where a single asterisk here denotes 1D temporal convolution and $p_r(t \mid k_{z0})$ denotes the reflected component of the field at a single axial wavenumber. This same 1D system model can be obtained using a point source, or more generally, using an arbitrary linear source array, by transforming $p_r(z,t)$ over space and evaluating the result at the desired axial wavenumber, k_{z0}. As before, equation (5.4) can be cast into the form of a reverberatory system as shown in Figure 5-3. We refer to this system as the "single wavenumber system model" and we will discuss the estimation problem associated with this model in considerable detail in this and the next chapter. In this system, one can only estimate the reflection coefficient as a function of frequency for a fixed axial component of wavenumber. In Chapter II we demonstrated the sensitivity of such a slice of the reflection coefficient to the parameters of the formation in the particular case where the formation model was homogeneous.

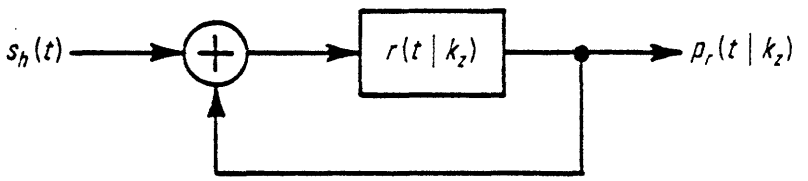

Figure 5-3. The 1D single wavenumber system model

5.3 Parametric Signal Representation

To this point, we have treated the reflection coefficient as a continuous function of both frequency and wavenumber and its Fourier transform as a continuous space-time signal. In this

section, we discuss the representation of the reflection coefficient and its transform by a finite number of parameters. This is achieved via a parametric model for the reflection coefficient and the estimation approach, then, will be to estimate the model parameters rather than the continuous function itself. The estimate of the reflection coefficient can be obtained by substituting the parameter estimates into the signal model. Using this approach, the reflection coefficient estimation problem reduces to a parameter estimation problem.

Classical approaches to representing a continuous signal by a set of parameters include the Karhunen-Loeve expansion, a Gram-Schmidt representation, etc. [39]. Although theoretically elegant, these approaches can be somewhat cumbersome primarily because the parameters themselves will not generally be physically meaningful and because a large number of parameters may be required to adequately represent the signal.

A more natural approach in this application is to first represent the continuous signals considered to this point by their sampled, or discretized, counterparts. The switch to the discrete space-time domain is convenient because the data will typically be both recorded and processed using digital means. Following this, the discrete signals can then be modeled parametrically using, for example, a pole-zero (i.e. an autoregressive moving-average, or ARMA) representation in the z-transform domain [25]. Pole-zero models, or less generally, all-pole (i.e. autoregressive, or AR) or all-zero (i.e. moving-average, or MA) models, are used extensively in the fields of modern spectral estimation [17], speech processing [22], etc. In this thesis, we will also adopt a pole-zero modeling approach.

To distinguish discrete signals from continuous signals, we will use square brackets, as in $s[n]$, rather than rounded brackets, as in $s(t)$. Generally, n will be used as a discrete time index and m will be used to index discrete space. For example, samples of the reflection coefficient signal in the single wavenumber model, $r(t \mid k_z)$, will be denoted by $r[n]$, where the dependence on k_z is understood. Similarly, in the single frequency model, we denote the samples of $r(z \mid \omega)$ by $r[m]$. Sampled versions of other continuous signals are defined similarly.

A pole-zero model for the single wavenumber reflection coefficient sequence, $r[n]$, is defined in terms of the z-transform of the reflection coefficient sequence as follows

$$R[z] = \sum_{n=0}^{\infty} r[n]\, z^{-n} = \frac{\sum_{m=0}^{P} a_m\, z^{-m}}{1 + \sum_{m=1}^{Q} b_m\, z^{-m}} = \frac{A_P[z]}{1 + B_Q[z]} \tag{5.5}$$

Here we have modeled $r[n]$ as a causal sequence. The $P+1$ coefficients in the numerator polynomial and the Q coefficients in the denominator polynomial define a set of $P+Q+1$ parameters which can be used to characterize the $r[n]$ sequence.

It is instructive to examine the form of the model for the closed-loop system when the reflection coefficient model is pole-zero. The closed-loop system z-transform, $A[z]$, is related to $R[z]$ by the relation $A = R/(1 - R)$. Using (5.5), we see that

$$A[z] = \frac{A_P[z]}{1 + B_Q[z] - A_P[z]} \tag{5.6}$$

From this result we see that a pole-zero model for R generally implies a pole-zero model for the closed-loop system. However, in the special case where R is all-pole, defined by the condition $P = 0$ in (5.5), we see that A_P reduces to a constant, a_0, and $A[z]$ also becomes all-pole. If, on the other hand, the reflection coefficient is modeled as all-zero, defined by the condition $B_Q[z] = 0$, then we see that $A[z]$ is pole-zero with a numerator polynomial given by A_P and a denominator polynomial given by $1 - A_P$. Thus, in this case, knowledge of the poles implies knowledge of the zeros and vice versa. We conclude that when R is modeled as all-zero, the overall system is a constrained pole-zero system in which the poles and zeros are tied to each other.

5.4 Maximum Likelihood Estimation

The maximum likelihood (ML) estimation problem is to maximize the conditional

probability density function (PDF) of the data given the reflection coefficient parameters over the space of admissible reflection coefficient parameter sets [39]. This space consists of those sets which map into reflection coefficients which are less than unity in magnitude for all frequencies and wavenumbers. The particular parameter set which maximizes the PDF is, in some sense, "most likely" to have caused the observations that were made, and hence, is termed the maximum likelihood estimate of the parameters. Mathematically, collecting the reflection coefficient parameter set into a vector, $\underline{r}$, and the observations (i.e. the data samples) into a vector $\underline{y}$, the ML estimator is defined by the relation

$$\hat{\underline{r}}_{ML} = \max_{\underline{r}} \left\{ \log p(\underline{y} \mid \underline{r}) \right\} \tag{5.7}$$

where $p(\underline{y} \mid \underline{r})$ denotes the conditional joint PDF of the data given the reflection coefficient parameters and $\log p(\underline{y} \mid \underline{r})$ is referred to as the log likelihood function. Maximizing the log of the PDF in (5.7) is equivalent to maximizing the PDF itself, since the log function is monotonic. Furthermore, in the specific case where the PDF is Gaussian, maximizing the log likelihood function sometimes involves only maximizing a quadratic function and therefore requires only linear processing.

Because ML estimation can be attractive when the processes involved are jointly Gaussian, and because the Gaussian case will be assumed in this thesis, we explore Gaussian ML problems in more detail in the remainder of this section. Of particular interest are the conditions under which the Gaussian ML estimation problem is a linear estimation problem.

5.4.1 Gaussian ML Problems

If the conditional joint PDF of the data given the parameters is Gaussian, then it can be written in the following form

$$p(\underline{y}\,|\,\underline{r}) = \frac{1}{(2\pi)^{N/2}\,|\Sigma_{y|r}|^{1/2}} \exp\left\{-\frac{1}{2}\left\{[\underline{y}-\underline{m}_{y|r}]^T\,\Sigma_{y|r}^{-1}\,[\underline{y}-\underline{m}_{y|r}]\right\}\right\} \tag{5.8}$$

where N is the length of the $\underline{y}$ vector and $\underline{m}_{y|r}$ and $\Sigma_{y|r}$ are the conditional mean and covariance of the observations, $\underline{y}$, given the parameters, $\underline{r}$. These are defined by

$$\underline{m}_{y|r} = E_Y\left[\underline{y}\,|\,\underline{r}\right] \quad \text{and} \quad \Sigma_{y|r} = E_Y\left[(\underline{y}-\underline{m}_{y|r})\,(\underline{y}-\underline{m}_{y|r})^T\,|\,\underline{r}\right] \tag{5.9}$$

where the expected value operators are over Y-space, conditioned on $\underline{r}$. We see from (5.8) that, in the particular case of Gaussian processes, the PDF is completely characterized by the first and second order statistics of the process, $\underline{m}_{y|r}$ and $\Sigma_{y|r}$. In fact, this allows us to use the more convenient shorthand notation

$$p(\underline{y}\,|\,\underline{r}) = N(\underline{m}_{y|r}\,,\,\Sigma_{y|r}) \tag{5.10}$$

Here, the N refers to "normal", which is synonomous with Gaussian.

In what follows, it will be convenient to minimize $-2\log p(\underline{y}|\underline{r})$ rather than to maximize $\log p(\underline{y}|\underline{r})$. From equation (5.8), this is given by

$$-2\log p(\underline{y}\,|\,\underline{r}) = N\log(2\pi) + \log|\Sigma_{y|r}| + (\underline{y}-\underline{m}_{y|r})^T\,\Sigma_{y|r}^{-1}\,(\underline{y}-\underline{m}_{y|r}) \tag{5.11}$$

Here we see that, in general, to minimize this function over $\underline{r}$ is a nonlinear problem. The specific functional dependence of equation (5.11) on the parameters, $\underline{r}$, is implicitly contained in the expressions for the conditional mean and covariance for $\underline{y}$ given $\underline{r}$.

A sufficient but stringent condition for the ML estimation problem to be a linear estimation problem is for $\Sigma_{y|r}$ to be independent of the parameters, $\underline{r}$, and for $\underline{m}_{y|r}$ to be a linear function of $\underline{r}$. That is, if $\underline{m}_{y|r} = M\,\underline{r}$, where M is a matrix whose elements are independent of $\underline{r}$. In this way, the ML estimate of $\underline{r}$ is obtained as the solution to a set of linear equations,

$$\underline{y} = \mathbf{M}\,\hat{\underline{r}}_{ML} \tag{5.12}$$

In the next few subsections, we briefly cover the form of the conditional mean and covariance for the Gaussian all-pole, all-zero and pole-zero signal models. We will find it convenient to model the Gaussian process which drives each model as causal. This somewhat unusual type of process is defined as deterministically zero for negative time but stochastic for n greater than or equal to zero. In the process of examining these Gaussian ML problems, we develop an appreciation for their difficult nonlinear nature and in addition, we develop a vector/matrix system notation which will be used in the remainder of this chapter.

5.4.2 The Gaussian All-Pole ML Problem

In Figure 5-4 we show an all-pole linear system driven by a causal Gaussian process, $s[n]$. The observed sequence, $y[n]$, is equal to the system output, $f[n]$, corrupted by an additive Gaussian noise process, $v[n]$, which is independent of $s[n]$. We model the system z-transform as in equation (5.5) with $P=0$ and $a_0 \neq 0$. We now define the following vectors

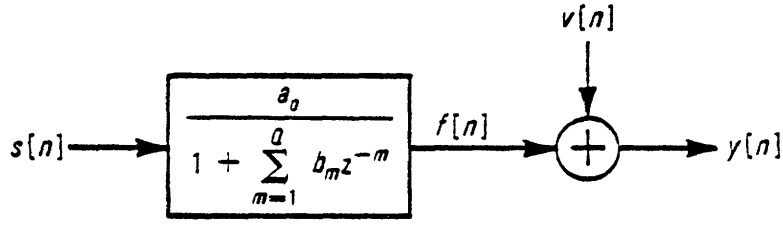

Figure 5-4. The all-pole model

$$\underline{y} = \begin{bmatrix} y[0] \\ y[1] \\ \cdot \\ \cdot \\ y[N-1] \end{bmatrix} \quad \underline{v} = \begin{bmatrix} v[0] \\ v[1] \\ \cdot \\ \cdot \\ v[N-1] \end{bmatrix} \quad \underline{s} = \begin{bmatrix} s[0] \\ s[1] \\ \cdot \\ \cdot \\ s[N-1] \end{bmatrix} \quad \underline{f} = \begin{bmatrix} f[0] \\ f[1] \\ \cdot \\ \cdot \\ f[N-1] \end{bmatrix} \tag{5.13}$$

and the NxN matrix B as

$$\mathbf{B} = \begin{bmatrix} 1 & 0 & & 0 \\ b_1 & 1 & & \cdot \\ b_2 & b_1 & & \cdot \\ \cdot & b_2 & & \cdot \\ \cdot & \cdot & & 0 \\ \cdot & \cdot & & 1 \end{bmatrix} \tag{5.14}$$

where the subscript, j, on the b_j's in (5.14) does not exceed $j = Q$. Finally, we define the $\underline{s}$ and $\underline{v}$ noise processes as independent Gaussian random vectors with known statistics

$$\underline{s} = \mathrm{N}(\underline{m}_s\ ,\ \Sigma_s) \qquad\qquad \underline{v} = \mathrm{N}(\underline{0}\ ,\ \Sigma_v) \tag{5.15}$$

With this vector/matrix system notation, and the fact that a causal driving process will produce a causal $f[n]$, we can write that

$$\underline{s} = \frac{1}{a_0}\,\mathbf{B}\,\underline{f} \quad \text{or} \quad \underline{f} = a_0\,\mathbf{B}^{-1}\,\underline{s} \tag{5.16}$$

so that

$$\underline{y} = \underline{f} + \underline{v} = a_0\,\mathbf{B}^{-1}\,\underline{s} + \underline{v} \tag{5.17}$$

It then follows directly that

$$\underline{m}_{y|r} = a_0\,\mathbf{B}^{-1}\,\underline{m}_s \qquad \text{and} \qquad \Sigma_{y|r} = a_0^2\,\mathbf{B}^{-1}\,\Sigma_s\,\mathbf{B}^{-1^T} + \Sigma_v \tag{5.18}$$

Using these forms in (5.11) we see that the ML minimization problem is, in general, nonlinear.

The Gaussian all-pole ML estimation problem does reduce to a linear estimation problem under degenerate conditions. Specifically, if there is no uncertainty in the source, (i.e. if $\Sigma_s = 0$), then it follows directly that the estimation problem is linear. On the other hand, if

there are perfect observations (i.e. if $\Sigma_\nu = 0$), then the ML solution is given by $a_0 = 0$ while the b_j's are arbitrary. This is clear from (5.18) since, if both Σ_ν and a_0 are zero, the log of the determinant in (5.11) is infinitely negative. Thus, in order for the perfect observations case to be well-posed, a_0 must be known and must be non-zero. If a_0 is, in fact, known and non-zero, the estimation of the all-pole parameters is a linear problem.

5.4.3 The Gaussian All-Zero ML Problem

In Figure 5-5 we show a linear system, with unit sample response $a[n]$, driven by a causal Gaussian process, $s[n]$. Again, the observed sequence, $y[n]$, is equal to the output of the system, $f[n]$, corrupted by an additive Gaussian noise process, $v[n]$, which is independent of $s[n]$. This time we model the system response, $a[n]$, as an all-zero signal and again, we maintain the notation from equation (5.5). Specifically, the z-transform of $a[n]$ is given by eq (5.5) with $B_Q[z] = 0$ (i.e. $a[n] = a_n$, $n = 0, 1, \cdots P$). Then, in addition to the vector notation in (5.13), and the noise statistics in equation (5.15), we define the $N \times N$ matrix, $\mathbf{A}$, as

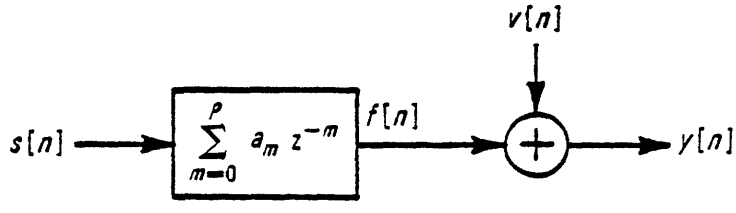

Figure 5-5. The all-zero model

$$\mathbf{A} = \begin{bmatrix} a_0 & 0 & & 0 \\ a_1 & a_0 & & \cdot \\ a_2 & a_1 & & \cdot \\ \cdot & a_2 & & \cdot \\ \cdot & \cdot & & 0 \\ \cdot & \cdot & & a_0 \end{bmatrix} \tag{5.19}$$

(where the subscript, j, on the a_j's does not exceed $j = P$). Now, because $s[n]$ is causal, we have that

$$\underline{y} = \mathbf{A}\,\underline{s} + \underline{v} \tag{5.20}$$

and we obtain the following expressions for the conditional mean and covariance

$$\underline{m}_{y|r} = \mathbf{A}\,\underline{m}_s \qquad \text{and} \qquad \Sigma_{y|r} = \mathbf{A}\,\Sigma_s\,\mathbf{A}^T + \Sigma_v \tag{5.21}$$

which is in the same form as (5.18), with $a_0\,\mathbf{B}^{-1}$ replaced by $\mathbf{A}$. When substituted into (5.11), the result is also difficult to minimize.

In the degenerate cases of perfect source knowledge and perfect observations, the same results as the all-pole case are obtained. That is, if $\Sigma_s = 0$ the all-zero problem becomes linear, while if $\Sigma_v = 0$ the problem is linear only if a_0 is known and non-zero.

5.4.4 The Gaussian Pole-Zero ML Problem

In Figure 5-6 we show a pole-zero linear system. As before, the system is driven by a causal Gaussian process, $s[n]$, and the observed sequence, $y[n]$, is equal to the output of the system, $f[n]$, corrupted by an additive Gaussian noise process, $v[n]$, which is independent of $s[n]$. This time we use the full pole-zero model for the system given in equation (5.5). We use the notation of the last two sections to arrive directly at the result that

$$\underline{y} = \mathbf{A}\,\mathbf{B}^{-1}\,\underline{s} + \underline{v} = \mathbf{B}^{-1}\,\mathbf{A}\,\underline{s} + \underline{v} \tag{5.23}$$

To see this, one can view a pole-zero system as either an all-pole system followed by an all-zero system, or an all-zero system followed by an all-pole system. From this result, it follows that

$$\underline{m}_{y|r} = \mathbf{A}\,\mathbf{B}^{-1}\,\underline{m}_s \qquad \text{and} \qquad \Sigma_{y|r} = \mathbf{A}\,\mathbf{B}^{-1}\Sigma_s\,\mathbf{B}^{-1^T}\mathbf{A}^T + \Sigma_v \tag{5.24}$$

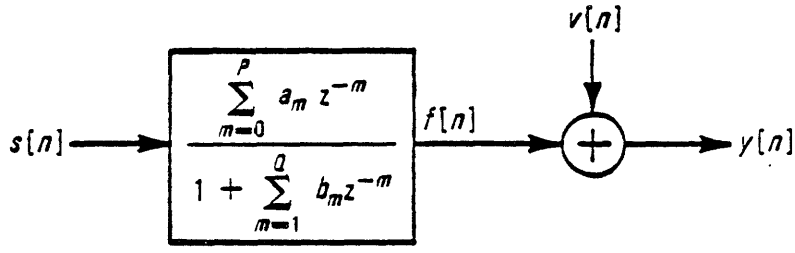

Figure 5-6. The pole-zero model

and, not surprisingly, the Gaussian pole-zero ML minimization problem is difficult to solve.

In both the perfect source knowledge case as well as the perfect observations case, the ML pole-zero problem degenerates as before. If the source is known, the estimation of the poles and zeros is a linear problem. If the observations are perfect and a_0 is known and non-zero, then the pole-zero estimation problem also reduces to a linear problem.

5.5 Musicus' Iterative Maximum Likelihood Method

Musicus has recently developed an iterative approach to solving nonlinear ML estimation problems [23]. In the specific case of Gaussian pole-zero, all-pole and all-zero ML problems, Musicus' scheme is particularly attractive, as we will see in the next section. In this section we present the iterative method in its most general form.

To motivate the theory, we first consider the introduction of an auxiliary signal, $\underline{x}$, into the problem formulation. This signal is properly thought of as a signal internal to the system model which we have no direct means of measuring or observing. Assume for the moment that this signal is known to be equal to $\underline{x}^*$. Then, with the knowledge of this internal signal, we might restate our estimation problem as

$$\hat{\underline{r}} = \max_{\underline{r}} \left\{ \log p(\underline{y} \mid \underline{r}, \underline{x}^{*}) \right\} \tag{5.25}$$

$$= \max_{\underline{r}} \left\{ \log p(\underline{x}^{*}, \underline{y} \mid \underline{r}) \right\}$$

The central idea behind Musicus' method is that, through the judicious selection of the $\underline{x}$ signal, the maximization in (5.25) will be an easier task than in (5.7) and hopefully will be a linear estimation problem. In fact, as we will see in the following sections, for the signal models we consider here it will be always be possible to choose $\underline{x}$ such that the estimation problem is linear when $\underline{x}$ is known.

In practice of course, we cannot assume the knowledge of a signal internal to the system model, let alone a specific signal which happens to make the estimation problem linear. Rather, the auxiliary signal will be unknown and random. In this case, one might consider replacing $\underline{x}^{*}$ in (5.25) with an estimate of $\underline{x}$, which we denote as $\hat{\underline{x}}$. That is,

$$\hat{\underline{r}} = \max_{\underline{r}} \left\{ \log p(\hat{\underline{x}}, \underline{y} \mid \underline{r}) \right\} \tag{5.26}$$

Or, as an alternative, we might consider maximizing the expected value of (5.25) over $\underline{x}$ as in

$$\hat{\underline{r}} = \max_{\underline{r}} \; \mathrm{E}_{\underline{x}} \left[\log p(\underline{x}, \underline{y} \mid \underline{r}) \right] \tag{5.27}$$

Equations (5.26) and (5.27) will produce the same estimate if $\underline{x}$ appears linearly in $\log p(\underline{x}, \underline{y} \mid \underline{r})$ and if $\hat{\underline{x}} = \mathrm{E}[\, \underline{x} \,]$ in (5.26). In general, however, equations (5.26) and (5.27) will yield different estimates.

The approaches in (5.26) and (5.27) each have the desirable property that if the distribution for $\underline{x}$ is impulsive, implying that $\underline{x}$ is deterministically known to be equal to $\underline{x}^{*}$, then

they reduce to the estimator in equation (5.25). In addition, (5.27) has the nice property that the estimate will be independent of the specific choice for $\underline{x}$. This is clear since the expectation operation in (5.27) will remove any $\underline{x}$ dependence from the expression. Unfortunately, the estimator defined by (5.27) is not useful because knowledge of the PDF of $\underline{x}$ is needed in order to take the indicated expected value. Just as we could not assume earlier that we had knowledge of an internal signal, we also cannot assume knowledge of the PDF of an internal signal. The estimator in (5.26) is also not useful since it is not clear where $\hat{\underline{x}}$ comes from, and even if it were clear, the method is ad hoc in nature.

The iterative method developed by Musicus follows naturally from this discussion. The method begins with an initial guess of the parameter vector, $\underline{r}$, which we denote as $\hat{\underline{r}}_0$. Then, assuming that these parameters are in fact correct, the PDF of $\underline{x}$ is computed. Because the parameters are presumably not correct, this will give us only an estimate of the PDF for $\underline{x}$. Having done this, the indicated expected value in (5.27) is taken and the result is maximized over $\underline{r}$. The parameter vector associated with the maximum is a new and hopefully improved estimate of the actual parameters. The process can then be repeated. That is, the new estimate can be used to refine the previous estimate of the PDF of $\underline{x}$, which is then used to perform the expected value operation, which in turn, leads to another parameter estimate. The scheme continues in this manner until the successive parameter estimates are no longer changing indicating that convergence has occurred. Mathematically, we can write this iterative procedure as follows

$$\hat{\underline{r}}_i = \max_{\underline{r}} \; \mathrm{E}_{\underline{x}} \left[\log p(\underline{x}, \underline{y} \mid \underline{r}) \mid \underline{y}, \hat{\underline{r}}_{i-1} \right] \tag{5.28}$$

$$= \max_{\underline{r}} \int_X \log p(\underline{x}, \underline{y} \mid \underline{r}) \, p(\underline{x} \mid \underline{y}, \hat{\underline{r}}_{i-1}) \, d\underline{x}$$

where $i = 1, 2, \cdots$ and $\hat{\underline{r}}_0$ denotes the initial guess of the parameters.

Equation (5.28) is the iterative ML estimation method developed by Musicus [23]. He showed that the log likelihood function of the original ML problem, equation (5.7), is theoretically guaranteed to monotonically increase with each iterative pass of this method. He also proved a general convergence theorem which states the following. If the PDFs in the problem formulation are continuously differentiable (implying that they are bounded above) and if the parameter space is compact (i.e. a closed and bounded subset of infinite space), then the sequence of estimates produced by this method will converge to a set of points in parameter space. This set of points consists of (i) parameters which map into local maxima of the log likelihood function, (ii) parameters which map into inflection points of the log likelihood function, and (iii) points on the boundary of the parameter space which map into maxima or inflection points of the log likelihood function which are on the image of the parameter space boundary.

Several comments are in order regarding this convergence result. First, in many signal models of interest probability desities are smooth and bounded but the parameter space is not compact. In these cases, convergence cannot be guaranteed. Intuitively, the compactness condition is needed so that the parameters do not drift off to infinity and the smoothness condition on the PDFs is needed so that the log likelihood function does not become infinite. Secondly, even if the conditions for convergence are satisfied, convergence is only guaranteed to a set of points, not to a single point. This means that it is possible for successive estimates to "wander around" the set of points and not actually converge. This situation is most likely to occur if the log likelihood function function has a flat plateau for a local maximum.

The primary attraction of Musicus' method is in computational efficiency, as we will see in the next section. Other approaches to solving nonlinear ML problems include brute force maximization (in which the log likelihood function is sampled on a grid in parameter-space and the parameters associated with the maximum are selected) and gradient hill-climbing methods (of which Newton-Raphson and Fletcher-Powell methods are popular [11][12]). The primary drawback of these approaches is that they are relatively computationally burdensome.

5.6 The Iterative Gaussian Pole-Zero ML Problem

The power and elegance of the iterative scheme given in equation (5.28) becomes apparent when it is applied to the Gaussian ML pole-zero estimation problem from the Section 5.4. The all-pole and all-zero models will be treated here as special cases of the pole-zero model. Specifically, the all-pole result can be obtained from the pole-zero result by setting $P = 0$, while the all-zero result is obtained when $Q = 0$.

In Figure 5-7 we divide the pole-zero system into an all-pole system followed by an all-zero system and select the auxiliary signal, $\underline{x}$, as the signal inbetween these two systems. This particular choice for the auxiliary signal should come as no surprise since, from our study in Section 5.4, we know that if $x[n]$ is a known signal, then the problem of estimating the parameters is linear. That is, estimating the zeros given $\underline{x}$ is precisely the case of perfect source knowledge (a problem which we found to be linear) and estimating the poles given $\underline{x}$ is precisely the case of perfect observations with a_0 known to be equal to unity (a problem which we also found to be linear).

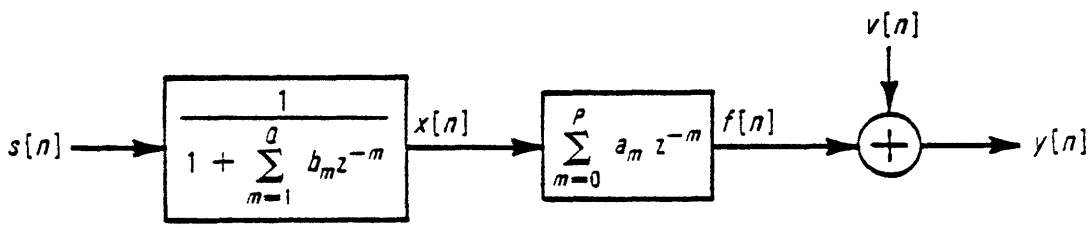

Figure 5-7. The selection of the auxiliary signal in the pole-zero model

5.6.1 Derivation of the Probability Densities

In this section we derive the form of the two probability density functions in equation (5.28) for the pole-zero signal model shown in Figure 5-7. The log of the conditional joint PDF in (5.28) is derived by using Bayes rule as follows

$$\log p(\underline{x}, \underline{y} \mid \underline{r}) = \log p(\underline{y} \mid \underline{x}, \underline{r}) + \log p(\underline{x} \mid \underline{r}) \tag{5.29}$$

To compute the two terms on the right hand side, we make note of the relations

$$\underline{y} = \mathbf{A}\,\underline{x} + \underline{\nu} \qquad \underline{x} = \mathbf{B}^{-1}\,\underline{s} \tag{5.30}$$

where $\underline{x}$ is a vector of length N, defined as the vectors are in (5.13), and **A** and **B** are defined as in (5.19) and (5.14). We obtain directly that

$$p(\underline{y} \mid \underline{x}, \underline{r}) = \mathrm{N}(\mathbf{A}\,\underline{x}, \Sigma_{\nu}) \tag{5.31}$$

and

$$p(\underline{x} \mid \underline{r}) = \mathrm{N}(\mathbf{B}^{-1}\,\underline{m}_s, \mathbf{B}^{-1}\,\Sigma_s\,\mathbf{B}^{-1^T}) \tag{5.32}$$

Combining these last two results gives

$$\begin{aligned} -2 \log p(\underline{x}, \underline{y} \mid \underline{r}) &= 2N \log(2\pi) + \log|\Sigma_{\nu}| + \log|\mathbf{B}^{-1}\Sigma_s\mathbf{B}^{-1^T}| \\ &+ [\underline{y} - \mathbf{A}\,\underline{x}]^T \Sigma_{\nu}^{-1} [\underline{y} - \mathbf{A}\,\underline{x}] + [\underline{m}_s - \mathbf{B}\,\underline{x}]^T \Sigma_s^{-1} [\underline{m}_s - \mathbf{B}\,\underline{x}] \end{aligned} \tag{5.33}$$

The form of the other PDF in (5.30), $p(\underline{x} \mid \underline{y}, \underline{r})$, is obtained directly from (5.33) by recognizing that $p(\underline{x}, \underline{y} \mid \underline{r}) = p(\underline{x} \mid \underline{y}, \underline{r})\, p(\underline{y} \mid \underline{r})$ so that the $\underline{x}$ dependence in (5.33) is the $\underline{x}$ dependence in $p(\underline{x} \mid \underline{y}, \underline{r})$. From (5.33), we see that the $\underline{x}$ dependence is quadratic, implying that $p(\underline{x} \mid \underline{y}, \underline{r})$ is Gaussian and therefore can be written as

$$p(\underline{x} \mid \underline{y}, \underline{r}) = \mathrm{N}(\underline{m}_{x|y,r}, \Sigma_{x|y,r}) \tag{5.34}$$

where

$$\Sigma_{x|y,r}^{-1} = \mathbf{A}^T \Sigma_{\nu}^{-1} \mathbf{A} + \mathbf{B}^T \Sigma_s^{-1} \mathbf{B} \tag{5.35}$$

and

$$\Sigma_{x|y,r}^{-1}\, \underline{m}_{x|y,r} = \mathbf{A}^T \Sigma_v^{-1}\, \underline{y} + \mathbf{B}^T \Sigma_s^{-1}\, \underline{m}_s \tag{5.36}$$

From this result we see that, given the parameters of the system, the inverse covariance matrix for $\underline{x}$ can be computed using (5.35) and the mean of $\underline{x}$ can be found as the solution to the linear equations in (5.36). These two quantities completely specify the PDF for $\underline{x}$ and will be used to take the expected value of (5.33) over $\underline{x}$. Since (5.33) is quadratic in $\underline{x}$, we will need to know the correlation of $\underline{x}$, in addition to its mean. Therefore, the inverse covariance matrix in (5.34) must be inverted, and using the mean, the correlation matrix must be obtained.

5.6.2 The Quadratic Dependence on the Parameters

Taking the expected value of (5.33) over $\underline{x}$ amounts to replacing linear terms in $\underline{x}$ with the mean of $\underline{x}$ and quadratic terms in $\underline{x}$ with the correlation of $\underline{x}$. Having done this, what remains must be maximized over $\underline{r}$. We now show that (5.33) is also quadratic in $\underline{r}$ so that the maximization over $\underline{r}$ requires only linear processing. To see this, we first note that the determinant of B is equal to unity (see eq. (5.14)), so that the $\log |\mathbf{B}^{-1}\Sigma_s \mathbf{B}^{-1^T}|$ term in (5.33) reduces simply to $\log |\Sigma_s|$. Thus, there are no logs of determinants containing parameters which we must minimize over. We now define the parameter vectors

$$\underline{a} = \begin{bmatrix} a_0 \\ a_1 \\ . \\ . \\ a_P \end{bmatrix} \qquad \underline{b} = \begin{bmatrix} b_1 \\ b_2 \\ . \\ . \\ b_Q \end{bmatrix} \tag{5.37}$$

which implicitly make up the vector $\underline{r}$, and the $N \times (P+1)$ matrix C by

$$\mathbf{C} = \begin{bmatrix} x[0] & 0 & & 0 \\ x[1] & x[0] & & . \\ x[2] & x[1] & & x[0] \\ . & x[2] & & x[1] \\ . & . & & . \\ . & . & & . \end{bmatrix} \tag{5.38}$$

and the NxQ matrix D by

$$\mathbf{D} = \begin{bmatrix} 0 & 0 & & 0 \\ x[0] & 0 & & . \\ x[1] & x[0] & & . \\ x[2] & x[1] & & x[0] \\ . & x[2] & & x[1] \\ . & . & & . \\ . & . & & . \end{bmatrix} \tag{5.39}$$

In this way, we may use the relations

$$\mathbf{A}\,\underline{x} = \mathbf{C}\,\underline{a} \qquad\qquad \mathbf{B}\,\underline{x} = \underline{x} - \mathbf{D}\,\underline{b} \tag{5.40}$$

to rewrite (5.33) as

$$-2 \log p(\underline{x}, \underline{y} \,|\, \underline{r}) = [\underline{a} - \underline{m}_a]^T \Sigma_a^{-1} [\underline{a} - \underline{m}_a] + [\underline{b} - \underline{m}_b]^T \Sigma_b^{-1} [\underline{b} - \underline{m}_b]$$

$$+ \text{terms independent of } \underline{a} \text{ and } \underline{b} \tag{5.41}$$

where

$$\Sigma_a^{-1} = \mathbf{C}^T \Sigma_v^{-1} \mathbf{C} \qquad \Sigma_b^{-1} = \mathbf{D}^T \Sigma_s^{-1} \mathbf{D} \tag{5.42}$$

and

$$\Sigma_a^{-1}\,\underline{m}_a = \mathbf{C}^T \Sigma_v^{-1}\,\underline{y} \qquad \Sigma_b^{-1}\,\underline{m}_b = \mathbf{D}^T \Sigma_s^{-1}\,(\underline{x} - \underline{m}_s) \tag{5.43}$$

From this result we see that if the auxiliary signal, $\underline{x}$, is known, then the estimates of the pole-zero coefficients can be obtained as the solution to the linear equations in (5.43). However,

since $\underline{x}$ is not known, we take the expected value of the equation in (5.43) over $\underline{x}$. This involves first estimating the mean and correlation of $\underline{x}$ assuming that the previous parameter estimates are correct, as discussed earlier. Then, linear terms in $\underline{x}$ are replaced with the estimated mean of $\underline{x}$ and quadratic terms in $\underline{x}$ are replaced with the estimated correlation. The result is a new set of linear equations which are then solved to produce a new parameter estimate. The iterative procedure then repeats. The new parameter estimate is used to refine the estimate of the mean and correlation of $\underline{x}$ which in turn leads to a refined parameter estimate.

5.6.3 Summary of the Iterative Procedure

The iterative ML procedure for the Gaussian pole-zero problem can now be explicitly stated. Begin with an initial estimate for the model parameters, $\hat{\underline{r}}_0$. Then, successive estimates are obtained by the following 3-part procedure

$$\text{for } l = 1, 2, \cdots$$

(1) Estimate the statistics of the auxiliary signal.

(a) Estimate the inverse of the covariance matrix, $\Sigma_{x}^{-1}|_{y,l}$, by computing (5.35) using $\hat{\underline{r}}_{l-1}$.

(b) Estimate the right-hand-side of (5.36) by computing the right-hand-side of (5.36) using $\hat{\underline{r}}_{l-1}$.

(c) Estimate the mean of the auxiliary signal, $\underline{m}_{x|y,l}$, by solving the system of equations in (5.36) using the estimated quantities from parts (1a) and (1b).

(d) Estimate the covariance matrix for the auxiliary signal, $\Sigma_{x|y,l}$, by inverting the matrix in part (1a).

(e) Estimate the correlation matrix for the auxiliary signal using the estimated mean and covariance from parts (1c) and (1d).

(2) Compute the expected value of $-2 \log p(\underline{x}, \underline{y} | \underline{r})$.

(a) Use the estimated correlation matrix from part (1e) to take the expected value of the

equations in (5.42).

(b) Use the estimated mean from from part (1c) and the estimated correlation from part (1e) to take the expected value of the right-hand-side of the equations in (5.43).

(3) Solve the two sets of linear equations in (5.43) using the results of parts (2a) and (2b) to obtain the new estimates for the model parameters, $\hat{\underline{r}}$.

5.6.4 Algorithms, Computation and Storage

The computational and storage requirements associated with this procedure were studied in detail by Musicus. To summarize his findings, parts (1a), (1b), (1e), (2a) and (2b) above consist only of vector/matrix multiplies and adds. These operations can be done rapidly, relative to the other steps in the procedure.

Parts (1c) and (3) require the solution to sets of linear equations. The matrix in each case is symmetric and positive definite, so that no pivoting is required and modified Cholesky decomposition can be used. The matrices in part (3) are small relative to the NxN matrix in part (1c). However, the maxtrix in (1c) has only $Q+1$ non-zero diagonals, assuming that $Q \geq P$, so that only these diagonals need be stored. If done carefully, only roughly $N(Q^2+9Q+2)/2$ computations are needed to solve the equations [23].

In part (1d), the NxN matrix from part (1c) must be inverted. However, the processing subsequent to part (1d) only makes use of $Q+1$ diagonals of the NxN covariance matrix. Musicus devised a clever algorithm to evaluate only these elements of the covariance matrix. The method makes use of the in-place Cholesky decomposition from part (1c) and uses only a modest amount of increased storage. The needed elements of the inverse matrix can be computed with roughly $N(Q^2+Q+1)$ computations using this method [23]. When Q is much less than N, this represents a significant savings, relative to computing the entire inverse matrix.

5.6.5 Convergence

As Musicus showed, it is not possible to prove that the sequence of parameter estimates produced by this procedure will converge. Convergence cannot be proved because it is possible to have a pole-zero pair cancellation which drifts off to infinity. Since the parameters can drift to infinity, the parameter space is not compact and the convergence theorem does not apply. In order to guarantee convergence, it must be true that if any of the parameters go to $\pm\infty$, then the log likelihood function must tend to $-\infty$. In this way, the problem can be recast so that the maximization is performed over a closed and bounded subset of infinite space. Such a subset is, by definition, compact, and therefore convergence is guaranteed.

As Musicus showed, convergence is guaranteed in the case where either the poles or the zeros are known. This is clear from the discussion above since there can be no pole-zero pair cancellations which drift to infinity in this case. If any of the unknown parameters drift to $\pm\infty$, the log likelihood function will go to $-\infty$.

As a final note, Musicus showed that the convergence rate of this iterative method is geometric, which can be slow.

5.7 The Iterative Gaussian ML Dereverberation Problem

In this section, we apply the iterative ML theory from Section 5.5 to the Gaussian dereverberation problem for the specific case of the single wavenumber model from Section 5.2.3. As we will see, the dereverberation problem is closely related to the pole-zero estimation problem and the treatment here closely parallels the treatment of Section 5.6.

In Figure 5-8 we show the discrete dereverberation model which is of interest in this thesis. The input to the system is a causal Gaussian random process, $s[n]$, which we use to model samples of the Hilbert transform of a delayed version of the source. The Hilbert transform of the source pulse will have energy for $n < 0$ and the delay is needed so that the result can be modeled as causal. For $n \geq 0$, the stochastic nature of $s[n]$ models the uncertainty in our knowledge of the source pulse.

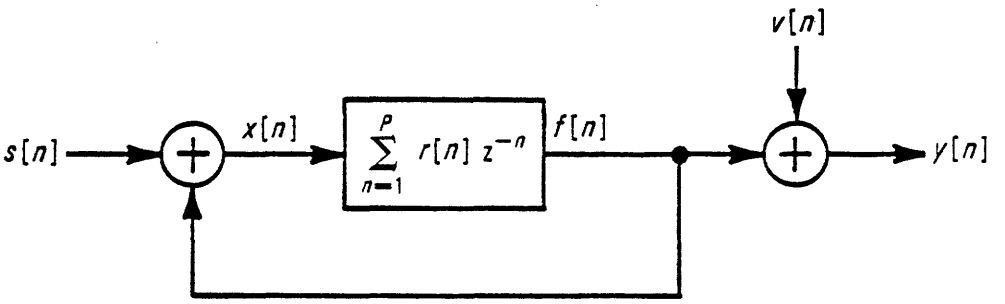

Figure 5-8. The discrete dereverberation model

The $r[n]$ sequence in Figure 5-8 represents samples of the reflection coefficient signal at a single axial wavenumber, $r(t \mid k_z)$, and in the figure we have indicated that $r[n]$ is modeled as all-zero. We elected to use an all-zero model for $r[n]$ because the closed-loop system for this choice is pole-zero where the poles and zeros are related (Section 5.3). That is, this selection corresponds to a constrained pole-zero system. Had we modeled $r[n]$ as all-pole or pole-zero then the closed-loop model would have also been all-pole or pole-zero, respectively. Thus, these latter two choices are no different than the estimation systems treated in Section 5.6.

In an effort to maintain the same notation as before, we model the reflection coefficient sequence with $r[n] = a_n$. Also as before, we measure N samples of the system output, $f[n]$, and denote the measurements by $y[n]$. The measurements differ from the actual output by an amount $v[n]$, which is a zero-mean and possibly non-stationary Gaussian random process, independent of the source process.

Also shown in Figure 5-8 is the selection of the auxiliary signal, $x[n]$, to be used in the iterative scheme. Specifically, we define the auxiliary signal, $x[n]$ by the implicit relationship

$$x[n] = s[n] + x[n] * r[n] \qquad n = 0,1,\ldots,N-1 \tag{5.44}$$

With this choice for $x[n]$, we now show that the nonlinearity in the ML problem decomposes into the iterative solution of only linear problems, as was the case in the pole-zero application.

5.7.1 Derivation of the Probability Densities

Using the same notation as before, and realizing that $P = Q$ in this system, we have that

$$\underline{y} = \mathbf{A}\,\underline{x} + \underline{v} \qquad\qquad \underline{x} = (\mathbf{I} - \mathbf{A})^{-1}\,\underline{s} \tag{5.45}$$

which is precisely the pole-zero system model given in (5.30) with B replaced with I − A. It follows directly that the log likelihood function for this case is given by (5.33) with this same substitution. Specifically,

$$-2 \log p(\underline{x}, \underline{y} \mid \underline{r}) = \left[\underline{m}_s - (\mathrm{I}-\mathrm{A})\underline{x}\right]^T \Sigma_s^{-1} \left[\underline{m}_s - (\mathrm{I}-\mathrm{A})\underline{x}\right] + (\underline{y} - \mathbf{A}\,\underline{x})^T \Sigma_v^{-1} (\underline{y} - \mathbf{A}\,\underline{x})$$

$$+ \log\left|(\mathbf{I} - \mathbf{A})^{-1}\,\Sigma_s\,(\mathbf{I} - \mathbf{A})^{-1^T}\right| + 2N \log(2\pi) + \log|\Sigma_v| \tag{5.46}$$

As before, from this it follows that the conditional density for $\underline{x}$ given $\underline{r}$ and $\underline{y}$ is Gaussian with a mean and covariance given by (5.35) and (5.36) with B replaced with I − A. We give the result of this substitution here

$$\Sigma_x^{-1}|_{y,r} = \mathbf{A}^T \Sigma_v^{-1} \mathbf{A} + (\mathbf{I} - \mathbf{A})^T \Sigma_s^{-1} (\mathbf{I} - \mathbf{A}) \tag{5.47}$$

and

$$\Sigma_x^{-1}|_{y,r}\, \underline{m}_{x|y,r} = \mathbf{A}^T \Sigma_v^{-1}\, \underline{y} + (\mathbf{I} - \mathbf{A})^T \Sigma_s^{-1}\, \underline{m}_s \tag{5.48}$$

From this result we see that, given the reflection coefficient sequence, the inverse covariance matrix for $\underline{x}$ can be computed from (5.47) and the mean of $\underline{x}$ can be found as the solution to the linear equations in (5.48). These two quantities completely specify the PDF for $\underline{x}$ so that we may take the desired expected value of (5.46). Because (5.46) is quadratic in $\underline{x}$, taking the expected value requires knowledge of only the mean and correlation of $\underline{x}$. The mean was found above as the solution to a set of linear equations. The inverse covariance matrix from above must be inverted, and combined with the mean, to obtain the correlation matrix.

5.7.2 Quadratic Dependence on the Parameters

As in the pole-zero case, taking the expected value of (5.46) over $\underline{x}$ amounts to replacing linear terms in $\underline{x}$ with the mean of $\underline{x}$ and quadratic terms in $\underline{x}$ with the correlation for $\underline{x}$. Having done this, what remains must be maximized over $\underline{r}$. We now examine the dependence of (5.46) upon the unknown parameters.

We see immediately that the dereverberation problem is ill-posed if a_0 is not known. Specifically, the determinant of $\mathbf{I} - \mathbf{A}$ is given by $(1 - a_0)^N$. Therefore, the ML solution will be to select an a_0 as large as possible since the log likelihood function in (5.46) is minimized in this case. Viewed in reverse, there will be a strong incentive not to select $a_0 = 1$ since (5.46) is maximized at this point.

In order to make the dereverberation problem well-posed, we will assume that $a_0 = 0$. In this way, the first sample of the reflection coefficient signal is zero, indicating that there is a delay in the signal and that successive reflections are successively delayed, as we would expect. Therefore, we define the parameter vector, $\underline{r}$, to be of length P, instead of $P+1$, as follows

$$\underline{r} = \begin{bmatrix} a_1 \\ a_2 \\ \cdot \\ \cdot \\ a_P \end{bmatrix} \tag{5.49}$$

We now show that, in tying the poles and zero together as we have in this model, equation (5.46) is still quadratic in the parameters. Specifically, we can write

$$\mathbf{A}\,\underline{x} = \mathbf{D}\,\underline{r} \tag{5.51}$$

where $\mathbf{D}$ was defined in (5.39). Upon substituting this into (5.46), we find that we can recast (5.46) into a form where the quadratic dependence on $\underline{r}$ is apparent. Specifically, we can write

$$-2 \log p(\underline{x}, \underline{y} \mid \underline{r}) = (\underline{r} - \underline{m}_r)^T \Sigma_r^{-1} (\underline{r} - \underline{m}_r) + \text{terms independent of } \underline{r} \tag{5.52}$$

where

$$\Sigma_r^{-1} = \mathbf{D}^T \left[\Sigma_r^{-1} + \Sigma_s^{-1} \right] \mathbf{D} \tag{5.53}$$

and

$$\Sigma_r^{-1} \underline{m}_r = \mathbf{D}^T \left[\Sigma_r^{-1} \underline{y} + \Sigma_s^{-1} (\underline{x} - \underline{m}_s) \right] \tag{5.54}$$

From this result we see that if the auxiliary signal, $\underline{x}$ is known, then the estimate of the reflection coefficient sequence can be obtained as the solution to the linear equations in (5.54). However, since $\underline{x}$ is not known, we take the expected value of (5.54) over $\underline{x}$. As mentioned earlier, this amounts to replacing linear terms in $\underline{x}$ with the estimated mean of $\underline{x}$ and quadratic terms in $\underline{x}$ with the estimated correlation. The result is a new set of linear equations which is then solved to produce a new parameter estimate. The iterative procedure then repeats. The new parameter estimate is used to refine the estimate of the mean and correlation of $\underline{x}$ which in turn leads to a refined parameter estimate.

5.7.3 A Summary of the Iterative Procedure

The iterative ML dereverberation scheme can now be explicitly stated. Begin with an initial estimate for the reflection coefficient signal vector, $\hat{\underline{r}}_0$. Then, successive estimates are obtained by following procedure

for $i = 1, 2, \cdots$

(1) Estimate the statistics of the auxiliary signal.

(a) Estimate the inverse of the covariance matrix, $\Sigma_{x|y,r}^{-1}$, by computing (5.47) using $\hat{\underline{r}}_{i-1}$.

(b) Estimate the right-hand-side of (5.48) by computing the right-hand-side of (5.48) using $\hat{\underline{r}}_{i-1}$.

(c) Estimate the mean of the auxiliary signal, $\underline{m}_{x|y,r}$, by solving the system of equations

in (5.48) using the estimated quantities from parts (1a) and (1b).

(d) Estimate the covariance matrix for the auxiliary signal, $\Sigma_{x|y,r}$, by inverting the matrix in part (1a).

(e) Estimate the correlation matrix for the auxiliary signal using the estimated mean and covariance from parts (1c) and (1d).

(2) Compute the expected value of $-2 \log p(\underline{x}, \underline{y} | \underline{r})$.

(a) Use the estimated correlation matrix from part (1e) to take the expected value of (5.53).

(b) Use the estimated mean from from part (1c) and the estimated correlation from part (1e) to take the expected value of the right-hand-side of (5.54).

(3) Solve the set of linear equations in (5.54) using the results of parts (2a) and (2b) to obtain the new estimates for the model parameters, $\hat{\underline{r}}$.

5.7.4 Algorithms, Computation and Storage

The computational and storage requirements associated with this procedure are essentially the same as in the pole-zero case (Section 5.6.4). Again, modified Cholesky decomposition followed by back-substitution can be used to solve the linear equations and Musicus' technique to inverting only the needed diagonals of the covariance matrix applies here as well. As before, the leading order behavior of the computation is $N P^2$.

5.7.5 Convergence

Because the reflection coefficient is theoretically guaranteed to be less than unity in magnitude, it follows that each element of the finite length reflection coefficient sequence is bounded and therefore, that the parameter space is compact. That is, the maximization should only be performed over those parameters which map into reflection coefficients which are less than unity in magnitude and in this way, no parameters can diverge to infinity. If the maximization is indeed restricted to this compact space, then the convergence theorem proved

by Musicus applies to the dereverberation case. However, in the iterative method outlined above there is no guarantee that the parameter estimates will remain within this compact space. Therefore, the estimates may diverge to infinity and convergence is not guaranteed. What is needed, of course, is a method of maximizing the log likelihood function only over the compact space of interest. We have not done this here and conclude that convergence is not guaranteed.

The fact that the dereverberation model can be viewed as a constrained pole-zero model has implications regarding the speed of convergence, provided that it occurs. The time required for an iterative pole-zero estimation method to converge is typically governed by the time required for the zeros to converge, not the poles [24]. Based on this, we intuitively expect that by tying the poles to the zeros as we have, the time required for the dereverberation problem to converge will be slower than the time it takes for the poles to converge, but faster than the time it takes the zeros to converge, in the corresponding unconstrained pole-zero problem. In this sense, the overall convergence properties of the dereverberation problem are expected to be better than those of the corresponding pole-zero problem.

5.8 Summary

We began this chapter with the relationship derived in Chapter III between the reflection coefficient and the reflected component of the field in the borehole and extracted several signal processing models from it. Of the three models which were immediately suggested (i.e. the 2D model, the single frequency model and the single wavenumber model), we selected the single wavenumber model for specific and detailed investigation in this chapter and the next.

We then made the switch to the discrete domain and adopted a pole-zero parametric model representation for the reflection coefficient. With this representation, the reflection coefficient estimation problem is reduced to a problem of estimating a finite set of parameters.

Following this, we focused on the maximum likelihood estimation method for estimating the parameters of the reflection coefficient model. We examined the classical all-pole, all-zero

and pole-zero ML problems, only to find that they are all difficult nonlinear maximization problems, even in the Gaussian case.

Musicus' iterative approach to solving nonlinear ML problems was then intuitively motivated and presented. This method was identified as only one of a number of possible approaches to solving the problem. This was followed by the application of his method to the nonlinear pole-zero problem discussed earlier. Here, the power and elegance of the method became apparent. In effect, through the introduction of an auxiliary signal into the processor, the nonlinearity in the problem decomposed into the iterative solution of two interconnected linear problems. The log likelihood function is guaranteed to monotonically increase and computationally efficient algorithms were devised.

Musicus' iterative ML theory was then applied to the Gaussian ML dereverberation problem for the specific case of the single wavenumber model. The reflection coefficient signal in this model was modeled using an all-zero representation and the result was seen to be a pole-zero problem in which knowledge of the poles implies knowledge of the zeros and vice versa. The application of the iterative ML theory to this constrained pole-zero problem was found to be as powerful and elegant as in the unconstrained case. Furthermore, we expect that, by tying the poles to the zeros, the overall time required for convergence will be less than in the corresponding unconstrained pole-zero case.

VI. THE SINGLE WAVENUMBER SYSTEM

6.1 Introduction

In this chapter we present and analyze the results of applying the iterative maximum likelihood dereverberation method developed in Section 5.7 to the single wavenumber processing model described in Section 5.2. Arrays of synthetic acoustic well logging waveforms, computed using the method described in Chapter IV, are used here as a data base. In this way, we are able to make a meaningful evaluation of the iterative ML method, as discussed earlier.

The goal in the single wavenumber system is to estimate the reflection coefficient associated with the formation as a function of frequency for a single value of axial wavenumber. To review, the single wavenumber system is shown in Figure 6-1. We see that the system is driven by the Hilbert transform of the source pulse and that the system output is the reflected pressure field on the borehole axis at a single axial component of wavenumber. The problem, then, is to estimate the slice of the reflection coefficient given noisy observations of the single wavenumber pressure field, the statistics of the observation noise, the best guess of the source pulse, and the statistics of our uncertainty in the source.

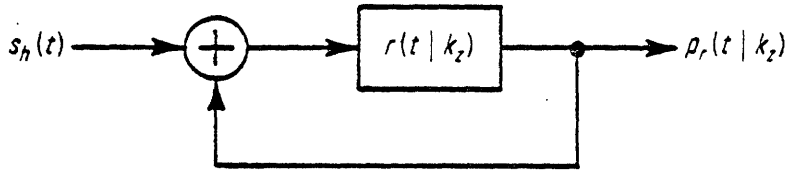

Figure 6-1. The single wavenumber system

In Figure 6-2, we show the discrete domain representation of the single wavenumber system shown in Figure 6-1. Here we have represented the Fourier transform of the slice of the

reflection coefficient by its discrete time samples. The input and output of the discrete system in Figure 6-2 are, again, given by the samples of the continuous signals in Figure 6-1. This is a natural representation since the data acquisition will typically be done digitally.

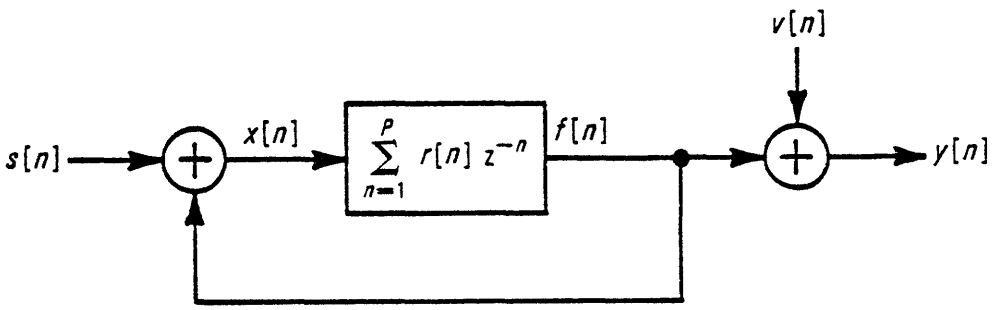

Figure 6-2. The discrete time dereverberation system

This chapter is structured according to the following outline. First, we put forth a sequence of experiments designed to isolate and test various aspects of interest concerning the iterative ML dereverberation method. Then, we conduct the experiments and present the results. Following this, the results are assimilated and some preliminary conclusions are drawn. Finally, we point the way toward future research relative to the single wavenumber system.

Before proceeding with the experiment design, two important issues must first be explored. The first is the estimation, or extraction, of the single wavenumber reflected pressure field from the reflected component of the total field containing all wavenumbers. Here, the primary issue is how to perform this extraction with only a finite aperture receiver array. We discuss this subject in Section 6.2. The other issue we must explore is the duration of the reflection coefficient signal, and the dependence of the duration on the choice of k_z. This subject is studied in Section 6.3. Following this, we design the sequence of experiments (Section 6.4), present the results from conducting these experiments (Section 6.5), draw some preliminary conclusions (Section 6.6) and point the way for future research (Section 6.7).

6.2 The Reflected Pressure Field at a Single Wavenumber

The estimation performance of the iterative ML method when applied to the single wavenumber dereverberation system will depend strongly on the particular receiver array design. Assuming that the inter-receiver spacing is sufficient to adequately sample the wavelengths involved, the only issues are the length of the array aperture and its placement relative to the source. Taken together, the aperture and its offset give us a window in z through which we observe the reflected field, $p_r(z,t)$. From this spatially windowed version of the field, the problem is to extract the reflected field at a single wavenumber, $p_r(t \mid k_z)$. For a sufficiently large aperture array placed at zero offset from the source, the single wavenumber field can, in theory, be obtained by Fourier transforming the array spatially and evaluating the result at the desired wavelength. The issue here, then, is the extraction of $p_r(t \mid k_z)$ from a limited aperture array.

We examine this issue in this section. We begin by numerically computing the theoretical single wavenumber reflected pressure field on the axis for a specific formation model. Following this, we consider 3 different array designs and in each case, we transform synthetic data across the array and compare the results with the theoretical single wavenumber field. In this way, we are able to evaluate the effects of having a limited aperture of data. We do not explore other approaches to obtaining $p_r(t \mid k_z)$ from a finite aperture array.

6.2.1 The Theoretical Single Wavenumber Reflected Pressure Field

In Figure 6-3 we show the theoretical single wavenumber reflected pressure field on the axis of the borehole as a function of time for 10 values of axial wavenumber. The axial wavenumbers range from 0 cm^{-1} to 1 cm^{-1} in increments of 1/9. These waveforms correspond to an infinite homogeneous elastic solid formation model which has a compressional speed of 3.5 Km/s and a shear speed of 2 Km/s. The borehole fluid speed was taken to be 1.5 Km/s and the ratio of the formation density to the borehole fluid density was taken to be 2. The borehole radius was chosen to be 10 cm. Finally, a 2^{nd} derivative of a Blackman window, 100 μs in duration, was used as a source pulse. A pulse of this type is shown in Figure 4-7.

Mathematically, the signals in Figure 6-3 were obtained by numerically integrating the

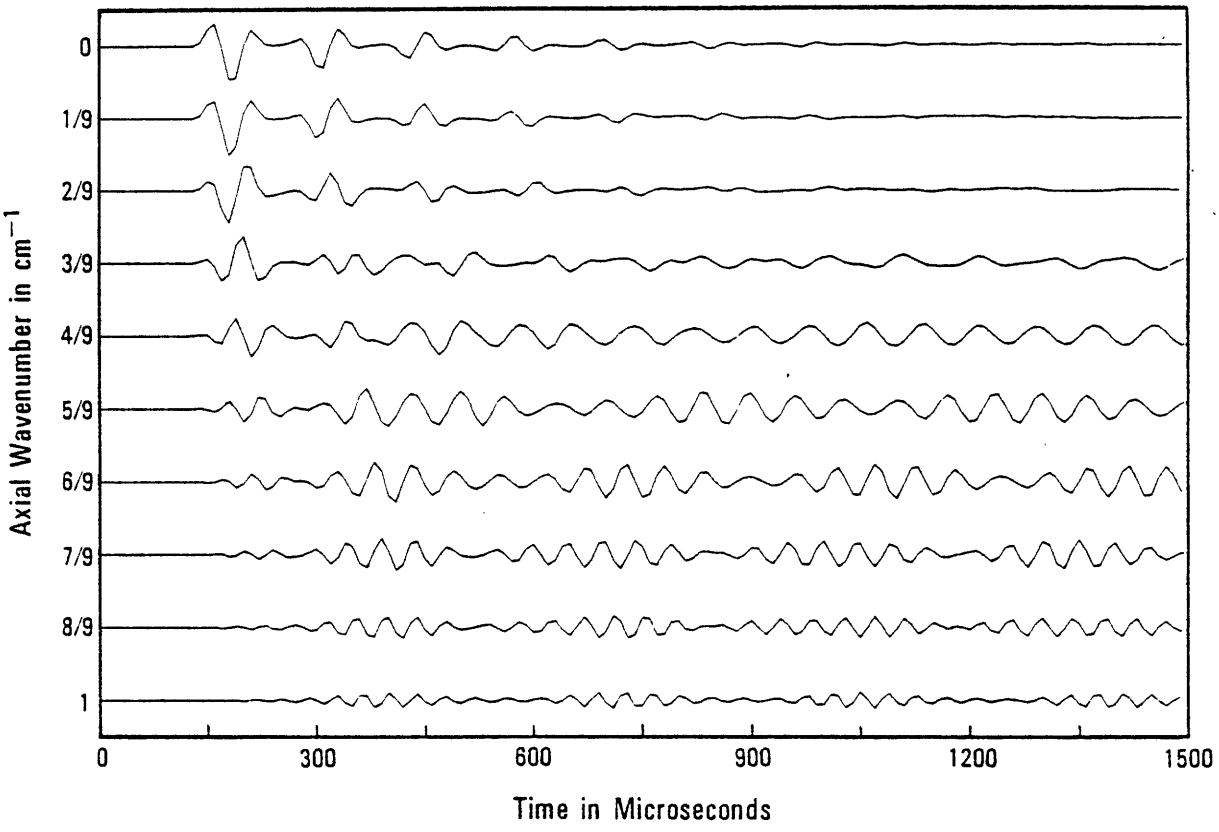

Figure 6-3. The theoretical single wavenumber reflected pressure field

following expression 10 times, each with a different value of k_{z_0}.

$$p_r(t \mid k_{z_0}) = \frac{e^{\alpha' t}}{2\pi} \int_{-\infty}^{\infty} \left\{ H(\omega)\ S(\omega)\ \sum_{m=1}^{\infty} R^m(k_{z_0}, \omega) \right\} e^{-i\omega' t} d\omega' \tag{6.1}$$

This is equivalent to equation (4.1) with $D(k_z) = \delta(k_z - k_{z_0})$, demodulated to remove the $e^{ik_{z_0}z}$ spatial dependence. That is, the signals in Figure 6-3 can be interpreted as the reflected component of the field in the hole due to a line source with a spatially sinusoidal distribution.

Consistent with the line source interpretation, note in Figure 6-3 that all 10 signals "arrive" at the time predicted by ray theory, $t = 2a/v_f = 133\ 1/3\ \mu$s, independent of the choice of k_z. However, the general character of the signals changes dramatically with k_z. Specifically, at

small values of k_z the line source effectively beamforms its energy into the formation at normal incidence and the waveforms show each individual reflection of the source pulse off the borehole wall. Note that the successive reflections change in shape and attenuate geometrically.

At intermediate values of axial wavenumber (specifically, note the signal in Figure 6-3 which corresponds to $k_z = 4/9\ \mathrm{cm}^{-1}$, or an axial component of wavelength of 5.57 inches) the pressure signal is seen to change from a sum of individual reflections at early times to a steady-state sinusoidal type of behavior as time increases. This sinusoidal behavior corresponds physically to the excitation of a mode in the borehole. That is, for this value of k_z, there exists an ω such that the (k_z, ω) pair precisely satisfies the condition for a propagating mode.

This modal behavior can be explained equally well from a signal processing perspective. Specifically, in the frequency domain, imagine the effects of summing the successively reflected signals. The Fourier transform of the total signal is given by the sum of the transforms of the individual signals of which it is composed. At a given frequency, the phase of the transform of the individual pulses will generally not all be the same and the magnitude will generally be less than unity. Therefore, summing the individual transforms at that frequency will be incoherent, meaning that the sinusoidal "waves" at that frequency tend to destructively interfere. The result is a relatively small total. The condition for a "mode" to occur at some frequency, then, is for the reflection coefficient to equal unity at that frequency. In this way, the phases of all the individual reflections add constructively and, because the magnitude of the reflection coefficient is unity, the overall transfer function has a pole at that frequency.

At the larger values of k_z in Figure 6-3, the signals are seen to exhibit more complicated behavior with increasing time. Specifically, we see bursts of sinusoids, where the bursts themselves appear periodically. Physically, this corresponds to the interference between more than one mode. That is, there are actually several sinusoids present in these signals at late times and one sees only the interference effects corresponding to the sum of the sinusoids.

6.2.2 The Extraction of $p_r(t \mid k_z)$ From an Array

In Figure 6-4 we show 10 $p_r(t \mid k_z)$ signals to be compared with those in Figure 6-3. These signals were obtained by tapering an array of synthetic waveforms with a Blackman window and transforming the result over space. Specifically, the synthetic array of data shown in Figure 4-9 was used here because the parameters associated with this synthetic data set are precisely those used in Figure 6-3. The receiver array consists of 100 elements spaced 1" apart, which implies an aperture of 8'3". The transmitter-receiver spacing (TRS) was zero, implying that the first receiver in the array is located at the position of the point source.

Comparing Figure 6-4 with Figure 6-3, we note that the dominant effect associated with the use of a finite aperture array is to reduce the amplitude of the large time behavior. This is partially due to the use of the Blackman window, but primarily due to the fact that the modes propagate out beyond the extent of the array. In the limit as the receiver array aperture extends out to infinity, the $p_r(t \mid k_z)$ signals obtained by transforming the array of data will approach the signals in Figure 6-3.

In Figures 6-5 and 6-6 we see the results of spatially transforming two different receiver arrays. Figure 6-5 corresponds to a 50 receiver array with a 2" inter-receiver spacing (an 8'2" aperture), while Figure 6-6 is a 50 receiver array with a 1" spacing (a 4'1" aperture). The TRS is zero in each case. Thus, the array corresponding to Figure 6-5 was obtained from the array corresponding to Figure 6-4 by eliminating every other element while the array corresponding to Figure 6-6 was obtained from the array corresponding to Figure 6-4 by eliminating the last half of the array.

Note that in Figure 6-5 the large time behavior is similar to that in the 100 receiver case, Figure 6-4, because the array aperture is roughly the same in the two cases. This is in contrast with Figure 6-6 where the shortened aperture is seen to greatly reduce the sensing of the modes. Also note that the shortened array tends to follow Figure 6-4 better at early times than the array obtained by eliminating every other receiver. This is due to the fact that the array which samples the field every 2" is actually inadequate at the larger values of k_z. That is, the wavelength associated with the last signal (i.e. $k_z = 1$ cm^{-1}) is just less than 2.5" which is inadequately

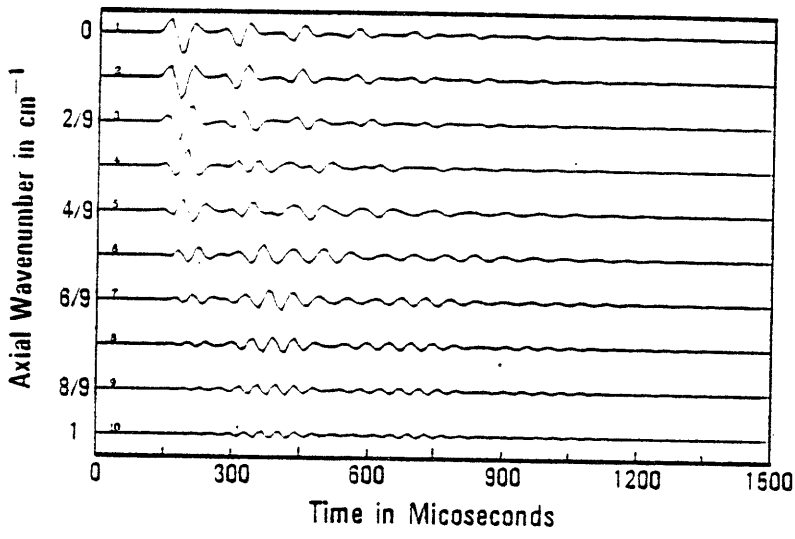

Figure 6-4

The single wavenumber field from an array of 100 receivers at 1" spacing.

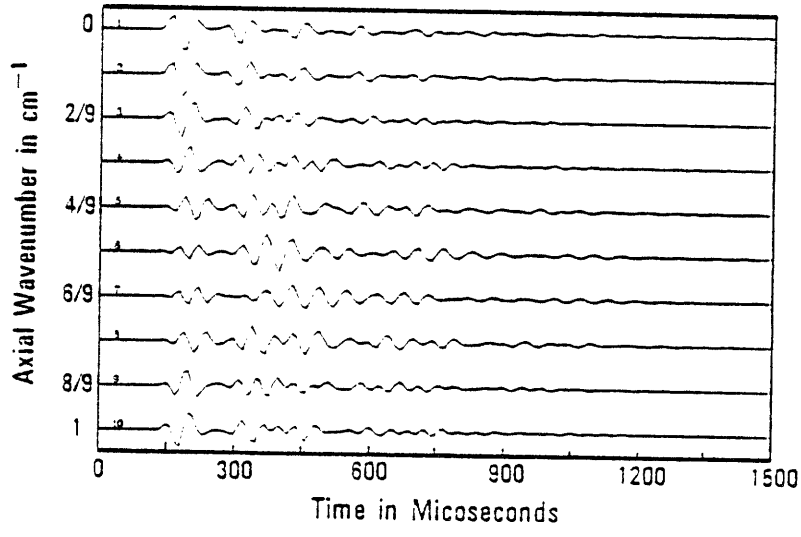

Figure 6-5

The single wavenumber field from an array of 50 receivers at 2" spacing.

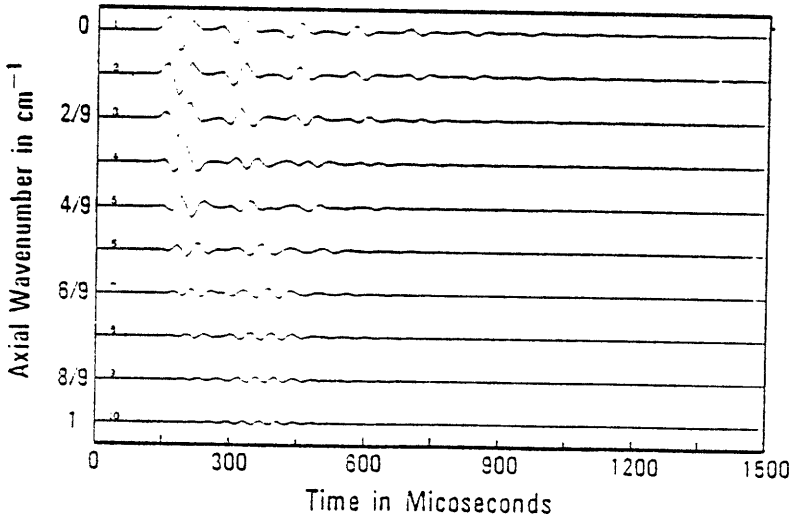

Figure 6-6

The single wavenumber field from an array of 50 receivers at 1" spacing.

sampled by an array with 2" spacing.

In conclusion, for a given k_z, each frequency will propagate to some axial distance from the source. Those frequencies corresponding to modes will propagate to very large distances, while those that do not are relatively contained axially. Thus, it appears that there is a "reasonable" distance beyond which most frequencies do not propagate and that the array aperture should be chosen roughly equal to this distance. In order to capture the modes, a much longer array is needed. It is felt that an array this long is impractical for a variety of reasons.

The single wavenumber reflected field obtained by transforming a finite aperture array of reflected field data will be least accurate at those frequencies corresponding to the modes. Assuming adequate spatial sampling and a transmitter-receiver spacing of zero, the accuracy of the single wavenumber field will depend strongly on the length of the aperture.

6.3 The Theoretical Reflection Coefficient and Its DFT

We begin this section with a brief review of the nature of the reflection coefficient as a function of frequency for a fixed axial component of wavenumber. Here, we illustrate the close relationship between the choice of a source pulse and the choice of an axial wavenumber. Following this, we focus on the issue of the duration of the reflection coefficient signal. Somewhat surprisingly, we find that there are two different ways to define the reflection coefficient signal, each of which leads to signals of the same duration, but one of which is more convenient to use than the other.

6.3.1 The Theoretical Reflection Coefficient

In Figure 6-7 we show the magnitude of the theoretical reflection coefficient, $R(\omega \mid k_z)$, for the formation model considered above and for the same 10 values of k_z. The first signal in Figure 6-7, however, is not a reflection coefficient, but is the magnitude of the Fourier transform of the source pulse. The magnitude of the transform of the source has been included in Figure

6-7 because we anticipate that we will have difficulty estimating the reflection coefficient at those frequencies where the source energy is relatively low. The reflection coefficient at $k_z = 0$ is the second signal in Figure 6-7, and the reflection coefficient at $k_z = 1/9, 2/9, \cdots 1$ follow in order.

The features of a slice of the reflection coefficient at constant k_z were discussed in Chapter 2 and are reviewed here. Moving from left to right across these waveforms, the first feature is a spike which corresponds to the excitation of a Stoneley wave. The second feature is the left edge of the "table" and occurs at a frequency equal to the product of the axial wavenumber and the fluid speed. The third feature is the right edge of the table and occurs at the shear speed multiplied by k_z. Finally, the right most peak occurs at the compressional speed multiplied by k_z. The fact that the "table" is perfectly flat, with sharp edges, indicates that there is no attenuation in the borehole fluid and no attenuation in the shear propagation. The fact that the compressional peak is sharp also indicates the presence of elastic compressional propagation. Finally, the high frequency asymptotic value of the magnitude of reflection coefficient is given by the magnitude of the plane wave reflection coefficient associated with a liquid/solid interface at normal incidence.

The signals in Figure 6-7 lend insight into the design of the source pulse. Specifically, the passband of the pulse should be selected so that it excites the features of interest in the reflection coefficient at the k_z of interest. Viewed in reverse, the axial component of wavenumber should be selected so that the interesting features of the reflection coefficient at that k_z fall within the passband of the source. Whether the source is distributed spatially, or is a point in space, is not important in this system.

6.3.2 The Theoretical Reflection Coefficient Signals

To this point, we have defined the reflection coefficient signal as the Fourier transform of the reflection coefficient. From Figure 6-7 we see that the theoretical reflection coefficient has infinite bandwidth, which implies that the numerical computation of samples of the Fourier transform of the reflection coefficient cannot be approximated in a straightforward manner with a

discrete Fourier transform (DFT).

One procedure for numerically computing samples of the Fourier transform of the reflection coefficient is based in part on the DFT and in part on analytic methods. In this scheme, the high frequency asymptotic behavior of the reflection coefficient can be subtracted out, leaving a new frequency function which approaches zero at large frequencies. The Fourier transform of this new frequency function can then be accurately approximated using a DFT. Following this, the Fourier transform of the asymptotic behavior can be performed analytically and samples of it can be added onto result of the numerical transform. In this way, samples of the Fourier transform of the reflection coefficient can be computed.

Rather than define the discrete time reflection coefficient signal by samples of the continuous Fourier transform, suppose instead that we define it as the DFT of samples of the continuous reflection coefficient out to some maximum frequency. Samples of the reflection coefficient beyond this maximum frequency are ignored. This definition represents a simplification over the previous definition since only a DFT of the sequence is needed to recover the samples of the reflection coefficient out to the maximum frequency chosen.

The reflection coefficient signals associated with these two definitions will certainly be different. However, while we do not show it here, we have found that the duration of the signals associated with these two definitions is roughly the same. This being the case, we adopt the simpler DFT definition from now on.

In Figure 6-8 we show the result of taking the DFT of the reflection coefficient samples in Figure 6-7 out to some maximum frequency. In the figure, we show only the first 1.5 ms (151 samples with a 10 μs sampling period) of the result. Note that these signals are not zero prior to $t = 2a/v_f$, as one might have thought on physical grounds, but they are "approximately causal". This is consistent with the findings in Chapter III where we saw that the decomposition of the field into a series of individual reflected arrivals was non-physical.

From Figure 6-8, it would appear that the reflection coefficient signals are only, say, 30

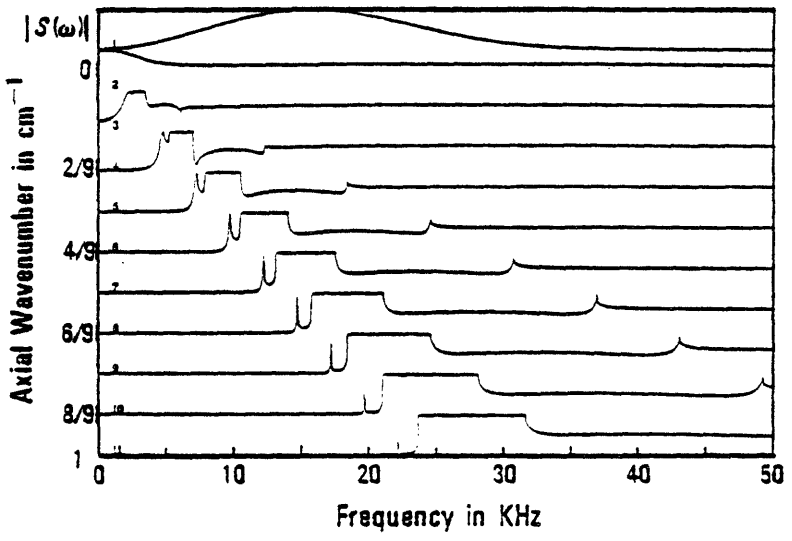

Figure 6-7

Slices of the magnitude of the theoretical reflection coefficient

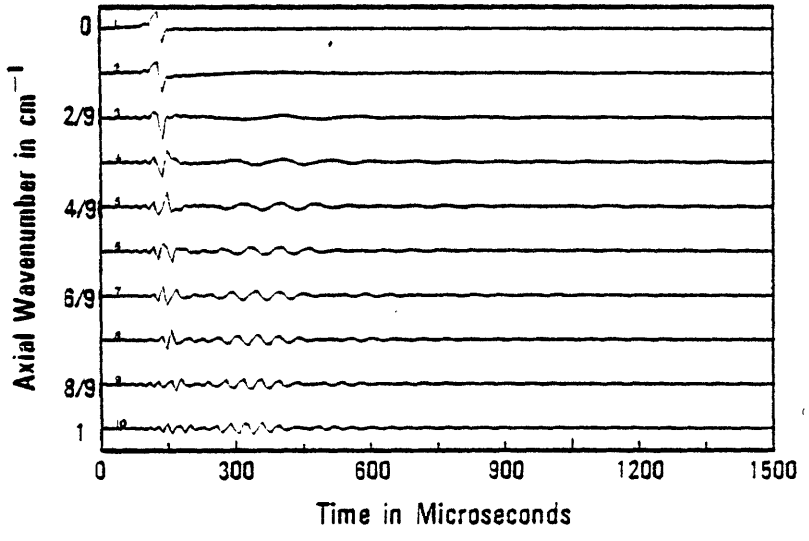

Figure 6-8

The theoretical reflection coefficient signals

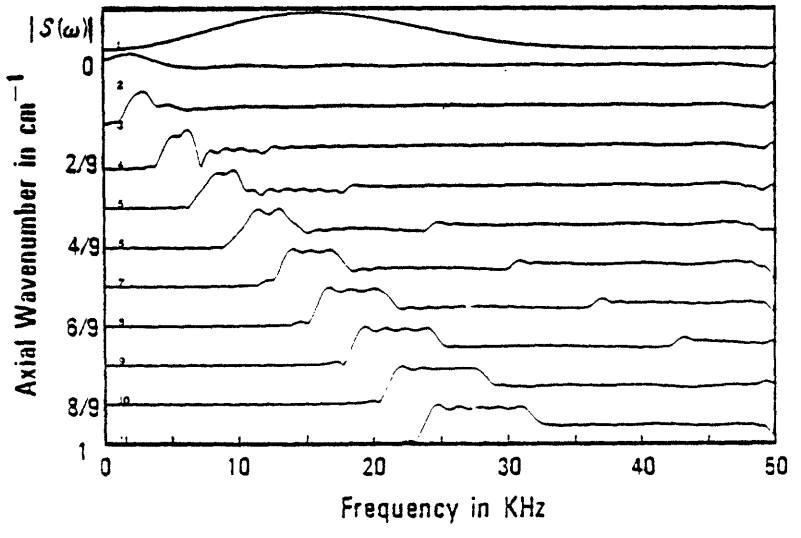

Figure 6-9

The frequency domain effects of a 100 point reflection coefficient signal

samples long at small values of k_z (i.e. 300 μs in duration) and 60 samples long at larger values. However, the apparent length of these signals is misleading for the following reason. Our interest is in the DFT of these sequences which we know to have very sharp features in the frequency domain. This implies that its transform has a long duration and that, by using only a small number of samples, resolution will be lost in the frequency domain. We conclude that the seemingly low amplitude long duration components of the signals in Figure 6-8 are, in fact, significant.

In Figure 6-9 we show the results of taking the DFT of the first 101 points (1ms) of the signals in Figure 6-8. No window function was applied. Comparing Figure 6-9 with 6-7, we see that the Stoneley feature is not resolved but that the other features are. We have found that the use of less that 101 points results in a significant loss in resolution, as does the use of a tapered window function. While longer reflection coefficient sequences will produce improved resolution, we view the result with 101 points to be adequate, and that larger values of P produce a small increase in resolution with a large increase in computation time.

6.4 Experiment Design

In this section we design a set of case studies, or experiments, which will structure the testing and evaluation of the iterative ML dereverberation method as it applies to the single wavenumber model. The hope is that, by analyzing the results of the sequence of experiments outlined here, some definitive statements can be made concerning the performance of the method.

The design of the experiments depends to a large extent upon what is of specific interest to us. Of particular concern here is the performance of the method for different choices of a receiver array and for different signal-to-noise ratios (SNR's). Specifically, if we find that the method only works well if the array aperture is 20 feet long or longer, and/or if the SNR is 100dB or better, then the practical usefulness of this method is doubtful. On the other hand, if the method performs satisfactorily on data from an aperture only a few feet long and at fairly

high noise levels, then the method has at least a chance to develop into a practical logging method.

Of secondary concern are the issues of computation time per iteration, and, assuming that the method converges, the number of iterations required to reach convergence and the uniqueness of the estimate. Also, there is the issue of the sensitivity of the convergence behavior to the initial guess for the reflection coefficient sequence. Again, the hope is that the computation time per iteration will be small and that convergence will occur to the "right answer" in a small number of iterations, independent of the initial guess for the reflection coefficient.

Also of secondary concern is the evaluation of the method on a large number of formation models. It is felt that while this is a necessary study if the method is to be developed further, it is not appropriate at this point.

Because we will focus primarily on the issues of array design and signal-to-noise ratio, we choose to hold all the other parameters in this system constant in each experiment. That is, in each experiment we will vary only one parameter at a time; either the choice of an array, or the noise level. In this way, the effect of one issue at a time can be isolated and understood. In the next subsection, we present the selection of the parameters which we hold fixed. Following this we present four array designs we will consider and then define the signal-to-noise ratio so that we may quantify the study of noise sensitivity. Finally, we explicitly state the sequence of experiments we will carry out.

6.4.1 Fixed Parameters in the Experiment

We limit our investigation to the formation model and associated parameters considered previously. That is, the formation is modeled as a perfectly elastic solid medium with a compressional speed of 3.5 Km/s and a shear speed of 2.0 Km/s. The fluid in the borehole is elastic with a speed of 1.5 Km/s and the ratio of the formation density to the fluid density is taken to be 2. Finally, the borehole radius is 10 cm.

In addition to the borehole and formation models, we will also assume the use of a point source whose waveform is given by a 2^{nd} derivative of a Blackman window which is 100 μs in duration. The signal which drives the system is the Hilbert transform of this pulse, which will be non-causal. The effect of the Hilbert transformer is to smear the actual source pulse into negative time and also beyond 100 μs. For this reason, we add an artificial delay, δ, of 50 μs into the source pulse. In this way the Hilbert transform of the delayed source pulse is effectively zero prior to $t = 0$ and extends out to roughly 200 μs.

Given this selection for a source pulse, we see from Figure 6-7 that if we select $k_z = 4/9$ cm^{-1} then the interesting features of the reflection coefficient fall into the passband of the source pulse. In addition, we know from Figure 6-3 that one and only one mode will be excited with this choice so that we can examine the performance in the presence of a mode. For these reasons, we make this selection of the axial wavenumber. We note that the axial component of wavelength is given by $\lambda_z = 2\pi/k_z = 14.14$ cm = 5.57 inches, or roughly half a foot.

In addition to the above restrictions, we will assume that the reflection coefficient signal at this k_z is roughly 1 ms in duration, or 101 samples long. From Figure 6-9, we see that the DFT of the first 101 points of the reflection coefficient signal possesses the essential features of the actual reflection coefficient. Finally, we will assume only 1.5 ms of observations, or 151 time samples. However, upon adding in the artificial 5 samples of delay, the length of the observation sequence is given by $N = 156$.

In Table 6-1, we list the values of the parameters which we have fixed in the experiments which follow.

6.4.2 Four Array Designs

Having selected the source design, the formation model and parameters, the sequence lengths and the axial component of wavenumber, our experiments will be centered around

various choices for a receiver array design. The purpose here is to investigate the performance of the method from data provided by limited aperture receiver array.

We will examine the performance of the method for four different choices of an array. These choices correspond to the arrays associated with Figures 6-3 through 6-6. That is, the first array we consider is actually a degenerate choice in which the array aperture is essentially infinite and the inter-receiver spacing and the transmitter-receiver spacing are effectively zero. In this case, the signal in Figure 6-3 corresponding to $k_z = 4/9\text{cm}^{-1}$ represents the ideal $p_r(t \mid k_z)$ signal which would be extracted from such and array. We choose to examine this idealized array so that we may assess the performance of the method under ideal conditions and compare the performance with that of finite aperture cases.

The remaining three choices correspond to the use of arrays with 100, 50 and 50 elements with spacings of 1", 2" and 1". For the choice of axial wavenumber here, these three arrays are roughly 16, 16 and 8 axial wavelength long with 6, 3 and 6 spatial samples per axial wavelength. The transmitter-receiver spacing in each case is taken to be zero.

In Table 6-2 we summarize the parameters of the arrays associated with each of the four experiments

6.4.3 Signal-to-Noise Ratio

In order to assess the performance of the method in the presence of noise, a meaningful quantitative study must be designed. As a first step in this regard, we will corrupt $p_r(t \mid k_z)$ and the Hilbert transform of the delayed source signal by adding artificially generated stationary zero-mean white Gaussian noise samples to them. This is the simplest possible choice of a noise process since it is characterized completely by the standard deviation of the source and observation noise processes. We denote these as σ_s and σ_r respectively.

Since the absolute noise levels, σ_s and σ_r, are not particularly meaningful, it is customary to compute a statistic which indicates the noise level relative to the signal level; that is, the

Table 6-1. Fixed Experiment Parameters		
Parameter	**Variable**	**Value**
formation compressional speed	v_c	3.5 Km/s
formation shear speed	v_s	2.0 Km/s
borehole fluid speed	v_f	1.5 Km/s
ratio of formation density to fluid density	ρ_1/ρ	2.0
borehole radius	a	10 cm.
source pulse duration	T	100 μs
artificial delay	δ	50 μs
axial component of wavenumber	k_z	.44 cm^{-1}
axial component of wavelength	λ_z	$\sim$ 6 inches
sampling period	Δt	10 μs
no. samples in reflection coefficient signal	$P+1$	101
no. of observation samples (including delay)	N	156

Table 6-2. The Four Arrays Under Consideration				
Array No.	No. Rcvrs	Inter-Rcvr Spacing	Aperture	$p_r(t \mid k_z)$
1	∞	ϵ	∞	Figure 6-3
2	100	1" or 6 samples/λ_z	8' 3" or 16 λ_z	Figure 6-4
3	50	2" or 3 samples/λ_z	8' 2" or 16 λ_z	Figure 6-5
4	50	1" or 6 samples/λ_z	4' 1" or 8 λ_z	Figure 6-6

signal-to-noise ratio (SNR). In this thesis we define the signal-to-noise ratio of the source and observation random processes as follows

$$SNR_r = 20 \log_{10} \frac{\sigma_p}{\sigma_r} \qquad SNR_s = 20 \log_{10} \frac{\sigma_{hs}}{\sigma_s} \tag{6.2}$$

where

$$\sigma_p = \frac{1}{\sqrt{N}} \left[\sum_{n=0}^{N-1} p_r(n\Delta t \mid k_r)^2 \right]^{1/2} \qquad \sigma_{hs} = \frac{1}{\sqrt{N}} \left[\sum_{n=0}^{N-1} \left(s(t-\delta) * h(t) \right)^2_{|t=n\Delta t|} \right]^{1/2} \tag{6.3}$$

For a particular choice of an array, we will study the performance of the system for various choices of σ_s and σ_r.

As an additional study, we also examine the performance of the method when we do not add any artificial noise to either the observations or the source process. This allows us to study the performance under the most favorable conditions. An issue here is how to select appropriate values for σ_s and σ_r to be used in the processor. These quantities cannot be chosen equal to zero since the PDFs become singular if this is done. Therefore, numbers for these standard deviations will be selected and used in the iterative scheme and the signal-to-noise ratios in (6.2) can be computed. However, the SNRs computed this way are not particularly meaningful in this case since we have not actually added any artificial noise into the system.

6.4.4 The Sequence of Experiments

In Table 6-3, we list the array choices and SNR's associated with 15 experiments. This table will be useful in the next section where we refer to the experiment by the entry number in this table.

6.5 Experimental Results

In this section we present the results of the 15 experiments defined in Table 6-3. We

Table 6-3. The List of Experiments

experiment no.	array no.	add noise ?	σ_1	σ_2	SNR_1	SNR_2
1	1	NO	10^{-8}	10^{-8}	58.6	58.7
2	1	NO	10^{-7}	10^{-7}	38.6	38.7
3	1	NO	10^{-6}	10^{-6}	18.6	18.7
4	1	YES	10^{-8}	10^{-8}	58.6	58.7
5	1	YES	10^{-7}	10^{-7}	38.6	38.7
6	1	YES	10^{-6}	10^{-6}	18.6	18.7
7	2	NO	10^{-7}	10^{-7}	38.6	34.4
8	2	YES	10^{-7}	10^{-7}	38.6	34.4
9	2	YES	10^{-6}	10^{-6}	18.6	14.4
10	3	NO	10^{-7}	10^{-7}	38.6	36.6
11	3	YES	10^{-7}	10^{-7}	38.6	36.6
12	3	YES	10^{-6}	10^{-6}	18.6	16.6
13	4	NO	10^{-7}	10^{-7}	38.6	31.4
14	4	YES	10^{-7}	10^{-7}	38.6	31.4
15	4	YES	10^{-6}	10^{-6}	18.6	11.4

present the results of the first experiment in some detail and then present the rest with far less discussion.

6.5.1 The Results of Experiment 1

We see from Table 6-3 that in the first experiment we are using the theoretical single wavenumber reflected pressure field as our observations and we have perfect knowledge of the source process. No artificial noise is added into either the source or the observations. The only issues here are the selection of the noise standard deviations to use in the processor, as discussed earlier, and the issue of having only a finite observation length (which is fixed in all experiments).

a. The Reflection Coefficient Signal Estimates

In Figure 6-10 we show 7 waveforms, each 1ms in duration, corresponding to the reflection coefficient sequence estimates associated with this first experiment. The first waveform shown is the first 101 points of the theoretical reflection coefficient signal (i.e. from Figure 6-8). The second signal in Figure 6-10 is the initial guess of the reflection coefficient signal. This initial guess signal is zero at all points except at the 20^{th} sample, where it equals 0.4. The third signal is the first estimate produced by the iterative ML procedure. The 4^{th} to 7^{th} signals are the results of iterations 6, 11, 16 and 21.

Two observations can immediately be made from Figure 6-10. First, the procedure did not converge after 21 iterations. Secondly, after 21 iterations, the estimate appears to be very different from the actual reflection coefficient signal (which is the first signal). Thus, it would appear that the method is performing extremely poorly, even in the case where we have added no noise into either the source or the observations.

b. The Reflection Coefficient Estimates

In Figure 6-11 we show the DFT's of the signals in Figure 6-10. The first signal in 6-11 is the magnitude of the transform of the source pulse and the second signal in 6-11 is the theoretical magnitude of the reflection coefficient of the formation (i.e. from Figure 6-7). The third signal in Figure 6-11 is the DFT of the first 101 points of the theoretical reflection coefficient signal (i.e. from Figure 6-9). Mathematically, this signal is given by $R(\omega \mid k_z)$ convolved in frequency with $W(\omega)$. Here $W(\omega)$ has a Fourier transform, $w(t)$, which equals unity from $t = 0$ to $t = 1$ ms and is zero otherwise. This signal is, in some sense, the "best" we can hope to achieve with 101 point reflection coefficient model. Finally, signals 4 through 8 in Figure 6-11 correspond to the DFT's of the reflection coefficient signal estimates from iterations 1 through 21 in steps of 5.

We see from Figure 6-11 that the estimates have roughly converged within the passband of the source, but that outside of the passband, convergence has not occurred. Furthermore, approximate convergence within the band resulted after only 11 iterations.

c. Estimates of the Auxiliary Signal

In Figure 6-12 we show the iterative estimates of the mean of the auxiliary signal, $x[n]$. The first signal is the actual $x[n]$ signal while the remaining signals are the estimates after iterations 1 to 21 in steps of 5.

We note from Figure 6-12 that convergence is roughly achieved here after only 5 iterations, which is faster than the convergence of the reflection coefficients. This faster convergence rate for the auxiliary signal estimates is typical of all the experimental results and indicates that the auxiliary signal is not as sensitive to the reflection coefficient signal as we might like. That is, perturbations in the reflection coefficient signal map into much smaller perturbations in the auxiliary signal estimate. The reason for this is that the repeated convolution of the reflection coefficient with itself tends to smooth out the late time portion of the observations and make them relatively insensitive to the specific details of the reflection coefficient. Therefore, changing the details of the reflection coefficient will not change the later

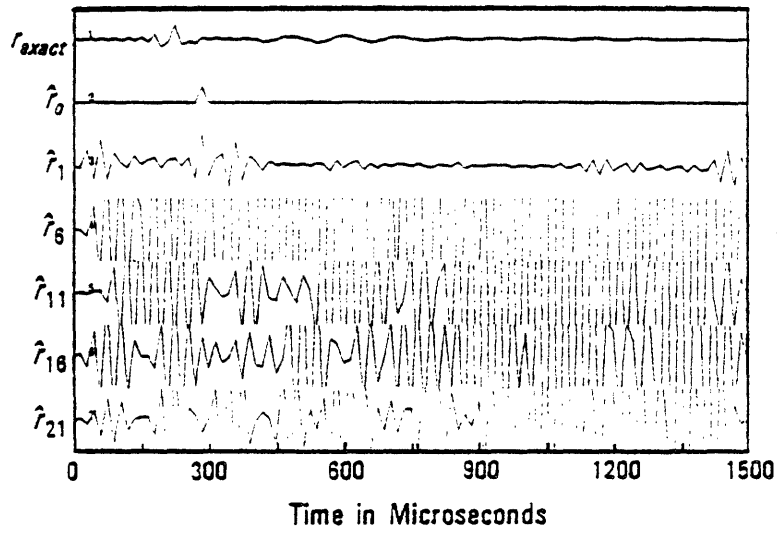

Figure 6-10

Experiment 1. Reflection coefficient signal estimates

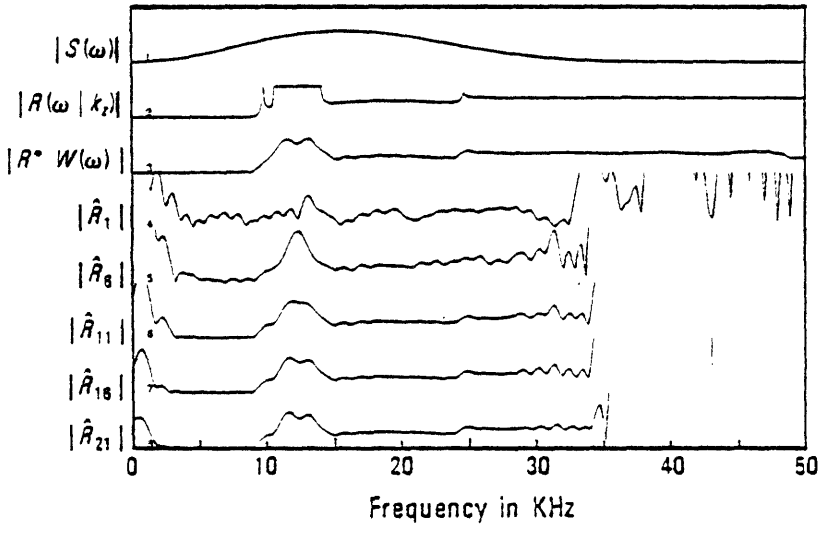

Figure 6-11

Experiment 1. Reflection coefficient estimates

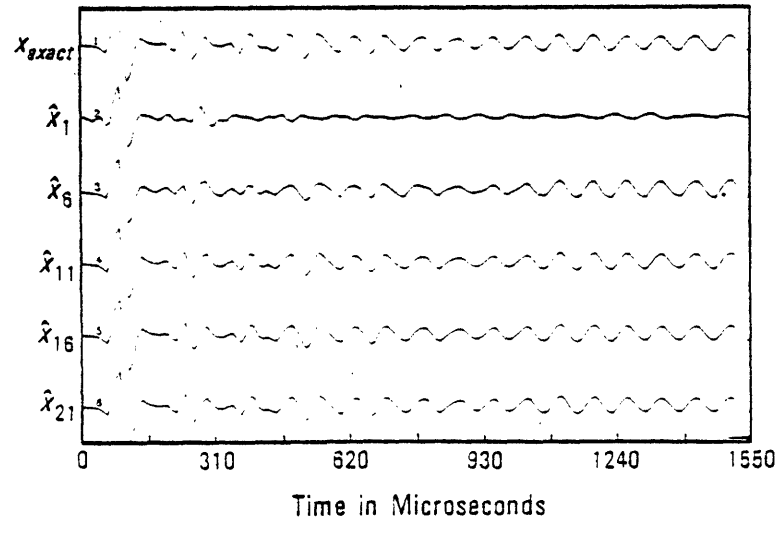

Figure 6-12

Experiment 1. Auxiliary signal estimates

time portion of the auxiliary signal significantly.

d. Sensitivity to the Initial Guess

Through additional testing of the iterative ML method not presented here, we have found that the convergence behavior is relatively insensitive to the initial guess for the reflection coefficient signal. Specifically, any "reasonable" initial guess will converge to the same experimental result in roughly the same number of iterations. This comment applies to all the experiments which follow. It should be realized, however, that the noise levels we consider are always low, so that the processing initially pays close attention to the observations and quickly forgets about the initial guess.

e. Computation Time Per Iteration

The computation time per iteration was accurately measured at 42.1 seconds in this and all the remaining experiments. For a given computer system, the computation time depends most strongly on the data length, N, and the reflection coefficient length, P, which were 156 and 100 in this instance. The leading order behavior of the computation time is proportional to NP^2, as we saw in the last chapter. The processing was done on a VAX machine under a VMS operating system and programmed in single precision FORTRAN.

f. A Comparison With Frequency Domain Division

The reflection coefficient at a single wavenumber is theoretically related to the single wavenumber reflected pressure field by the relation

$$R(\omega \mid k_z) = \frac{P_r(\omega \mid k_z)}{H(\omega)\, S(\omega) + P_r(\omega \mid k_z)} \tag{6.4}$$

where $P_r(\omega \mid k_z)$ is the Fourier transform of $p_r(t \mid k_z)$. Motivated by the simplicity of this formula, one might consider estimating the reflection coefficient using such a rule. In the

absence of noise, and for infinitely long data segments, this approach can be expected to work well. If noise is present or if the data segments are finite in length, then we anticipate that this approach will not work well.

In Figure 6-13 we show the result of transforming the first 1.55 ms of the exact delayed $p_r(t \mid k_c)$ and the first 200 μs of the delayed version of the Hilbert transform of the exact source pulse. Shown along side is the 21st iterative estimate from Figure 6-11. We see that the estimate obtained by direct frequency division is very poor even though there has been no noise added. The reason for the poor estimate is due solely to the fact that we have windowed the exact observations and the exact source signal. We conclude that since the method performs so poorly in a noise free environment, it is unlikely to perform better in the presence of noise. For this reason, we do not consider the direct frequency division estimation approach further.

6.5.2 The Results of Experiments 2 and 3

Experiments 2 and 3 differ from experiment 1 only in the selection of the noise standard deviations. Again, no noise is actually added into the source or the observations. In Figures 6-14 and 6-15 we present the reflection coefficient estimates associated with experiments 2 and 3. The format is the same here as in Figure 6-11.

We see that the primary effect of increasing the noise variance is to dramatically reduce the amplitude of the estimates out of the source band. This behavior is argued as follows. In experiment 1, the estimation system was, in effect, "told" that there was no noise present in the system. The estimator then attempted to use the frequencies which are out of the source passband to lower the estimation error. The fact that the out of band error was so large in experiment 1 is an indication of the difficulty the system had trying to reduce the error.

In experiments 2 and 3, the system was constrained less tightly. Here, there was no point in using the frequencies outside the passband of the source to reduce the error since these frequencies have little effect on the error and since the error could be made small enough using

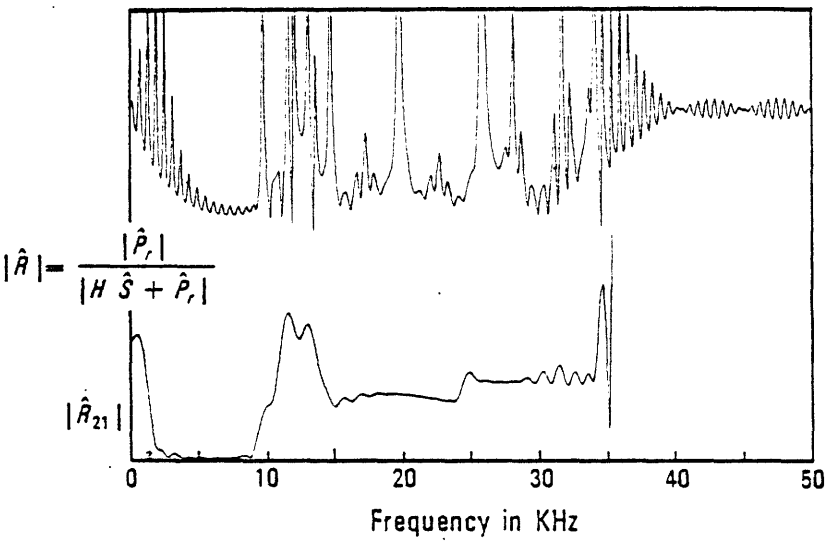

Figure 6-13

Experiment 1.
Comparision with direct
frequency domain division

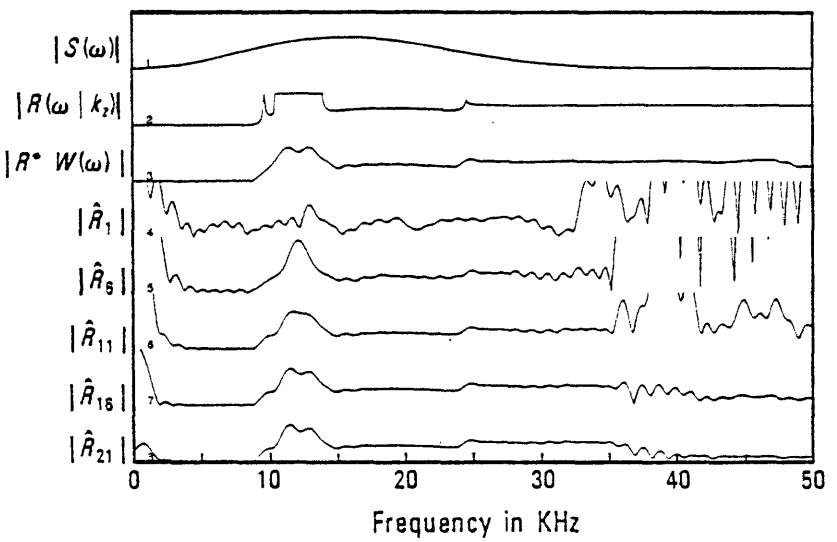

Figure 6-14

Experiment 2.
Reflection coefficient estimates.
infinite array
no noise added, 38 dB SNR

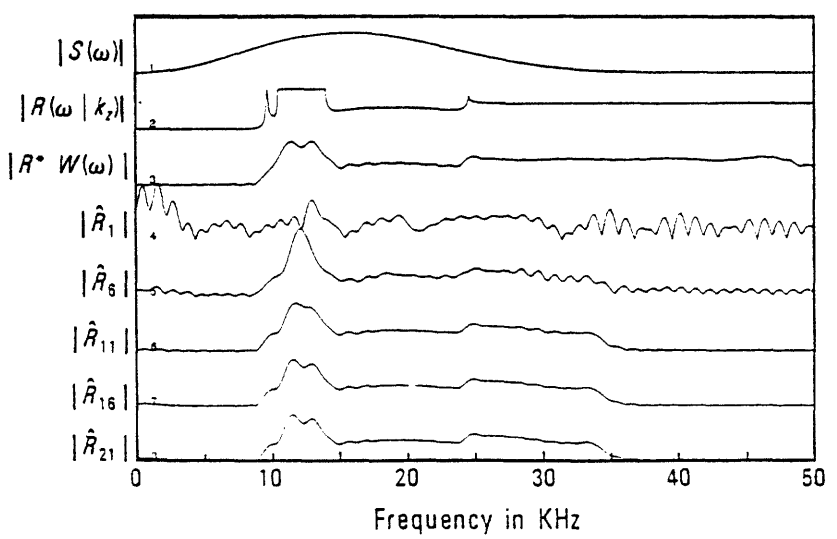

Figure 6-15

Experiment 3.
Reflection coefficient estimates.
infinite array
no noise added, 18 dB SNR

the in-band frequencies only.

6.5.3 Results of Experiments 4-6

In experiments 4-6 we add white Gaussian noise into the source and observations. As in the previous experiments, the infinite aperture array is used. In Figures 6-16 to 6-18 we show the estimation results. In each case 51 iterations were performed and estimates 1 through 51 in steps of 10 are shown in the figures. Convergence is seen to take place after only 11 iterations in each case. The performance of the method in experiments 4 and 5 are seen to be acceptable, while the performance in experiment 6 is, at best, marginally acceptable. The source and observation process SNR's in experiment 6 are each just under 19. We consider this to be the noise level at which the method begins to perform poorly.

6.5.4 Results of Experiments 7-9

In Figures 6-19 to 6-21 we show the results of experiments 7 to 9. These experiments used a 100 element array of synthetic data where the inter-receiver spacing was one inch. Again, this array is roughly 16 axial wavelengths long with roughly 6 spatial samples per axial wavelength. In each case, as in the last 3 experiments and in all the experiments which follow, 51 iterations are performed and we present every tenth estimate. Again, we see that approximate convergence is achieved after only 11 iterations.

In experiment 7, we added no artificial noise into the source or the observations. The purpose of this experiment was to see what the reflection coefficient estimate would be like if the estimation system was told that there was effectively no noise. The result in Figure 6-19 is interesting. We see that the reflection coefficient is quite accurate everywhere within the passband of the source, except in the "table" region of the reflection coefficient. There the estimate is seen to be distorted. This behavior is due to the fact that there is a mode formed from a frequency in the table region where the reflection coefficient has unity magnitude. The receiver array does not capture the long range modal propagation, as discussed earlier, so that it

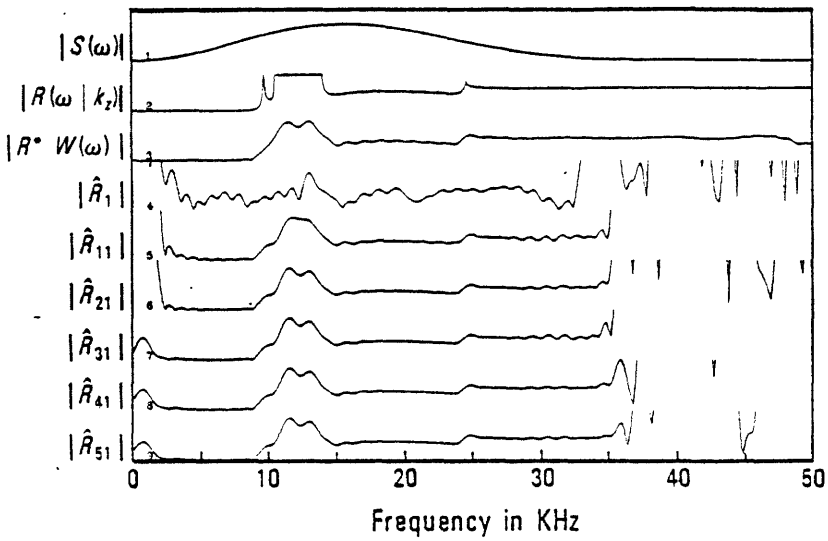

Figure 6-16

Experiment 4.
Reflection coefficient estimates.
infinite array
noise added, 58 dB SNR

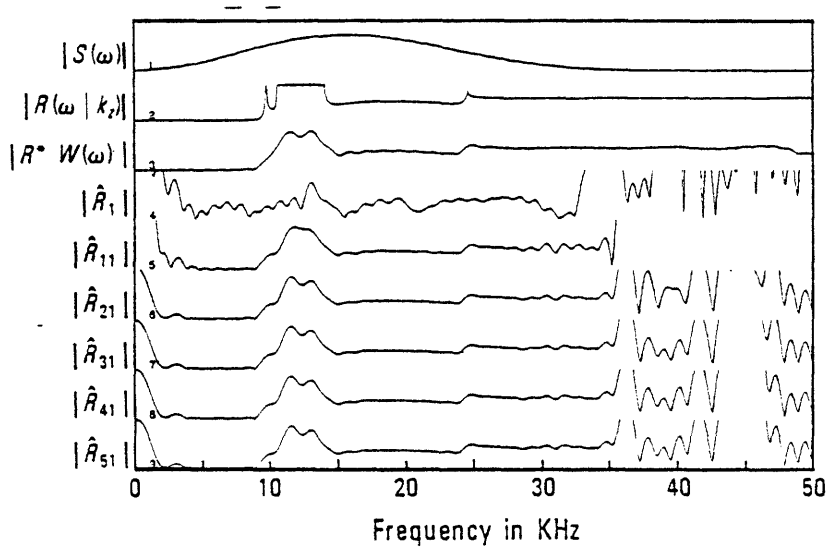

Figure 6-17

Experiment 5.
Reflection coefficient estimates.
infinite array
noise added, 38 dB SNR

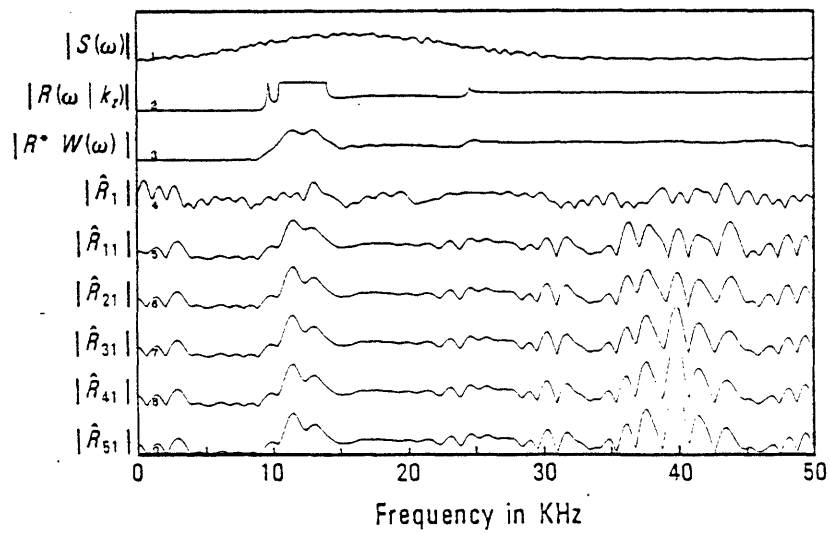

Figure 6-18

Experiment 6.
Reflection coefficient estimates.
Infinite array
noise added, 18 dB SNR

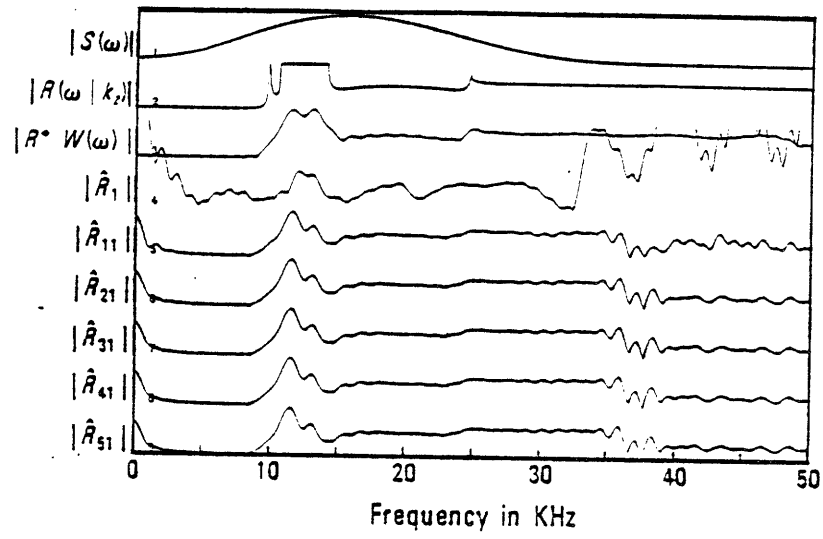

Figure 6-19

Experiment 7.
Reflection coefficient estimates.
16 λ array, 6 rcvr/λ
no noise added, 38 dB SNR

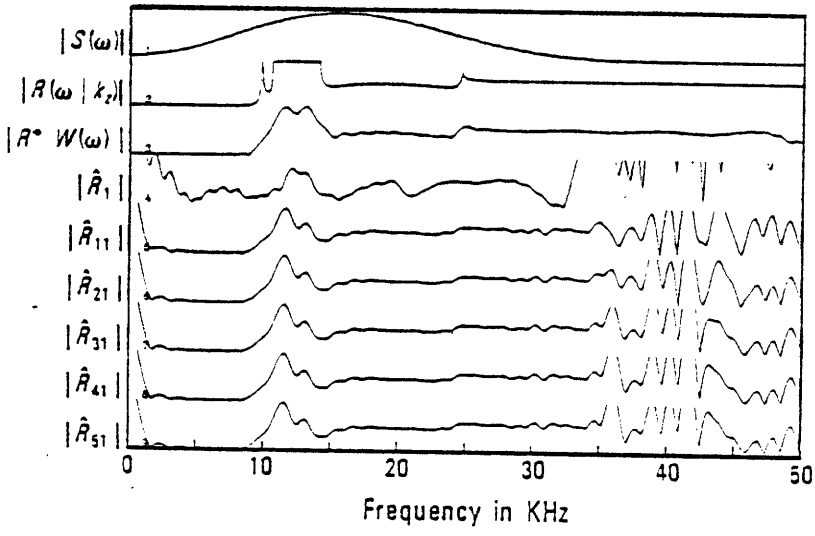

Figure 6-20

Experiment 8.
Reflection coefficient estimates.
16 λ array, 6 rcvr/λ
noise added, 38 dB SNR

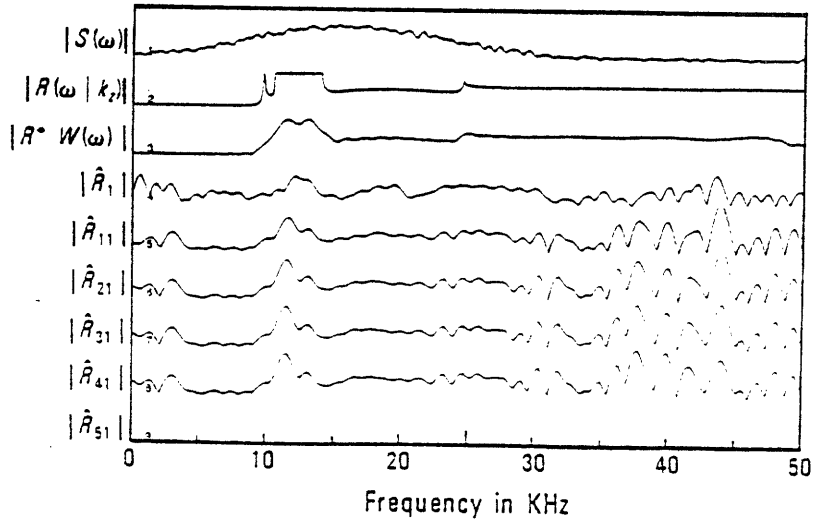

Figure 6-21

Experiment 9.
Reflection coefficient estimates.
16 λ array, 6 rcvr/λ
noise added, 18 dB SNR

is not surprising that the estimate will not be accurate at the frequencies corresponding to the modes.

In experiments 8 and 9 we add noise into the system and examine the resulting estimation performance. We find that the performance is acceptable when the signal-to-noise ratios are in the 30's but are only barely acceptable for SNR's in the high teens. Thus, the performance drops off at roughly the same point as in the infinite array case.

6.5.5 Results of Experiments 10-12

The array associated with experiments 10-12 is the same as the array in experiments 7-9, only every other receiver element has been eliminated. The inter-receiver spacing for this set of experiments, then, is 2", while the axial component of wavelength is roughly 5.6". Thus we expect to see some problems associated with the marginal sampling of the field. We have not sacrificed the array aperture so that any degradation in the performance of this array will be due solely to the spatial sampling issue.

In Figure 6-22 we show the estimation performance in the case where no artificial noise was added. We note that the estimates are only slightly more distorted in the table region than they were with the 100 element array. This is because the array aperture roughly the same in these two cases. However, the primary area of degradation is in the estimate at higher frequencies. Here we see that the reflection coefficient estimate becomes poor even within the passband of the source. We attribute this to spatial aliasing.

The cases where additive noise was introduced are shown in Figures 6-23 and 6-24. Here, there are no surprises. With a SNR in the 30 dB range, the estimate is the same as if no noise were added. However, when the source and observation SNR's drop into the teens, the estimates begin to degrade.

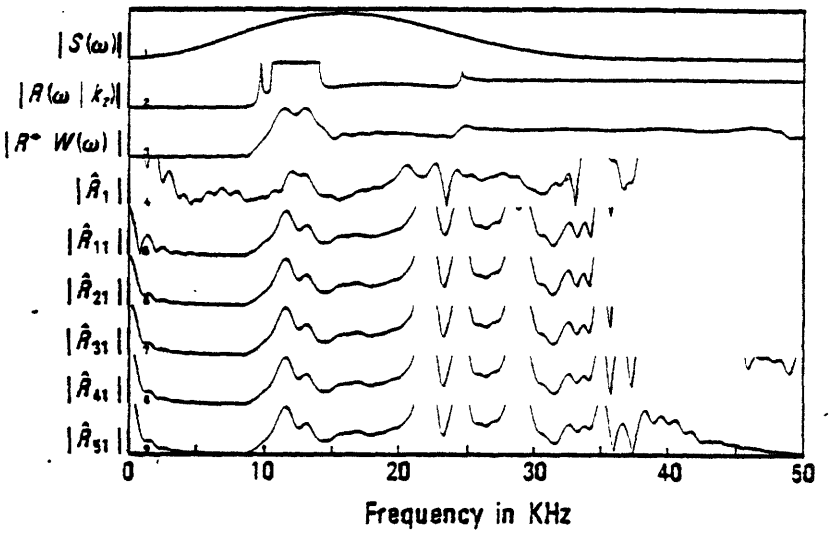

Figure 6-22

Experiment 10.
Reflection coefficient estimates.
16 λ array, 3 rcvr/λ
no noise added, 38 dB SNR

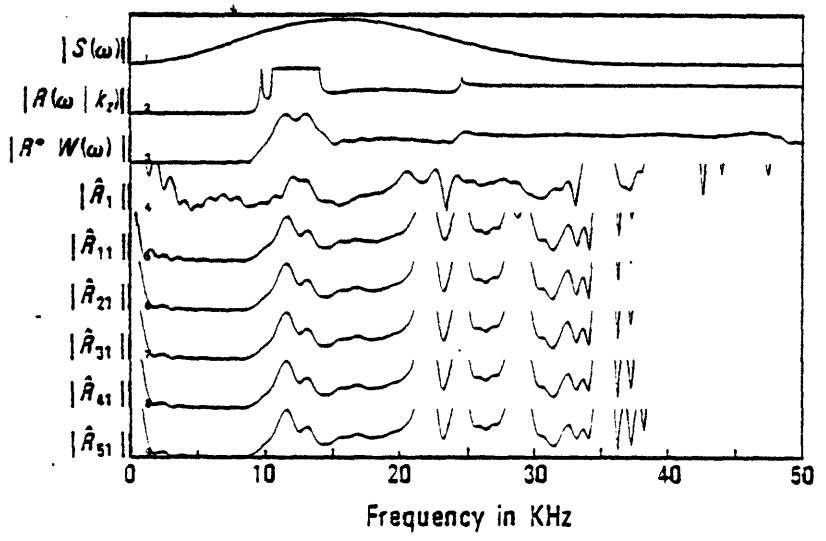

Figure 6-23

Experiment 11.
Reflection coefficient estimates.
16 λ array, 3 rcvr/λ
noise added, 38 dB SNR

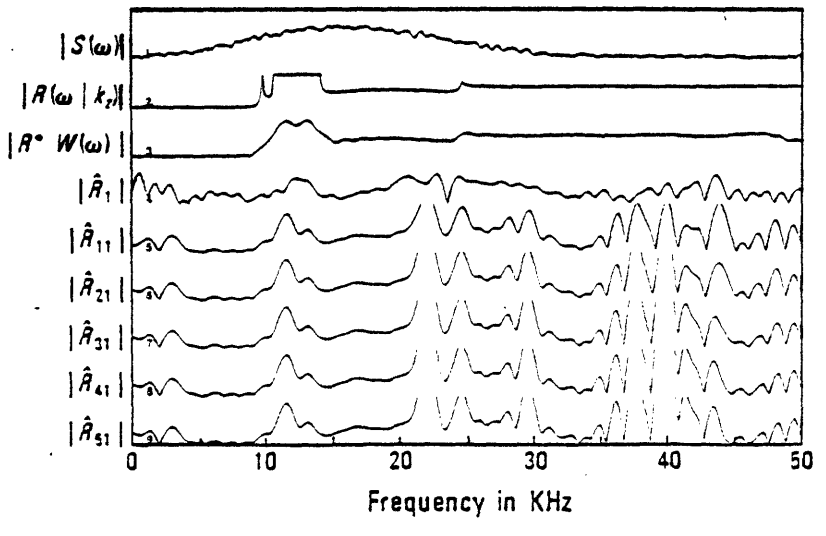

Figure 6-24

Experiment 12.
Reflection coefficient estimates.
16 λ array, 3 rcvr/λ
noise added, 18 dB SNR

6.5.6 The Results of Experiments 13-15

The array associated with experiments 13-15 has 50 elements spaced an inch apart so that the aperture is roughly half that of experiments 7-9. The results of experiments 13-15 are shown in Figures 6-25 to 6-27.

We see from Figure 6-25 that by cutting the aperture in half, a serious degradation in the estimate results. The estimate in the table region is distorted and the compressional wave feature is essentially lost. We conclude that with this 4 foot aperture, we are not able to estimate the reflection coefficient at those frequencies where it is close to unity in magnitude. This is because the waves associated with the reflection coefficients near unity propagate out beyond the array aperture.

In Figures 6-26 and 6-27, we show the estimation performance in the presence of noise. Again, the method performs as in the previous experiments and begins to degrade at roughly the same SNR's.

6.6 Preliminary Conclusions

Based on the experimental results presented in the previous section, we feel that it is safe to draw the following conclusions.

(1) The iterative ML estimation approach is superior to a direct division approach in the frequency domain based on equation (6.4).

(2) The iterative ML method cannot estimate the reflection coefficient at those frequencies outside the passband of the source pulse.

(3) Within the passband of the source, using an array with a transmitter-receiver spacing of zero, the performance of the method depends strongly on the array aperture and the inter-receiver spacing.

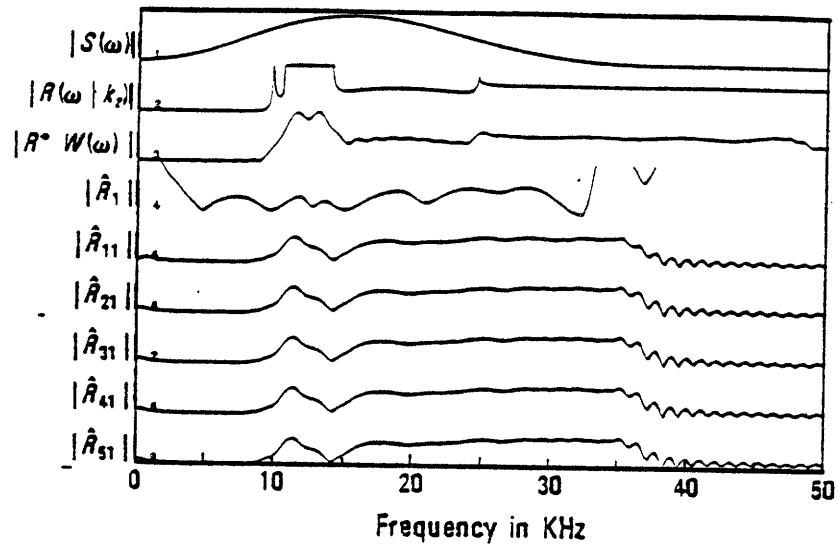

Figure 6-25

Experiment 13.
Reflection coefficient estimates.
8 λ array, 6 rcvr/λ
no noise added, 38 dB SNR

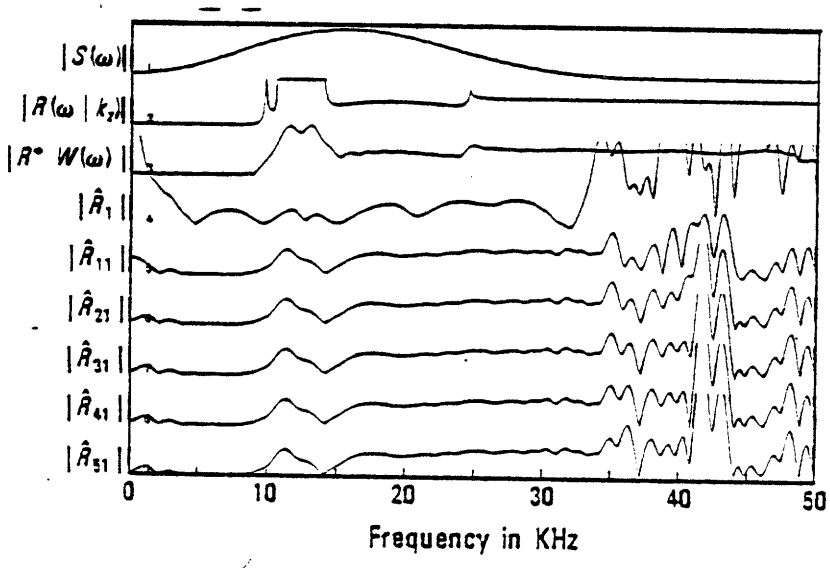

Figure 6-26

Experiment 14.
Reflection coefficient estimates.
8 λ array, 6 rcvr/λ
noise added, 38 dB SNR

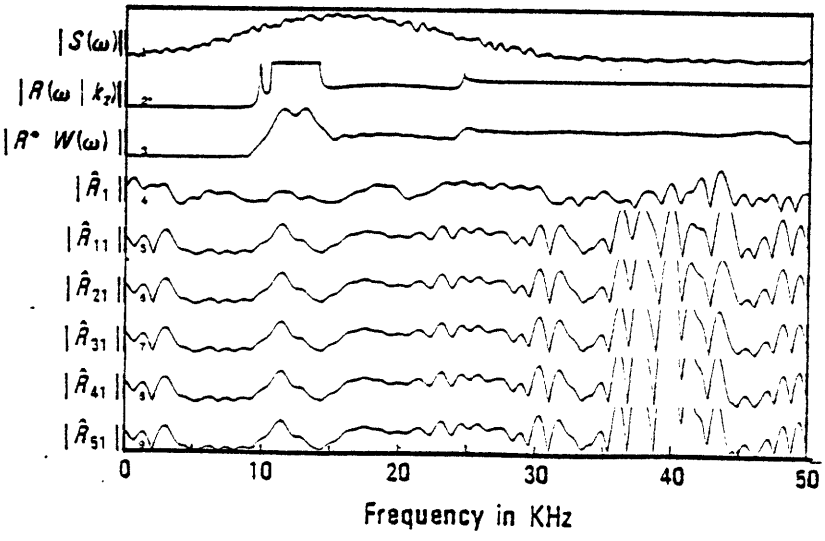

Figure 6-27

Experiment 15.
Reflection coefficient estimates.
8 λ array, 6 rcvr/λ
noise added, 18 dB SNR

(i) It appears that at least 5 spatial samples are needed per wavelength and that, if less are used, the estimation performance may be very poor at some frequencies.

(ii) A long array aperture is needed to estimate reflection coefficient at those frequencies where it is near unity in magnitude, or equivalently, a short aperture is able to estimate the reflection coefficient only at those frequencies where the reflection coefficient is small. An array 16 wavelengths long was found to estimate the reflection coefficient at those frequencies where it is near unity in magnitude significantly better than an array which is 8 wavelengths long.

(iii) The reflection coefficient cannot be reliably estimated at those frequencies which excite propagating modes. This is because these modes propagate to distances much longer than the extent of any feasible array.

(4) Independent of the array aperture and the inter-receiver spacing, the estimates are seen to become marginally acceptable when the signal-to-noise ratios (defined in Section 6.4) is in the teens.

(5) Independent of the array aperture, the inter-receiver spacing and the signal-to-noise ratios, the iterative ML method is seen to converge in roughly 10 iterations or less. The convergence behavior was found to be insensitive to the initial guess of the reflection coefficient signal. The method always converged to the "right answer" within the passband.

6.7 Summary

We have demonstrated that the iterative ML method is able to estimate the reflection coefficient at some but not all frequencies from data provided by a finite aperture receiver array which has been corrupted with noise. The iterative method performs poorly at those frequencies outside of the passband of the source and at those frequencies corresponding to the modes. The iterative method performs best at those frequencies at which the reflection coefficient is relatively

small in magnitude. It is felt that these are fundamental findings which will be shared by any estimation approach. It is not possible to say whether the iterative ML method performs better or worse than some other statistically based method would in this application. However, it is safe to say that the iterative ML method will perform better than any non-statistically based method.

It is felt that, through careful selection of the source passband and the axial component of wavenumber, the reflection coefficient can be reliably estimated in a band of frequencies with a relatively short receiver array. The extent to which this research is pursued in the future will depend primarily on the usefulness of such a limited estimate. The sensitivity of such a reflection coefficient estimate to the formation parameters, and in particular, to radial variation in the formation, is a subject for future study.

A potentially practical application of the single wavenumber system might be the case where $k_z = 0$. With an axial wavelength of zero, only one receiver will, in theory, be needed. This choice of axial wavenumber is analogous to normal incidence reflection seismology performed in a borehole. The frequency content of the reflected normal incidence pulse is analyzed in terms of the radial structure of the formation.

VII. CONTRIBUTIONS AND FUTURE RESEARCH

7.1 Thesis Contributions

A general theme throughout this thesis involved looking at the analogous problem in a planar geometry and asking whether the same concepts which were successful there can be applied in the cylindrical case. This approach was consistently rewarding. The concepts of the monochromatic cylindrical wave and the cylindrical wave reflection coefficient are direct analogs of key concepts in planar geometries and served as the physical basis of this thesis. It is felt that these cylindrical wave concepts have not enjoyed the same fundamental role as plane wave concepts do in layered media applications and that this thesis may help to bring these ideas to the forefront in borehole wave propagation. In fact, the properties of cylindrical waves and of the cylindrical wave reflection coefficient derived in Chapter III of this thesis are of a most fundamental nature and yet were not commonly known until now. This is in distinct contrast to plane waves and the plane wave reflection coefficient whose properties have been extensively studied and are well known. A major contribution of this thesis, then, is in illustrating the fundamental importance of cylindrical waves and of the cylindrical wave reflection coefficient in cylindrical geometry applications.

Besides the cylindrical waves and the cylindrical wave reflection coefficient, other concepts from planar problems may be transferable to cylindrical geometry problems. For example, travel-time inversion methods used in refraction seismology appear to apply directly to the existing acoustic logging method and yet they have not been exploited as yet. The tomographic concept of reconstructing an object from a set of its projections also appears to be applicable in a borehole refraction context. Also, surface reflection seismology processing methods may find a use in processing short-spaced acoustic logging data. Here, the reflection coefficient signal is estimated directly and then migrated. Again, these ideas have not been explored for a cylindrical geometry and are outlined in the next section as promising areas for future investigation.

The development of fast methods for generating arrays of synthetic acoustic logging data (Chapter IV) was a part of this research which has already had a significant effect in acoustic logging related research. Synthetic data is now used on a daily basis to aid in understanding the effects of various formation parameters on the data, to aid in the testing and performance evaluation of new signal processing techniques, and may eventually lead to a useful analysis-by-synthesis method for inverting field data. Prior to the development of the method in Chapter IV the generation of synthetic data required an order of magnitude more time which made its use on a regular basis unattractive.

The application of the iterative maximum likelihood dereverberation theory developed by Musicus to a problem other than pole-zero estimation (Chapter V) may have far reaching effects. The dereverberation problem we apply the method to here is just one example of a class of feedback problems which the method may find application in. Reverberation problems arise in many contexts, and feedback problems in even more, so that the development of this technique may find use elsewhere.

Finally, this research may eventually develop into a design and processing method for a short-spaced acoustic logging tool. Such a tool would analyze energy reflected by the formation, rather than refracted by it as in the current tool, and would offer the possibility of resolving radial variation in the formation. The reflection coefficient estimation goal of this thesis is only one approach to take in this regard.

7.2 Furture Research

We conclude this thesis by identifying several promising areas for theoretical research relating to the acoustic logging application. These include research areas associated with the reflection coefficient estimation approach investigated in this thesis as well as new and different areas of research which came to light in the course of this research.

We view the acoustic well logging problem as one of multi-dimensional acoustic imaging

from a perspective in a borehole. The number of dimensions in the image depends upon the number of dimensions in the underlying formation model and the image is constructed by resolving a particular acoustic formation parameter as a function of space. Here, a robust measurement principle is needed and the fundamental resolution-versus-stability issues arise.

As in Chapter II, we divide the research areas into those based on a refraction principle and those based on reflection. Within the refraction approach, we suggest the imaging of the velocity structure of the formation in two dimensions (radially as well as axially) as a promising area of research. Here, we consider the application of travel-time inversion methods as well as tomographic reconstruction concepts to the 2D imaging problem. Within the reflection-based approach, we suggest the application of reflection seismic processing methods to short-spacing borehole acoustic data and also suggest further areas of research relating to the reflection coefficient approach. Each of these reflection approaches involves a formation model with only radial variation, and therefore, is a one-dimensional imaging problem.

7.2.1 Refraction-Based 2D Velocity Imaging (Radial and Axial)

a. Travel-Time Inversion

As we saw in Chapter II, the travel-time inversion methods which have been developed for planar geometry applications apply equally well to a cylindrical geometry and may lead to a useful 2D velocity imaging system. However, the cylindrical refraction problem differs from the planar refraction problem in two fundamental ways. First, the formation in the planar case typically contains strong planar reflectors parallel to the measurement plane, while in the cylindrical case, the strong planar reflectors are perpendicular to the measurement plane, with the noteable exception of the mud/formation interface. In addition, the diffuse radial variation in the cylindrical problem is unlike any variation of interest in the planar problem. Secondly, in the borehole problem, we continually shift the instrumentation within the hole to obtain travel-time information from depth z_1 to depth z_2, denoted $t(z_1,z_2)$. It is not unreasonable, then, to assume

that we have a measurement of an array of first arrival times, $t(z_1,z_2)$, and to consider the inversion of this information to extract $v(r,z)$. This is unlike surface refraction experiments where the source movement is relatively limited.

The brief analysis of travel-time inversion in Chapter II was enough to produce some significant benefits. The analysis there put the existing logging method in perspective as a restricted travel-time inversion technique. It indicated how the correlation between successive local experiments might be used to enhance axial resolution without sacrificing stability, and how a formation model more realistic than the homogeneous model which is currently assumed might be incorporated into the processing method. Prior to this analysis, it was not clear how to incorporate shot-to-shot correlation into the processing, nor was it clear how to treat more complicated formation models.

b. Tomographic Reconstruction

Also under the domain of reflection-based methods is the inverse scattering theory, or tomographic approach, outlined in Chapter II. In this approach, the medium is reconstructed from a set of projections. Here, arrival time information is viewed as an integral of the formation slowness (i.e. inverse velocity) along the unknown ray path. Given a collection of such projections, the problem, then, is to reconstruct the slowness structure.

This application for tomographic concepts differs from previous applications in some significant ways. First, the refraction geometry is different. In typical tomography arrangements, such as x-ray tomography, the instrumentation can be placed on either side of the object to be imaged and moved around as desired. In this application, both the source and receivers are on the same "side" of the object, but can be moved independently within the measurement plane. Secondly, the ray path is unknown. This is viewed as a serious but challenging complication.

7.2.2 Reflection-Based 1D Imaging (Radial Only)

a. Reflection Seismic Methods

The method used in planar layered media applications for analyzing reflection data may prove useful in the cylindrical geometry application. This method consists of a stacking operation, followed by predictive deconvolution, followed by a migration step. Both the stacking and predictive deconvolution steps attempt to enhance primary reflections off of subsurface reflectors relative to the multiple reflections and noise. This is analogous to estimating the reflection coefficient signal discussed in this thesis. The migration step then maps the offset-versus-time domain into an offset-versus-depth image and is analogous to inverting the transform of the reflection coefficient to obtain a radial image of the formation structure.

The application of this processing approach to the borehole geometry is a possible direction for future research. The first step here would be to invert data associated with a formation which has strong radial reflectors. For this case, some degree of success in expected. Following this, the reflectors can be made progressively weaker.

b. The Reflection Coefficient Approach

Within the reflection coefficient based approach, there are variety of areas to pursue. First, there is the treatment of the direct arrival issue. In this thesis, we treated the estimation of the reflection coefficient from the reflected component of the total field only. The actual problem of interest is to estimate the reflection coefficient from the total measured field directly.

Another important area of research is the inversion of the reflection coefficient to recover the radial velocity structure of the formation. This is analogous to the Gel'fand Levitan inverse scattering method for inverting the plane wave reflection coefficient at normal incidence, or to Claerbout's discrete formulation, etc. Again, the first step here is to study a simple formation model.

Aside from the single wavenumber model, the next choice for a signal processing model should be the monochromatic model. Here, the situation is more complicated because the

reflection coefficient signal in this case is complex-valued and even. When the iterative ML theory is applied to this formulation, the I−B matrix no longer has a unity determinant. Instead, this matrix takes on a symmetric Toeplitz form whose determinant can be readily computed in a recursive fashion, but is a nonlinear function of the parameters. This means that the estimation problem is no longer linear and that the method is not nearly as elegant when applied to this case.

Another area of research involves the extension of the processing into two dimensions by treating the 2D model outlined in Chapter V. The 2D formulation has not been explored and it is not clear whether the iterative ML theory will extend nicely into two dimensions.

The results generated in Chapter VI for the single wavenumber system are of a preliminary nature. Further testing of this approach for different values of axial wavenumber, different formation models, different source pulses, etc. will produce more conclusive results concerning behavior of this estimation approach. Specifically, the equivalent of normal incidence reflection seismology (i.e. $k_z = 0$) should be explored.

Finally, other areas which are not well understood include the following. In cylindrical geometry problems, Hilbert transform relations tend to appear regularly and are of curious concern both from a physical standpoint as well as from a signal processing point of view. For example, the signal which drives the single wavenumber system is, somewhat surprisingly, the Hilbert transform of the source pulse. As another example, the cylindrical wave reflection coefficient approaches the Hilbert transform of the plane wave reflection coefficient as the borehole becomes large relative to a wavelength. More generally, it can be said that the differences between the properties of plane waves and cylindrical waves, and between the properties of the plane wave reflection coefficient and the cylindrical wave reflection coefficient are not well understood. Here, there are issues of causality, real-valuedness, conservation of energy implications, impedance implications, etc. It is felt that the similarities and differences are of fundamental interest and importance and should be explored further.

7.2.3 Other Areas

The research directions outlined in this chapter represents only a small fraction of the spectrum of possible directions. Others include the estimation of acoustic attenuation, acoustic fracture detection methods, mechanical strength estimation, etc. Also, new dimensions to acoustic logging can be introduced by moving the source off the borehole axis. Here, the axi-symmetric symmetry is destroyed and azimuthal variation in the formation can be examined.

REFERENCES

[1] Abramowitz, M., and Stegun, I.A., Handbook of Mathematical Functions, Dover Publications, New York, 1964.

[2] Aki, K. and Richards, P.G. Quantitative Seismology— Theory and Methods, W.H. Freeman and Company, San Francisco, 1980.

[3] Allaud, L.A., and Martin, M.H., Schlumberger—The History of a Technique, Wiley, 1977.

[4] Aron, J., Murray, J., and Seeman, B., "Formation Compressional and Shear Interval-Transit-Time Logging by Means of Long Spacings and Digital Techniques", presented at the 53rd Conf. of the Soc. of Petroleum Engrs., Houston TX, October 1978.

[5] Biot, M.A., "Propagation of Elastic Waves in a Cylindrical Bore Containing a Fluid", *J. Appl. Phys.*, Vol. 23, No. 9, pp. 997-1005, September 1952.

[6] Brekhovskikh, L.M. Waves in Layered Media, Academic Press, 1960.

[7] Chang, S.K., and Everhart, A.H., "N-Layered Real Axis Integration Model for Borehole Acoustics", Schlumberger-Doll Monthly Progress Report, March 1982, Schlumberger Doll Research, Ridgefield, CT.

[8] Cheng, C.H., Tubman, K.M. and Toksöz, M.N., "Propagation of Seismic Waves in a Multilayered Borehole", presented at the 1981 meeting of the Society of Exploration Geophysicists, Dallas TX, October 1981.

[9] Cheng, C.H., and Toksöz, M.N., "Seismic Wave Propagation in a Fluid-Filled Borehole and Synthetic Acoustic Logs", *Geophysics*, Vol. 46, No. 7, pp. 1042-1053, July 1981.

[10] Claerbout, J.F., Fundamentals of Geophysical Data Processing, McGraw-Hill, 1976.

[11] Dahlquist, G., Bjork, A. and Anderson, N., Numerical Methods, Prentice-Hall, 1974.

[12] Eykhoff, P., Systems Identification: Parameter and State Estimation, Wiley, 1974.

[13] Evans, H.B., "Status and Trends in Logging", *Geophysics*, Vol. 35, No. 1, pp. 93-112, February 1970.

[14] Ewing, Jardetsky and Press, Elastic Waves in Layered Media, McGraw-Hill, 1957.

[15] Frisk, G.V., "Inhomogeneous Waves and the Plane Wave Reflection Coefficient", *J. Acoust. Soc. Am.*, Vol. 66, No. 1, pp. 219-234, 1979.

[16] Gradshteyn, I.S., and Ryzhik, I.M., Table of Integrals, Series, and Products, Academic Press, 1965.

[17] Kay, S.M., and Marple, S.L., "Spectrum Analysis--A Modern Perspective", *Proc. IEEE*, Vol. 69, No. 11, pp. 1380-1419, November 1981.

[18] Koehler, F. and Taner, M.T., "Direct and Inverse Problems Relating Reflection Coefficients and Reflection Response for Horizontally Layered Media", *Geophysics*, Vol. 42, No. 6, pp. 1199-1206, October 1977.

[19] Kokesh, F.P. and Blizard, R.B., "Geometrical Factors in Sonic Logging", *Geophysics*, Vol. XXIV, No. 1, pp. 64-76, February 1959.

[20] Kurkjian, A.L., and Aron, J., "Time Delay Estimation in Sonic Well Logging", presented at the Conference on Time Delay Estimation, U.S. Naval Postgraduate School, Monterey CA, May 1979.

[21] Kurkjian, A.L., and Chang, S.K., "The Numerical Evaluation of Acoustic Well Logging Waveforms", accepted for publication in the *IEEE Trans. on ASSP*, accepted in December 1981.

[22] Makhoul, J., "Linear Prediction: A Tutorial Review", *Proc. IEEE*, Vol. 63, pp. 561-580, April 1975.

[23] Musicus, B.R., "An Iterative Maximum Likelihood Technique With Noisy Data", M.S. thesis, Massachusetts Institute of Technology Cambridge MA, February 1979.

[24] Musicus, B.R., and Lim, J.S., "Iterative Maximum Likelihood Estimation of AR and ARMA Models from Noisy Data", submitted for publication to *IEEE Trans on ASSP*, March 1982.

[25] Oppenheim, A.V. and Schafer, R.W., Digital Signal Processing, Prentice-Hall, 1975.

[26] Papoulis, A., The Fourier Integral and its Applications, McGraw-Hill, 1962.

[27] Peterson, E.W., "Acoustic Wave Propagation Along a Fluid-Filled Cylinder", *J. Appl. Phys.*, Vol. 45, No. 8, pp. 3340-3350, August 1974.

[28] Pickett, G.R., "Applications for Borehole Geophysics in Geophysical Exploration", *Geophysics*, Vol. 35, No. 1, pp. 81-92, February 1970.

[29] Porter, R.P. and Marzetta, T., "Sonic Well Logging-- Acoustic Propagation and Signal Processing", *J. Acoust. Soc. Am.*, Suppl., 1 68, S8, 1980.

[30] Ricker, N., "The Form and Laws of Propagation of Seismic Wavelets", *Geophysics*, Vol. XVIII, No. 1, pp. 10-40, 1953.

[31] Roever, W.L., Rosenbaum, J.H., and Vining, T.F., "Acoustic Waves from an Impulsive Source in a Fluid-Filled Borehole", *J. Acoust. Soc. Am.*, Vol. 55, No. 6, pp. 1144-1157, 1974.

[32] Rosenbaum, J.H., "Synthetic Microseismograms: Logging in Porous Formations", *Geophysics*, Vol. 39, No. 1, pp. 14-32, February 1974.

[33] Schoenberg, M., Marzetta, T., Aron, J., and Porter, R.P., "Space-Time Dependence of Acoustic Waves in a Borehole", *J. Acoust. Soc. Am.*, Vol. 70, No. 5, pp. 1496-1507, November 1981.

[34] Segesman, F.F., "Well-logging Method", *Geophysics*, Vol. 45, No. 11, pp. 1667-1684, November 1980.

[35] Sheriff, R.E., "Glossary of Terms Used in Well Logging", *Geophysics*, Vol. 35, No. 6, pp. 1116-1139, December 1970.

[36] Somers, E.V., "Propagation of Acoustic Waves in a Liquid-Filled Cylindrical Hole, Surrounded by an Elastic Solid", *J. Appl. Phys.*, Vol. 24, No. 5, pp. 515-521, May 1953.

[37] Tsang, L., and Rader, D., "Numerical Evaluation of a Transient Acoustic Waveforms due to a Point Source in a Fluid-Filled Borehole", *Geophysics*, V 44, 1706-1720, (1979).

[38] Tsang, L. and Kong, J.A., "Asymptotic Methods for the First Compressional Head Wave Arrival in a Fluid-Filled Borehole", *J. Acoust. Soc. Am.*, Vol. 65, No. 3, pp. 647-654, March 1979.

[39] Van Trees, Estimation and Detection Theory: Volume I, McGraw-Hill, 1968.

[40] White, J.E., and Zechman, R.E., "Computed Response of an Acoustic Logging Tool", *Geophysics*, Vol. 33, No. 2, pp. 302-310, April 1968.

[41] White, J.E., Seismic Waves, McGraw-Hill, 1965.

[42] White, J.E., "Elastic Waves Along a Cylindrical Bore", *Geophysics*, Vol. XXVII, No. 3, pp. 327-333, June 1962.

[43] White, J.E., "Signals in a Borehole due to Plane Waves in a Solid", *J. Acoust. Soc. Am.*, Vol. 25, No. 5, Sept. 1953.

DISTRIBUTION LIST

	DODAAD Code	
Director Advanced Research Project Agency 1400 Wilson Boulevard Arlington, Virginia 22209 Attn: Program Management	HX1241	(2)
Program Director Fluid Dynamics Mathematical and Information Sciences Division Office of Naval Research 800 North Quincy Street Arlington, Virginia 22217	N00014	(3)
Administrative Contracting Officer E19-628 Massachusetts Institute of Technology Cambridge, Massachusetts 02139	N66017	(1)
Director Naval Research Laboratory Attn: Code 2627 Washington, D.C, 20375	N00173	(6)
Defense Technical Information Center Bldg. 5, Cameron Station Alexandria, Virginia 22314	S47031	(12)
Office of Naval Research Easter/Central Regional Office Bldg. 114, Sec. D 666 Summer Street Boston, Massachusetts 02210	N62879	(1)
TACTEC Battelle Memorial Institute 505 King Avenue Columbus, Ohio 43201	79986	(1)